

DOT/FAA/AR-02/130

Office of Aviation Research
Washington, D.C. 20591

Analytical Modeling of ASTM Lap Shear Adhesive Specimens

DISTRIBUTION STATEMENT A

Approved for Public Release
Distribution Unlimited

February 2003

Final Report

This document is available to the U.S. public
through the National Technical Information
Service (NTIS), Springfield, Virginia 22161.



U.S. Department of Transportation
Federal Aviation Administration

20030508 165

NOTICE

This document is disseminated under the sponsorship of the U.S. Department of Transportation in the interest of information exchange. The United States government assumes no liability for the contents or use thereof. The United States Government does not endorse products or manufacturers. Trade or manufacturer's names appear herein solely because they are considered essential to the objective of this report. This document does not constitute FAA certification policy. Consult your local FAA aircraft certification office as to its use.

This report is available at the Federal Aviation Administration William J. Hughes Technical Center's Full-Text Technical Reports page: actlibrary.tc.faa.gov in Adobe Acrobat portable document format (PDF).

1. Report No. DOT/FAA/AR-02/130		2. Government Accession No.		3. Recipient's Catalog No.	
4. Title and Subtitle ANALYTICAL MODELING OF ASTM LAP SHEAR ADHESIVE SPECIMENS				5. Report Date February 2003	
				6. Performing Organization Code	
7. Author(s) Charles Yang, John S. Tomblin, and Zhidong Guan				8. Performing Organization Report No.	
9. Performing Organization Name and Address Department of Mechanical Engineering Wichita State University Wichita, KS 67260				10. Work Unit No. (TRAIS)	
				11. Contract or Grant No. IA031	
12. Sponsoring Agency Name and Address U.S. Department of Transportation Federal Aviation Administration Office of Aviation Research Washington, DC 20591				13. Type of Report and Period Covered Final Report	
				14. Sponsoring Agency Code ACE-120	
15. Supplementary Notes The FAA William J. Hughes Technical Center COTR was Mr. Peter Shyprykevich.					
16. Abstract An analytical model was developed to predict the stress distribution within the specimen specified in ASTM D 3165 "Strength Properties of Adhesives in Shear by Tension Loading of Single-Lap-Joint Laminated Assemblies." In the developed model, the composite adherends were assumed elastic orthotropic, and the adhesive was assumed elastic-perfectly plastic. Experimental joint strength data was used in conjunction with the developed model to define the failure criterion for cohesive failure mode. Finite element analyses were conducted to simulate the behavior of both ASTM D 5656 "Standard Test Method for Thick-Adherend Metal Lap-Shear Joints for Determination of the Stress-Strain Behavior of Adhesives in Shear by Tension Loading" and ASTM D 3165 test specimens for deformation, stress distribution, and failure. In the finite element models, aluminum adherends were assumed elastic-perfectly plastic, and the adhesive stress-strain relation was determined by trial calculations of ASTM D 5656 specimens and comparison to experimental results. Both the equivalent plastic strain criterion and the fracture mechanics approach with <i>J</i> -integral were used as failure criteria. Predicted joint strengths were compared with experimental data.					
17. Key Words Composite joints, Adhesive joints, Adhesive property, ASTM D 3165, ASTM D 5656			18. Distribution Statement This document is available to the public through the National Technical Information Service (NTIS), Springfield, Virginia 22161.		
19. Security Classif. (of this report) Unclassified		20. Security Classif. (of this page) Unclassified		21. No. of Pages 78	
				22. Price	

TABLE OF CONTENTS

	Page
EXECUTIVE SUMMARY	xi
1. INTRODUCTION	1-1
2. ANALYTICAL MODEL ON ASTM D 3165 SPECIMEN	2-1
2.1 Model Derivation	2-1
2.1.1 Adherend Formulation	2-1
2.1.2 Adhesive Behavior in Elastic Regions	2-3
2.1.3 Adhesive Behavior in Plastic Regions	2-4
2.1.4 Solution Procedure	2-6
2.2 Results and Discussion	2-6
3. FINITE ELEMENT ANALYSES OF ASTM D 5656 AND ASTM D 3165 SPECIMENS	3-1
3.1 Finite Element Models of ASTM D 5656 Specimens	3-1
3.1.1 Explicit Direct-Integration Dynamic Analysis	3-2
3.1.2 Nonlinear Analysis for Both Adhesive and Adherends	3-2
3.1.3 Displacement Control at the End of Adherend	3-6
3.1.4 Half Model	3-6
3.1.5 Shear Failure Model	3-7
3.2 Finite Element Models of ASTM D 3165 Specimens	3-8
3.2.1 <i>J</i> -Integral	3-9
3.2.2 Modeling the Crack Tip Singularity	3-9
3.3 Results and Discussion of ASTM D 5656 Specimens	3-11
3.3.1 Deformation Analysis (ASTM D 5656)	3-11
3.3.2 Stress Analysis (ASTM D 5656)	3-14
3.3.3 Failure Mode and Failure Criterion (ASTM D 5656)	3-19
3.4 Results and Discussion of ASTM D 3165 Specimens	3-30
3.4.1 Deformation Analysis (ASTM D 3165)	3-30
3.4.2 Stress Analysis (ASTM D 3165)	3-35
3.4.3 Failure Mode and Failure Criterion (ASTM D 3165)	3-39

3.5	Parameters Affecting Joint Performance	3-43
3.5.1	Adherend Thickness	3-43
3.5.2	Adherend Stiffness	3-45
3.5.3	Adherend Plasticity	3-47
4.	CONCLUSION	4-1
5.	REFERENCES	5-1
APPENDIX A—BOUNDARY CONDITIONS		

LIST OF FIGURES

Figure	Page
2-1 Joint Configuration and Coordinate Systems	2-1
2-2 Free-Body Diagram and Sign Conventions	2-3
2-3 Adhesive Stress Distribution From FEM (ABAQUS)	2-6
2-4 Adhesive von Mises Stress Distribution	2-8
2-5 Adhesive Peel Stress Distribution	2-8
2-6 Adhesive Shear Stress Distribution	2-9
3-1 ASTM D 5656 Specimen Geometry and Dimensions	3-1
3-2 Material Properties of PTM&W ES6292 Paste Adhesive	3-5
3-3 Comparison Between Experimental Results (ASTM D 5656) and FE Simulation Using Material Properties Data in Table 3-2	3-6
3-4 Symmetric Boundary Conditions at Center of ASTM D 5656 Specimen	3-7
3-5 ASTM D 3165 Specimen Geometry and Dimensions	3-8
3-6 Arbitrary Contour Around Tip of a Crack	3-9
3-7 Collapsed Two-Dimensional Element	3-10
3-8 Typical Focused Mesh for Fracture Mechanics Evaluation	3-10
3-9 Displacement of ASTM D 5656 Specimen With Bondline Thickness of 0.013" at Failure Load (1.41 kips)	3-12
3-10 Displacement of ASTM D 5656 Specimen With Bondline Thickness of 0.040" at Failure Load (1.34 kips)	3-12
3-11 Displacement of ASTM D 5656 Specimen With Bondline Thickness of 0.080" at Failure Load (1.26 kips)	3-13
3-12 Displacement of ASTM D 5656 Specimen With Bondline Thickness of 0.120" at Failure Load (1.05 kips)	3-13
3-13 Through-Thickness Average Adhesive Shear Strain Within Overlap at Each Respective Failure Load (ASTM D 5656)	3-14

3-14	Through-Thickness Average Adhesive Peel Strain Within Overlap at Each Respective Failure Load (ASTM D 5656)	3-14
3-15	Definition of Five Paths in Adhesive Layer	3-15
3-16	Adhesive Shear Stress Distribution (0.013" Bondline Thickness, ASTM D 5656)	3-16
3-17	Adhesive Shear Stress Distribution (0.04" Bondline Thickness, ASTM D 5656)	3-16
3-18	Adhesive Shear Stress Distribution (0.08" Bondline Thickness, ASTM D 5656)	3-17
3-19	Adhesive Shear Stress Distribution (0.12" Bondline Thickness, ASTM D 5656)	3-17
3-20	Five-Path Average Adhesive Shear Stress Distribution (ASTM D 5656)	3-18
3-21	Development of Shear Stress Distribution Along Path 3 (0.12" Bondline Thickness, ASTM D 5656)	3-19
3-22	Load Versus Joint-End Displacement (0.12" Bondline Thickness, ASTM D 5656)	3-19
3-23	Experimental Load Versus Apparent Adhesive Shear Strain Curves (ASTM D 5656)	3-21
3-24	Critical Locations Inside Adhesive Layer	3-21
3-25	Shear Stress at Critical Locations	3-22
3-26	Peel Stress at Critical Locations	3-22
3-27	PEEQ at Critical Locations	3-23
3-28	Calculated Apparent Shear Stress-Strain Curves for ASTM D 5656 Specimens	3-24
3-29	Experimental Apparent Shear Stress-Strain Curves for ASTM D 5656 Specimens	3-24
3-30	PEEQ Distribution in Adhesive With Bondline Thickness of 0.013" at Four Typical Stages	3-26
3-31	PEEQ Distribution in Adhesive With Bondline Thickness of 0.040" at Four Typical Stages	3-27
3-32	PEEQ Distribution in Adhesive With Bondline Thickness of 0.080" at Four Typical Stages	3-28
3-33	PEEQ Distribution in Adhesive With Bondline Thickness of 0.120" at Four Typical Stages	3-29
3-34	<i>J</i> -Integral for ASTM D 5656 of Specimens With Four Bondline Thicknesses	3-30

3-35	Displacement of ASTM D 3165 Specimen With Bondline Thickness of 0.013" at Failure Load (1.40 kips)	3-31
3-36	Displacement of ASTM D 3165 Specimen With Bondline Thickness of 0.040" at Failure Load (1.10 kips)	3-32
3-37	Displacement of ASTM D 3165 Specimen With Bondline Thickness of 0.080" at Failure Load (0.677 kips)	3-32
3-38	Displacement of ASTM D 3165 Specimen With Bondline Thickness of 0.120" at Failure Load (0.510 kips)	3-33
3-39	Through-Thickness Average Adhesive Shear Strain Within Overlap at Each Respective Failure Load (ASTM D 3165)	3-34
3-40	Through-Thickness Average Adhesive Peel Strain Within Overlap at Each Respective Failure Load (ASTM D 3165)	3-34
3-41	Adhesive Shear Stress Distribution (0.013" Bondline Thickness, ASTM D 3165)	3-35
3-42	Adhesive Shear Stress Distribution (0.040" Bondline Thickness, ASTM D 3165)	3-36
3-43	Adhesive Shear Stress Distribution (0.080" Bondline Thickness, ASTM D 3165)	3-36
3-44	Adhesive Shear Stress Distribution (0.120" Bondline Thickness, ASTM D 3165)	3-37
3-45	Five-Path Average Adhesive Shear Stress Distribution (ASTM D 3165)	3-37
3-46	Development of Shear Stress Distribution Along Path 3 (0.12" Bondline Thickness, ASTM D 3165)	3-38
3-47	Load Versus Joint-End Displacement (0.12" Bondline Thickness, ASTM D 3165)	3-38
3-48	Load Versus Joint-End Displacement (ASTM D 3165)	3-39
3-49	Critical Location Inside Adhesive Layer (ASTM D 3165)	3-40
3-50	Adhesive Shear Stress Versus Load At Location 1 (ASTM D 3165)	3-40
3-51	Adhesive Peel Stress Versus Load At Location 1 (ASTM D 3165)	3-41
3-52	PEEQ Versus Load At Location 1 (ASTM D 3165)	3-41
3-53	<i>J</i> -Integral Versus Load At Location 1 (ASTM D 3165)	3-42
3-54	<i>J</i> -Integral for ASTM D 3165 Configuration With Double Adherend Thickness	3-43
3-55	<i>J</i> -Integral for ASTM D 3165 Configuration With Triple Adherend Thickness	3-44

3-56	Failure Load Versus Adherend Thickness	3-44
3-57	<i>J</i> -Integral Versus Load for With Different Adherend Young's Moduli (0.013" Bondline Thickness, ASTM D 3165)	3-45
3-58	Failure Load Versus Adherend Young's Modulus (0.013" Bondline Thickness, ASTM D 3165)	3-46
3-59	<i>J</i> -Integral Versus Load for With Different Adherend Young's Moduli (0.013" Bondline Thickness, ASTM D 5656)	3-46
3-60	Failure Load Versus Adherend Young's Modulus (0.013" Bondline Thickness, ASTM D 5656)	3-47
3-61	Comparison Between Different Material Models for Aluminum Adherends (0.04" Bondline Thickness, ASTM D 3165)	3-48
3-62.	Comparison Between Different Material Models for Aluminum Adherends (0.08" Bondline Thickness, ASTM D 3165)	3-48

LIST OF TABLES

Table	Page
2-1 Values of $Index_1$ From Test Results (MPa)	2-9
2-2 Values of $Index_2$ From Test Results (MPa)	2-10
2-3 Values of $Index_3$ From Test Results (in/in)	2-10
3-1 Number of Elements and Aspect Ratio of Finite Element Models (ASTM D 5656)	3-1
3-2 Postyielding Behaviors of PTM&W ES6269 Adhesive	3-5
3-3 Number of Elements and Aspect Ratio of Finite Element Models (ASTM D 3165)	3-8
3-4 Angle of Rotation of Overlap Area of ASTM D 5656 Specimens at Failure Load	3-11
3-5 Adhesive Shear Modulus	3-18
3-6 Experimental and Predicted Failure Loads by J -Integral Criterion (ASTM D 5656)	3-30
3-7 Angle of Rotation of Overlap Area of ASTM D 3165 Specimens at Failure Load	3-33
3-8 Corresponding Values at Failure Loads for ASTM D 3165	3-42
3-9 Comparison of Predicted Failure Loads With Experimental Results for ASTM D 3165 Using $J_c = 4$ psi-in	3-42

EXECUTIVE SUMMARY

While the general aviation industry increasingly uses adhesive bond for airframe composite structures, two issues have become particularly important: certification of adhesives used and certification of adhesive joints. A generally agreed-upon design methodology for adhesive-bonded composite joints, especially the failure criterion, is lacking. Typically, three failure modes of adhesive-bonded composite joints exist: (1) adherend failure, (2) adhesive failure (failure at the adhesive/adherend interface), and (3) cohesive failure (failure within the adhesive layer). A previous report (DOT/FAA/AR-01/57, 2001) included an analytical model development for adherend failure mode. This report describes the investigation of adhesive and cohesive failure modes.

This report includes two parts. The first part comprises the derivation of an analytical model for predicting adhesive stress distribution within the joint specimens of ASTM D 3165. Elastic orthotropic adherends and elastic-perfectly plastic adhesive were used in the model development. The developed stress model was verified with finite element models by comparing the adhesive stress distributions. Failure analysis was conducted based on three failure criteria. Predicted strengths were compared with test data. The second part of this report contains finite element approaches for analyzing adhesive and cohesive failure modes. The equivalent plastic strain and J -integral were used as the failure criteria for cohesive and adhesive failure modes, respectively. Experimental data was used to establish the values of the equivalent plastic strain and the critical value of J -integral (J_c).

1. INTRODUCTION.

Advanced composite materials have been widely used due to their lightweight and high-corrosion resistance. In many applications, bolted joints have been replaced by adhesive-bonded joints because of the weight penalty and corrosion problems associated with bolted joints. Many certification-related issues become more important as the application of adhesive-bonded joints gains in popularity in the general aviation industry. The objectives of this study are two-fold: (1) to provide an analytical model to predict the adhesive stress distribution within an adhesive-bonded joint using elastic-perfectly plastic adhesive properties and to investigate the cohesive failure mode, and (2) to use finite element methods to investigate the cohesive and adhesive failure modes of adhesive-bonded joints.

Earlier studies on adhesive-bonded joints can be found from reviewing papers by Kutscha [1], Kutscha and Hofer [2], Matthews, et al. [3], and Vinson [4]. When studying adhesive-bonded lap joints, the effects due to the rotation of the adherends were first taken into account by Goland and Reissner [5]. They introduced an equation to relate the bending moment of the adherend at the end of the overlap to the in-plane loading. The basic approach of the Goland and Reissner theory was based on beam theory or, rather, on cylindrically bent-plate theory, which treated the overlap section as a beam of twice the thickness of the adherend. Hart-Smith [6-9] published a series of papers regarding single-lap, double-lap, scarf, and stepped-lap joints involving a continuum mechanics model in which the adherends were isotropic or anisotropic elastic, and the adhesive was modeled as elastic, elastic-plastic, or bielastic. Basically, classical plate theory was adopted during Hart-Smith's derivation. However, the effects of transverse shear deformation, which has been shown to be important when the span-to-depth ratio or the transverse shear modulus is small (Reissner [10] and Reddy [11]), were not included in either Goland and Reissner or Hart-Smith's theories. Moreover, edge effects were neglected, and adhesive stresses were assumed to be constant through the thickness in most of the analyses found in the literature.

Renton and Vinson [12] used a higher order formulation that includes the adherend transverse shear and normal strains to analyze adhesive-bonded joints. Their results were compared with photoelastic experiments and show excellent agreement, except for local stress concentrations at the edges of the overlap region. Yang, et al. [13] studied double-lap composite joints under cantilevered bending and developed a strain gap model to describe the stress-strain behavior. Yang and Pang [14 and 15] also derived analytical models for adhesive-bonded composite single-lap joints under cylindrical bending and tension based on the laminated anisotropic plate theory. Their approach correlated the asymmetry of the adherend laminates as well as the effects due to the transverse shear deformation. Oplinger [16] studied single-lap joints with isotropic adherends and found that many of the predictions of the Goland-Reissner analysis are recovered in the limit of large adherend-to-adhesive layer thickness ratios, although substantial differences from the Goland-Reissner analysis can occur for relatively thin adherends.

In 1997, Tong [17] studied the strength of adhesive-bonded double-lap composite joints. Due to the fact that failure often occurs at the resin-fiber interface adjacent to the adhesive, Tong used a simplified one-dimensional model as well as a finite element model in conjunction with several existing and new interlaminar failure criteria to predict the strength of joints. In 1996, Adams and Davies [18] published the results of their nonlinear finite element analysis on single-lap adhesive-bonded joints of composite/steel and composite/aluminum with different taper

arrangements at the edges of joints. An experimental study of the effects of adherend layup sequence on joint strength following ASTM D 1002 was published by Thomas, et al. [19] in 1998.

Many researchers investigated the failure of adhesive-bonded joints. To name a few, the linear elastic fracture mechanics approach was used by Chai [20 and 21] and Chai and Chiang [22]. They used the Butterfly and the End-Notch Flexure adhesive-bond specimens to establish a crack propagation criterion for adhesive bonds. Dynamic crack growth of bonds was investigated by Needleman and Rosakis [23]. The finite element method has been widely used to analyze adhesive-bonded composite structures as well as adhesive-bonded repairs. Among these researchers, Charalambides, et al. [24 and 25] studied bonded repairs under static and fatigue loading, experimentally as well as using elastic-plastic finite element models.

Although finite element analysis can solve many mechanical problems with different materials and configurations, analytical solutions are still preferred to perform parametric analyses such as optimization. In the first part of this report, an analytical model is derived to determine the stress and strain distributions of adhesive-bonded composite single-lap joints under tension. In the model development, the laminated anisotropic plate theory is applied in the derivation of the governing equations of the two bonded laminates. The adhesive is assumed to be very thin, and the adhesive stresses are assumed constant through the bondline thickness. The composite adherends are assumed linear elastic while the adhesive is assumed elastic-perfectly plastic following von Mises yield criterion. The entire coupled system is then determined through the kinematics and force equilibrium of the adhesive and the adherends. The overall system of governing equations is solved analytically with appropriate boundary conditions. The computer software, Maple V, is used as the solution tool. Results from the analytical model are verified with finite element analysis using ABAQUS. The three major failure modes of adhesive-bonded joints are: (1) adherend failure, (2) cohesive failure, and (3) adhesive failure. While the adherend failure mode was investigated and reported in the previous report (DOT/FAA/AR-01/57, 2001), the current report includes cohesive and adhesive failure modes. The analytical model developed in this investigation is used to predict the cohesive failure using experimental results from ASTM D 3165-95 "Strength Properties of Adhesives in Shear by Tension Loading of Single-Lap-Joint Laminated Assemblies" test specimen configurations.

The second part of this report describes the finite element analyses of test specimens specified in both ASTM D 3165 and ASTM D 5656-95 test standards. Both cohesive and adhesive failure modes are included in the finite element analyses.

2. ANALYTICAL MODEL ON ASTM D 3165 SPECIMEN.

As described previously, an analytical model is developed to predict the stress and strain distributions within an adhesive-bonded joint. In the model, the laminated anisotropic plate theory describes the behavior of the adherends. The adhesive is assumed to be elastic-perfectly plastic and to follow von Mises yield criterion. The entire system of coupled ordinary differential equations is solved by using a symbolic solver, Maple V [26]. Finite element analysis is conducted to confirm the adhesive stress distributions obtained from the developed model. Cohesive failure is investigated using the developed model and experimental results.

2.1 MODEL DERIVATION.

Figure 2-1 shows the configuration of a single-lap joint following ASTM D 3165 configuration. The tensile load in the x direction, defined as P , represents the load per unit width. As shown below, the joint is divided into three regions for convenience in the model development. There is an adhesive plastic zone at each edge of the overlap within which the adhesive shear stress reaches its yield strength.

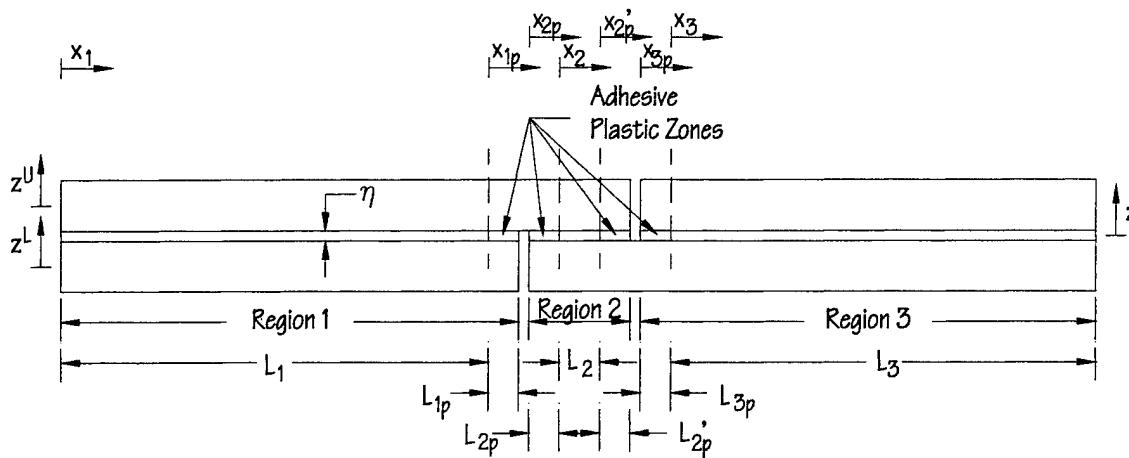


FIGURE 2-1. JOINT CONFIGURATION AND COORDINATE SYSTEMS

2.1.1 Adherend Formulation.

The generalized formulas of the adherends and adhesive are the same for all three regions. The upper and lower adherends are assumed to follow the first-order laminated plate theory. The displacement field of the two adherends, u in the x direction and w in the z direction, can be written as follows:

$$u^U = u^{oU}(x) + z^U \psi^U(x) \quad (2-1)$$

$$u^L = u^{oL}(x) + z^L \psi^L(x) \quad (2-2)$$

$$w^U = w^U(x) \quad (2-3)$$

$$w^L = w^L(x) \quad (2-4)$$

where superscript U and L denote the upper and lower adherends, respectively, superscript o represents the mid-plane displacement, and ψ is the corresponding bending slope. After substituting equations 2-1 through 2-4 into the strain displacement relations together with the equivalent modulus matrices $[A]$, $[B]$, and $[D]$ for orthotropic laminates, the normal stress resultant N_x , bending moment for unit width M_y , and transverse shear stress resultant Q_z can be obtained as follows:

$$N_x = A_{11} \frac{du^o(x)}{dx} + B_{11} \frac{d\psi(x)}{dx} \quad (2-5)$$

$$M_y = B_{11} \frac{du^o(x)}{dx} + D_{11} \frac{d\psi(x)}{dx} \quad (2-6)$$

$$Q_z = k_s A_{55} \left(\psi(x) + \frac{dw(x)}{dx} \right) \quad (2-7)$$

where k_s is the shear correction factor. In order to establish the equations of equilibrium, a free-body diagram of the adherends and adhesive is shown in figure 2-2. The equations for force equilibrium of the upper adherend are then as follows:

$$\frac{dN_x^U}{dx} = -\tau_{xz} \quad (2-8)$$

$$\frac{dM_y^U}{dx} = Q_z^U + \frac{h^U}{2} \tau_{xz} \quad (2-9)$$

$$\frac{dQ_z^U}{dx} = \sigma_z \quad (2-10)$$

where τ_{xz} and σ_z are the shear and peel stresses of the adhesive, respectively, and h^U is the thickness of the upper adherend. Three equilibrium equations can be obtained for the lower adherend in the same fashion.

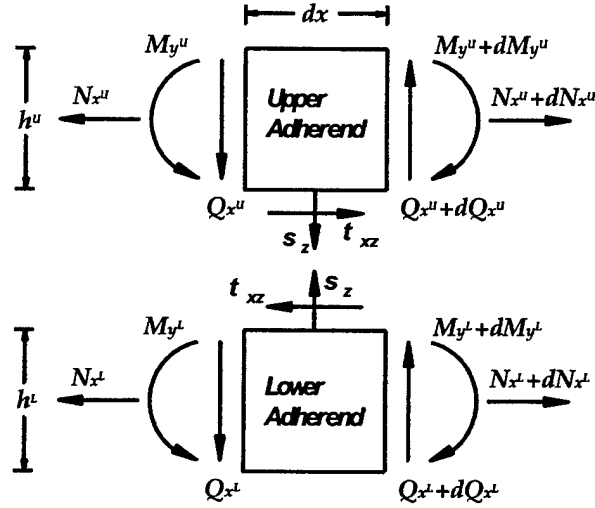


FIGURE 2-2. FREE-BODY DIAGRAM AND SIGN CONVENTIONS

2.1.2 Adhesive Behavior in Elastic Regions.

Assuming a perfect bond between the adhesive and the adherend surfaces, based on the kinematics of the adherends, the adhesive strains are related to the bottom surface of the upper adherend and to the top surface of the lower adherend. In terms of the displacement field of the two adherends, the adhesive strains can be written as follows:

$$\gamma_{xz} = \left[(u^{oL} - u^{oU}) + \left(\frac{h^L}{2} \psi^L + \frac{h^U}{2} \psi^U \right) - \frac{1}{2} \left(\frac{dw^L}{dx} + \frac{dw^U}{dx} \right) \right] / \eta \quad (2-11)$$

$$\varepsilon_x = \frac{1}{2} \frac{d}{dx} \left[(u^{oL} + u^{oU}) + \left(\frac{h^L}{2} \psi^L - \frac{h^U}{2} \psi^U \right) \right] \quad (2-12)$$

$$\varepsilon_z = \frac{1}{\eta} (w^U - w^L) \quad (2-13)$$

where η is the adhesive thickness. Under plane-strain condition, the adhesive stresses can be obtained as follows:

$$\sigma_x = \frac{E}{(1+\nu)(1-2\nu)} [(1-\nu)\varepsilon_x + \nu\varepsilon_z] \quad (2-14)$$

$$\sigma_y = \frac{\nu E}{(1+\nu)(1-2\nu)} (\varepsilon_x + \varepsilon_z) \quad (2-15)$$

$$\sigma_z = \frac{E}{(1+\nu)(1-2\nu)} [\nu\varepsilon_x + (1-\nu)\varepsilon_z] \quad (2-16)$$

and

$$\tau_{xz} = G \gamma_{xz} \quad (2-17)$$

2.1.3 Adhesive Behavior in Plastic Regions.

High adhesive stresses at the vicinity of the joint edges are expected. Therefore, it is necessary to assume a plastic zone near each of the edges where adhesive yielding is considered.

Based on Prandtl-Reuss material model, the plastic strain increment is expressed by the flow rule:

$$d\epsilon_{ij}^p = \frac{\partial g}{\partial \sigma_{ij}} d\lambda \quad (2-18)$$

where ϵ_{ij} and σ_{ij} are the strain and stress tensors of the adhesive, respectively, and g is plastic potential. When elastic-perfectly plastic behavior following von Mises yield criterion is assumed for the adhesive, the plastic potential can be assumed as follows:

$$g = J_2 = \frac{1}{2} s_{ij} s_{ji} \quad (2-19)$$

Therefore, equation 2-18 can be written as follows:

$$\frac{d\epsilon_x^p}{s_x} = \frac{d\epsilon_y^p}{s_y} = \frac{d\epsilon_z^p}{s_z} = \frac{d\gamma_{xy}^p}{\tau_{xy}} = \frac{d\gamma_{yz}^p}{\tau_{yz}} = \frac{d\gamma_{zx}^p}{\tau_{zx}} = d\lambda \quad (2-20)$$

Also, for a perfectly plastic material, the equation can be written as follows:

$$d\sigma_{ij} = 2Gde_{ij} + Kd\epsilon_{kk}\delta_{ij} - \frac{Gs_{mn}de_{mn}}{k^2}s_{ij} \quad (2-21)$$

where e_{ij} is the deviatoric strain tensor, δ_{ij} is the Kronecker delta, $k = (J_2)^2$, J_2 is the second invariant of the deviatoric stress tensor, G is the shear modulus, and

$$K = \frac{E}{3(1-2\nu)} \quad (2-22)$$

von Mises stress σ' can be expressed in terms of the deviatoric stresses and the shear stress as follows:

$$\sigma' = \sqrt{\frac{3}{2}(s_x^2 + s_y^2 + s_z^2) + 3\tau_{xz}^2} \quad (2-23)$$

By assuming that the shear stress τ_{xz} is much greater than all the three deviatoric stress components when the adhesive reaches the yield stress at the edges of the joint, then

$$\tau_{xz} = \frac{\sigma_{yield}}{\sqrt{3}} \quad (2-24)$$

and

$$s_x \approx 0 \quad s_y \approx 0 \quad s_z \approx 0 \quad (2-25)$$

Based on this assumption and equation 2-21, it can be shown that $d\sigma_x \approx d\sigma_y \approx d\sigma_z \approx 0$ after the adhesive reaches yield strength. Therefore, the adhesive behavior in the plastic zones is as follows:

$$\sigma_x = \frac{E}{(1+\nu)(1-2\nu)} [(1-\nu)\epsilon_x + \nu\epsilon_z] \quad (2-26)$$

$$\sigma_y = \frac{\nu E}{(1+\nu)(1-2\nu)} (\epsilon_x + \epsilon_z) \quad (2-27)$$

$$\sigma_z = \frac{E}{(1+\nu)(1-2\nu)} [\nu\epsilon_x + (1-\nu)\epsilon_z] \quad (2-28)$$

and

$$\tau_{xz} = \tau_p = \frac{\sigma_{yield}}{\sqrt{3}} \quad (2-29)$$

This assumption is verified by the finite element analysis using ABAQUS. Figure 2-3 shows the adhesive stress distribution in region 2, as specified in figure 2-1. It can be seen that the shear stress is almost constant within the adhesive plastic zones, while the von Mises stress remains constant.

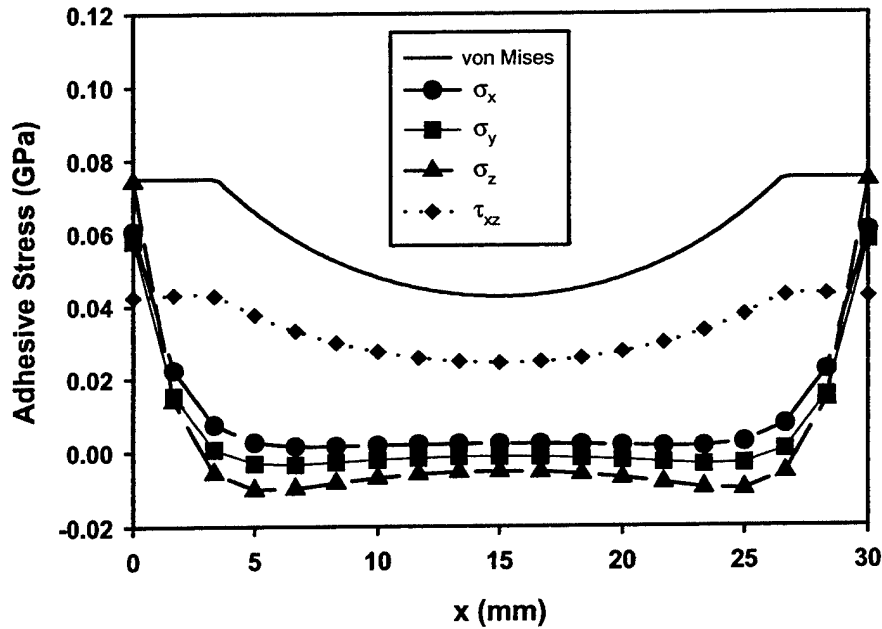


FIGURE 2-3. ADHESIVE STRESS DISTRIBUTION FROM FEM (ABAQUS)

Because the adhesive shear stress is assumed constant within the plastic zone, the von Mises stress calculated based on equation 2-23 is no longer a constant. A factor is then applied to each of the stress components to scale down the von Mises stress to the value of the yield stress σ_{yield} . Due to the symmetry of the joint system, the length of the plastic zone in region 1 (L_{1p}) is the same as the length of the plastic zone in region 3 (L_{3p}) and the two plastic zones in region 2 have the same length ($L_{2p} = L_{2p}'$).

2.1.4 Solution Procedure.

The overall system of governing equations includes 42 coupled second-order ordinary differential equations (six equations for each zone) with 42 variables (u^{oU} , ψ^U , w^U , u^{oL} , ψ^L , and w^L for each zone). A total of 84 boundary conditions are obtained at the ends of each zone from either continuity or applied force conditions, as shown in figure 2-1. These boundary conditions are listed in appendix A. The solution procedure starts with assumed plastic zone lengths, L_{1p} and L_{2p} . Solutions to the differential equations are obtained by using a symbolic solver, Maple V [26], with the Laplace option. Once the Laplace option is chosen, Maple V performs forward and inverse Laplace transformations to obtain the exact solutions to the system of ordinary differential equations. Based on the solutions, the von Mises (σ') stresses in the plastic zones are calculated. The lengths of the plastic zones for the next iteration are adjusted by multiplying $(\sigma'/\sigma_{yield})^2$ by the plastic zone lengths of the previous iterations. Iteration continues until the calculated von Mises stresses σ' converge to the value of yield stress σ_{yield} .

2.2 RESULTS AND DISCUSSION.

To demonstrate the application of the developed model, a joint system as described in figure 2-1 is modeled using both the developed model and finite element software ABAQUS. In this

illustration, T300/5208 (Graphite/Epoxy) with a ply thickness of 0.25 mm was used for both upper and lower adherends. Each adherend consists of 12 plies with orientation and sequence of $[0_3/90_3]_S$. The engineering constants of T300/5208 are as follows:

$$E_{11} = 181 \text{ GPa} \quad E_{22} = 10.3 \text{ GPa} \quad G_{12} = 7.17 \text{ GPa} \quad \nu_{12} = 0.28$$

For convenience, other mechanical properties of the adherends are assumed as $E_{33} = E_{22}$, $G_{13} = G_{12}$, $\nu_{13} = \nu_{12}$, $\nu_{23} = 0.35$, and $G_{23} = E_{22}/(2 + 2\nu_{23}) = 3.815 \text{ GPa}$. Based on the material properties above, the mechanical constants of the adherends per unit width can be given as follows:

$$\begin{aligned} A_{11}^U = A_{11}^L &= 374 \text{ kN/mm} & B_{11}^U = B_{11}^L &= 0 \\ D_{11}^U = D_{11}^L &= 394 \text{ kNmm} & A_{55}^U = A_{55}^L &= 18.2 \text{ kN/mm} \end{aligned}$$

The adhesive is Metbond 408 with the following properties:

$$\begin{aligned} E &= 0.96 \text{ GPa} & G &= 0.34 \text{ GPa} \\ \nu &= 0.41 & \sigma_{\text{yield}} &= 7.5 \text{ MPa} \end{aligned}$$

The joint dimensions include $L_1 = L_3 = 80 \text{ mm}$, $L_2 = 30 \text{ mm}$, and $\eta = 0.2 \text{ mm}$. The applied tensile load is $P = 0.1 \text{ kN/mm}$.

Figure 2-4 shows the von Mises stress distribution obtained from both the developed model and finite element model. A good correlation can be seen from the size of the adhesive plastic zone and the stress level in the entire overlap region. Figures 2-5 and 2-6 show the adhesive peel stress (σ_z) and shear stress distributions, respectively, obtained from the developed model and the finite element model. It can be seen that the reduced value of shear stress at the ends of the overlap can be obtained following scaling, as previously described.

Joint strength can be predicted if a suitable joint failure criterion is established. Experimental results using ASTM D 3165 specimens with PTM&W ES6292 paste adhesive from previous investigation (reported in DOT/FAA/AR-01/33) are used for the establishment of a valid joint failure criterion. The yield strength (σ_{yield}) of PTM&W ES6292 is 41.37 MPa based on previous test results.

Several proposed criteria include the following: (1) hydrostatic stress at certain locations such as 5% of overlap length from the edges of the joint, (2) average hydrostatic stress over a portion of the overlap length, and (3) average plastic strain over a portion of the overlap length. The results all show good correlation with test results. The index using the hydrostatic stress of the adhesive at certain locations of the overlap can be expressed as follows:

$$Index_1 = \frac{1}{3}(\sigma_x + \sigma_y + \sigma_z) \quad (2-30)$$

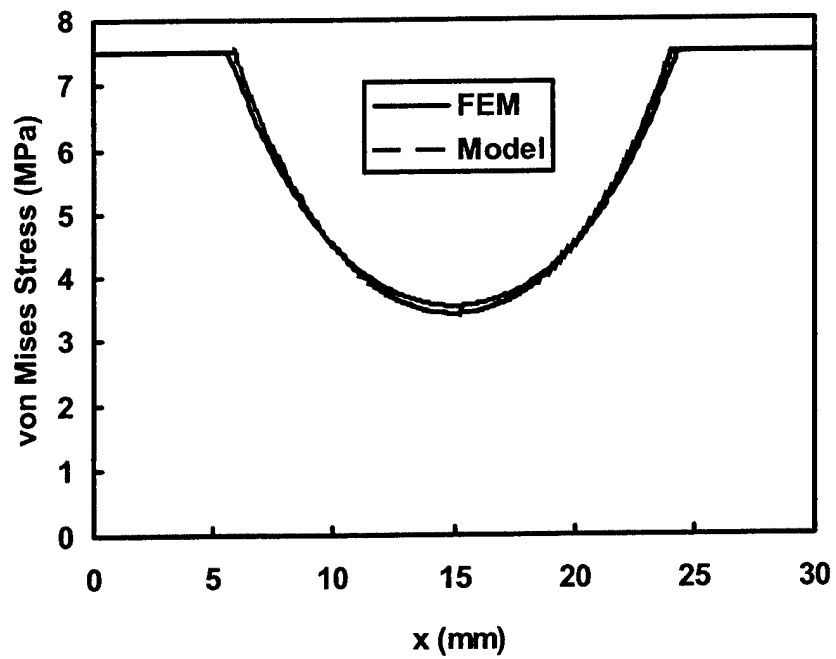


FIGURE 2-4. ADHESIVE VON MISES STRESS DISTRIBUTION

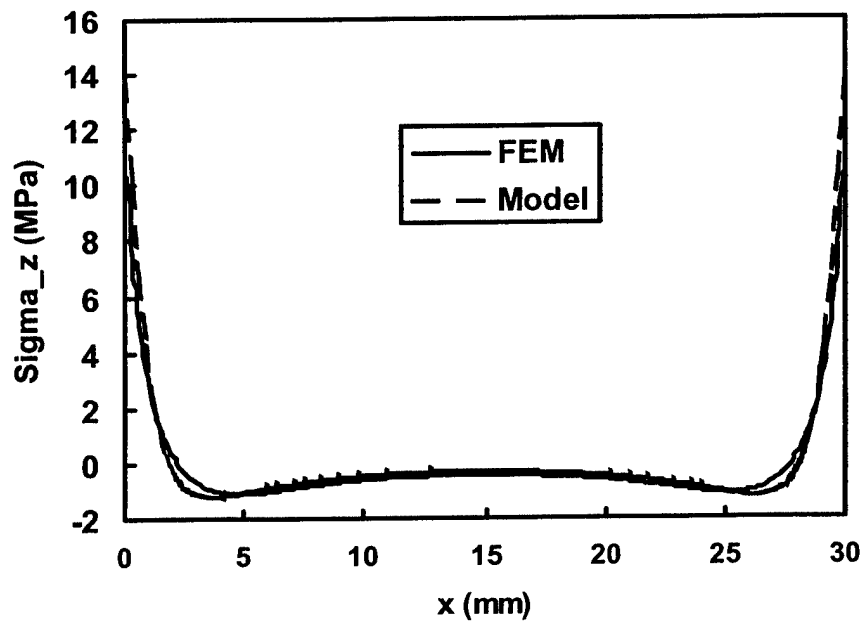


FIGURE 2-5. ADHESIVE PEEL STRESS DISTRIBUTION

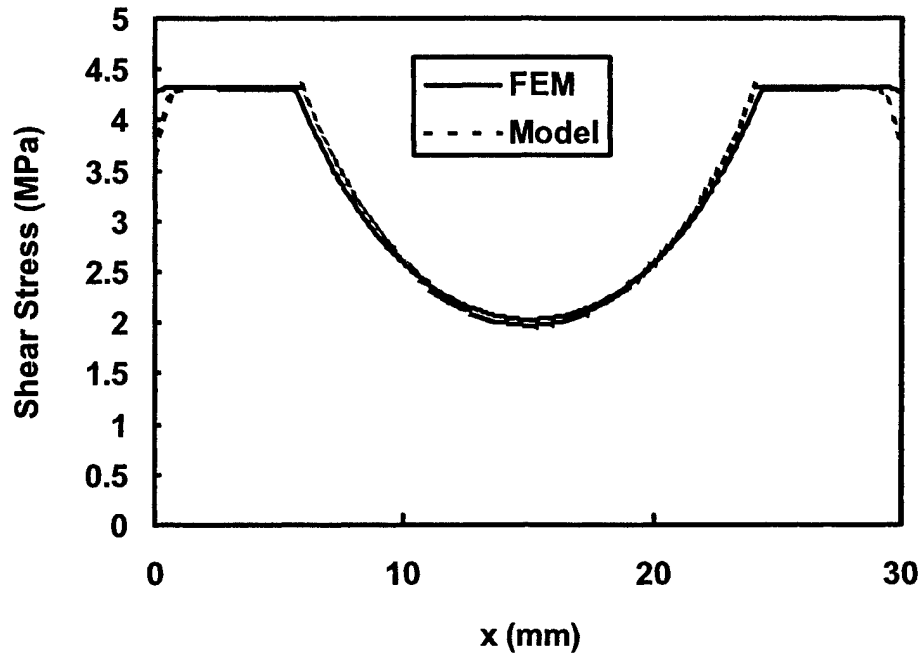


FIGURE 2-6. ADHESIVE SHEAR STRESS DISTRIBUTION

Table 2-1 provides the $Index_1$ values at $\alpha\%$ of L_2 from the overlap edge using test results.

TABLE 2-1. VALUES OF $INDEX_1$ FROM TEST RESULTS (MPa)

A	0	2	3	4	5
Sample No. 1	35.65	28.54	24.82	21.10	17.51
Sample No. 2	36.40	29.23	25.44	21.65	18.00
Sample No. 3	39.23	31.44	27.10	22.75	18.48
Sample No. 4	37.16	29.79	25.92	21.93	18.13
Sample No. 5	39.78	31.85	27.44	22.96	18.55
Average	37.65	30.17	26.15	22.08	18.13
Std. Dev.	18.91	1.42	1.10	0.77	0.42

If the average hydrostatic stress within a certain portion close to the edges of the overlap is used as failure criterion, $Index_2$ is written as follows:

$$Index_2 = \frac{\int_0^{\alpha\beta} \frac{1}{3} (\sigma_x + \sigma_y + \sigma_z) dx}{\alpha\beta} \quad (2-31)$$

Table 2-2 provides the values of $Index_2$ from test results.

TABLE 2-2. VALUES OF $INDEX_2$ FROM TEST RESULTS (MPa)

A	β = Overlap Length		β = Adhesive Plastic Region		
	5%	8%	10%	30%	50%
Sample No. 1	31.10	28.54	33.92	30.48	27.30
Sample No. 2	31.85	29.23	34.47	30.75	27.30
Sample No. 3	41.23	31.44	37.03	32.54	28.48
Sample No. 4	32.47	29.79	35.16	31.23	27.58
Sample No. 5	34.75	31.85	37.44	32.89	28.61
Average	34.28	30.17	35.60	31.58	27.85
Std. Dev.	17.63	1.42	1.56	1.08	0.64

If the average adhesive plastic strain is used to evaluate failure, $Index_3$ is as follows:

$$Index_3 = \frac{\int_0^{\alpha\beta} \gamma^p dx}{\alpha\beta} \quad (2-32)$$

Table 2-3 provides the values of $Index_3$ from test results.

TABLE 2-3. VALUES OF $INDEX_3$ FROM TEST RESULTS (in/in)

A	β = Overlap Length			β = Adhesive Plastic Region		
	3%	5%	8%	10%	30%	50%
Sample No. 1	0.0435	0.0401	0.0353	0.0455	0.0389	0.0330
Sample No. 2	0.0480	0.0444	0.0395	0.0496	0.0423	0.0358
Sample No. 3	0.0640	0.0596	0.0533	0.0657	0.0557	0.0469
Sample No. 4	0.0517	0.0480	0.0427	0.0534	0.0454	0.0383
Sample No. 5	0.0675	0.0628	0.0562	0.0692	0.0585	0.0492
Average	0.0549	0.0510	0.0454	0.0567	0.0482	0.0406
Std. Dev.	0.0104	0.0098	0.0090	0.0103	0.0085	0.0071

The validation of the developed analytical model can be justified based on the reasonable correlations between the stress distributions obtained from the developed analytical model and the finite element model. However, due to the fact that most of the composite joints failed at the adherends instead of the adhesive in the experiments conducted on ASTM D 3165 specimens, there is not sufficient data to establish a reliable failure criterion. In tables 2-1 through 2-3, results from only five specimens are used to establish the failure criterion. More data points would be necessary for the development of a valid failure criterion. This would be feasible only if a ductile and relatively weak adhesive is to be used.

3. FINITE ELEMENT ANALYSES OF ASTM D 5656 AND ASTM D 3165 SPECIMENS.

3.1 FINITE ELEMENT MODELS OF ASTM D 5656 SPECIMENS.

The ASTM D 5656 test standard allows one to obtain the stress-strain relationship of adhesives. From the test, one can determine the adhesive's apparent shear modulus, the stress and strain at the proportional limit, and the failure load of the joint. The specimen is loaded at both ends, while the relative displacement of the two adherends is recorded using the KGR-1 device. The thick nature of the adherends causes them to have a high rigidity in both tension and bending. The displacement of the adherends in the gauge section is fairly uniform. The ASTM D 5656 specimen geometry and dimensions are shown in figure 3-1.

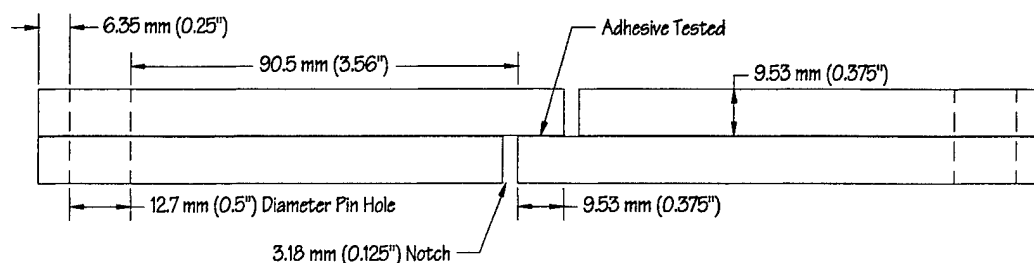


FIGURE 3-1. ASTM D 5656 SPECIMEN GEOMETRY AND DIMENSIONS

To simulate the mechanical behavior of the joint, including stress distributions and failure, two-dimensional (2-D) finite element models with four-node elements are constructed for specimens with bondline thicknesses of 0.013", 0.04", 0.08", and 0.12". The number of elements of the entire specimen, the number of elements of the adhesive, and the element aspect ratios are provided in table 3-1.

TABLE 3-1. NUMBER OF ELEMENTS AND ASPECT RATIO OF FINITE ELEMENT MODELS (ASTM D 5656)

FE Model	Adhesive Thickness (in)	Number of Elements of Entire Model	Number of Elements of Adhesive	Number of Elements Through Adhesive Thickness	Largest Element Aspect Ratio of Adhesive
D 5656_1	0.013	13,420	400	8	5.4
D 5656_2	0.040	10,208	700	14	3.1
D 5656_3	0.080	8,204	900	18	2.1
D 5656_4	0.120	7,864	880	22	2.3

The following techniques are used in the finite element analyses.

3.1.1 Explicit Direct-Integration Dynamic Analysis.

This method is appropriate for quasi-static analysis of large models with nonlinear material properties and large deformation. The explicit direct-integration dynamic analysis is available in ABAQUS/Explicit. It is based on the implementation of explicit central difference integration together with the use of diagonal element mass matrices. The explicit schemes obtain values for dynamic quantities at $t + \Delta t$ directly from the available values at time t , which is efficient for each time increment. Therefore, a large number of small time increments are performed effectively. However, the central difference operator is conditionally stable. The stability limit (the largest time step) is approximately equal to the time for an elastic wave to move across the smallest element in the model. In the present analysis, the time increments are determined automatically by ABAQUS/Explicit within the stability limit. Moreover, the mass scaling method is used in the calculation to expedite the simulation process.

3.1.2 Nonlinear Analysis for Both Adhesive and Adherends.

Both geometry and material nonlinearity are included in the finite element simulation. To include material nonlinearity, the von Mises yield criterion with isotropic hardening and the associated plastic flow are used, which can be expressed in equations 3-1 and 3-2.

$$f = \sqrt{J_2} - k(\epsilon_p) = 0 \quad (3-1)$$

$$d\epsilon_{ij}^p = d\lambda \frac{\partial f}{\partial \sigma_{ij}} \quad (3-2)$$

where J_2 is the second invariant of the deviatoric stress tensor; k is the value defining the occurrence of material yielding, which is a function of effective plastic strain ϵ_p for isotropic hardening materials; $d\lambda$ is a positive scalar factor of proportionality; f is von Mises yield function; and σ_{ij} and ϵ_{ij}^p are stress tensor and plastic strain tensor, respectively. The effective plastic strain ϵ_p is defined as follows:

$$\epsilon_p = \sqrt{\frac{2}{3} \sum_{i,j=1,2,3} \epsilon_{ij}^p \epsilon_{ij}^p} \quad (3-3)$$

The incremental stress-strain relation can be generally expressed as follows:

$$d\sigma_{ij} = \sum_{k,l=1,2,3} (C_{ijkl} + C_{ijkl}^p) d\epsilon_{kl} \quad (3-4)$$

where $i, j = 1, 2, 3$, the incremental stress tensor $d\sigma_{ij}$ and strain tensors $d\epsilon_{ij}$ can be written in vector forms as follows:

$$\{d\sigma\}^T = \{d\sigma_x d\sigma_y d\sigma_z d\tau_{yz} d\tau_{zx} d\tau_{zy}\} \quad (3-5)$$

$$\{d\epsilon\}^T = \{d\epsilon_x d\epsilon_y d\epsilon_z d\epsilon_{yz} d\epsilon_{zx} d\epsilon_{xy}\} \quad (3-6)$$

The tensor of elastic modulus C_{ijkl} and C_{ijkl}^p are expressed in the following matrix forms:

$$[C] = \begin{bmatrix} K + \frac{4}{3}G & & & & & \\ & K - \frac{2}{3}G & K + \frac{4}{3}G & & & \\ & K - \frac{2}{3}G & K - \frac{2}{3}G & K + \frac{4}{3}G & & \\ & 0 & 0 & 0 & G & \\ & 0 & 0 & 0 & 0 & G \\ & 0 & 0 & 0 & 0 & 0 & G \end{bmatrix} \quad \text{sym.} \quad (3-7)$$

$$[C^p] = -\frac{9G^2}{(3G + H_p)\sigma_e^2} \begin{bmatrix} s_x^2 & & & & & \\ s_y s_x & s_y^2 & & & & \\ s_z s_x & s_z s_y & s_z^2 & & & \\ s_{yz} s_x & s_{yz} s_y & s_{yz} s_z & s_{yz}^2 & & \\ s_{zx} s_x & s_{zx} s_y & s_{zx} s_z & s_{zx} s_{yz} & s_{zx}^2 & \\ s_{xy} s_x & s_{xy} s_y & s_{xy} s_z & s_{xy} s_{yz} & s_{xy} s_{zx} & s_{xy}^2 \end{bmatrix} \quad (3-8)$$

where, $s_x, s_y, s_z, s_{xy}, s_{yz}$, and s_{zx} are the reduced stress deviatoric tensors, and G and K are the shear and bulk moduli, respectively. H_p and the effective stress σ_e are expressed as follows:

$$H_p = \frac{d\sigma_e}{d\epsilon_p} \quad (3-9)$$

$$\sigma_e = \sqrt{3J_2} \quad (3-10)$$

Actually, H_p is the slope of the uniaxial true stress/true plastic strain curve, which is required by ABAQUS as input data.

The material used for the adherends is 2024-T351 aluminum. Its material properties are simulated using an elastic-perfectly plastic model with Young's modulus of 10.6 Msi, Poisson's ratio of 0.3, and yield stress of 47 ksi.

PTM&W ES6269 paste adhesive is used in the finite element analyses using the elastic-plastic material model with isotropic hardening. In the elastic range, the Young's modulus of the adhesive is 275 ksi and the Poisson's ratio is 0.3. The postyielding behavior required by ABAQUS is a plastic strain/true stress curve. Because the material data is usually available in

values of nominal stress and strain, it is necessary to convert the nominal stress/strain relation to the true stress/strain relation before it can be used by ABAQUS. The true strain or logarithmic strain ϵ and true stress σ are defined as follows:

$$\epsilon = \int_{l_0}^l \frac{dl}{l} = \ln\left(\frac{l}{l_0}\right) \quad (3-11)$$

$$\sigma = \frac{F}{A} \quad (3-12)$$

where l is length, l_0 is the original length, F is the applied force, and A is the cross-sectional area. According to the definitions, the relations among true stress, true strain, nominal stress, and nominal strain are as follows:

$$\sigma = \sigma_{nom}(1 + \epsilon_{nom}) \quad (3-13)$$

$$\epsilon = \ln(1 + \epsilon_{nom}) \quad (3-14)$$

The plastic strain is obtained by subtracting the elastic strain, which is defined as the value of true stress divided by the Young's modulus, from the total strain, or the following equation:

$$\epsilon^{pl} = \epsilon - \sigma / E \quad (3-15)$$

To convert material test data to the required ABAQUS input, equations 3-13 and 3-14 are used to convert the nominal stress and nominal strain to true stress and true strain. Plastic strain is determined from true stress and true strain using equation 3-15. The converted stress and strains are shown in table 3-2. Although only a slight difference between the nominal and true values exists at small strains, there is a significant difference at larger strains. Therefore, it is important to provide the proper stress-strain data to ABAQUS if large strains occur in the simulation. Figure 3-2 shows the nominal stress versus nominal strain, true stress versus true strain, and true stress versus plastic strain curves.

In fact, the adhesive material data in table 3-2 is obtained by trial calculations using finite element models and compared with experimental results using ASTM D 5656 standard test with a bondline thickness of 0.013". As shown in figure 3-3, the experimental results correlate well with the finite element simulation using the material data in table 3-2.

TABLE 3-2. POSTYIELDING BEHAVIORS OF PTM&W ES6269 ADHESIVE

Nominal Stress σ_{nom}	Nominal Strain ϵ_{nom}	True Stress σ	True Strain ϵ	Plastic Strain ϵ^{pl}
0.0000	0.0000	0.0000	0.0000	
3.2601	0.0122	3.3000	0.0121	0.0000
3.9356	0.0163	4.0000	0.0162	0.0015
4.4172	0.0187	4.5000	0.0185	0.0020
5.0053	0.0231	5.1210	0.0228	0.0040
5.4399	0.0294	5.6000	0.0290	0.0084
5.7416	0.0380	5.9600	0.0373	0.0154
5.9111	0.0456	6.1810	0.0446	0.0219
6.0265	0.0548	6.3570	0.0533	0.0300
6.1121	0.0686	6.5320	0.0664	0.0424
6.1251	0.0799	6.6150	0.0769	0.0526
6.0954	0.1049	6.7350	0.0997	0.0750
5.9845	0.1330	6.7810	0.1249	0.1000
5.7212	0.1913	6.8160	0.1750	0.1500
5.4352	0.2523	6.8070	0.2250	0.2000

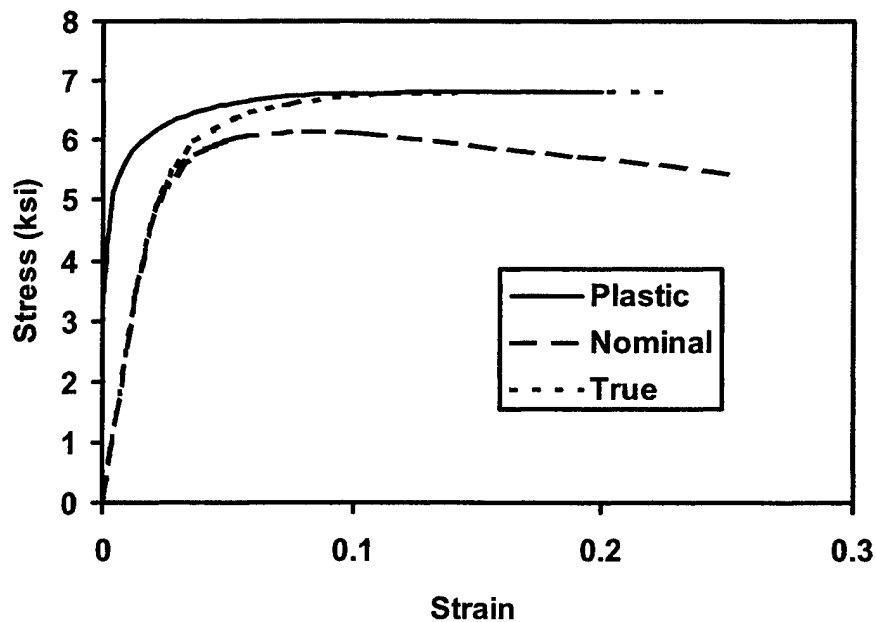


FIGURE 3-2. MATERIAL PROPERTIES OF PTM&W ES6292 PASTE ADHESIVE

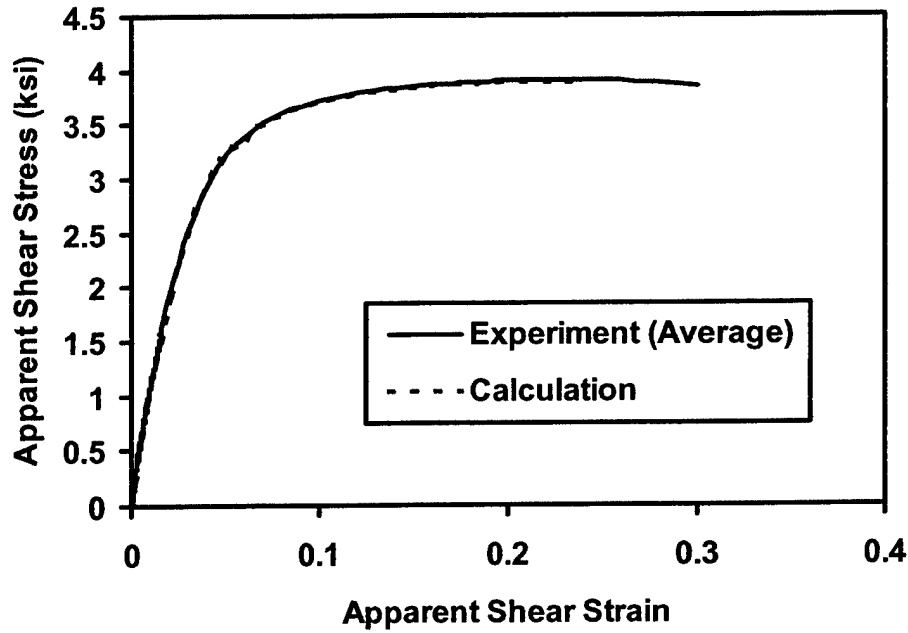


FIGURE 3-3. COMPARISON BETWEEN EXPERIMENTAL RESULTS (ASTM D 5656) AND FE SIMULATION USING MATERIAL PROPERTIES DATA IN TABLE 3-2

3.1.3 Displacement Control at the End of Adherend.

To simulate the actual loading process in the experiment, displacement boundary conditions are used at the loading end of the specimen. The displacement increases linearly along the loading direction at a rate of 0.05 in/min, which is the same as in the experiment.

3.1.4 Half Model.

According to the loading condition and geometry of the specimen, only half of the specimen is modeled with appropriate boundary constraints. As figure 3-4 shows, point O is the geometry center of the specimen and line A-A is perpendicular to the loading direction. Along line A-A, the displacements of two symmetric points B and B' with respect to O must satisfy the following constraints:

$$u_x^B + u_x^{B'} = 0, \quad u_y^B + u_y^{B'} = 0 \quad (3-16)$$

where u_x^B and $u_x^{B'}$ are the displacements along the x direction of points B and B' and u_y^B and $u_y^{B'}$ are the displacements along y direction of points B and B', respectively. The constraint equations are established for all the nodes on line A-A in the finite element model. By implementing these constraint equations into the finite element model together with a zero-displacement boundary condition at point O, only half of the specimen is modeled to reduce the computation time. The right half of the specimen is selected in the present study.

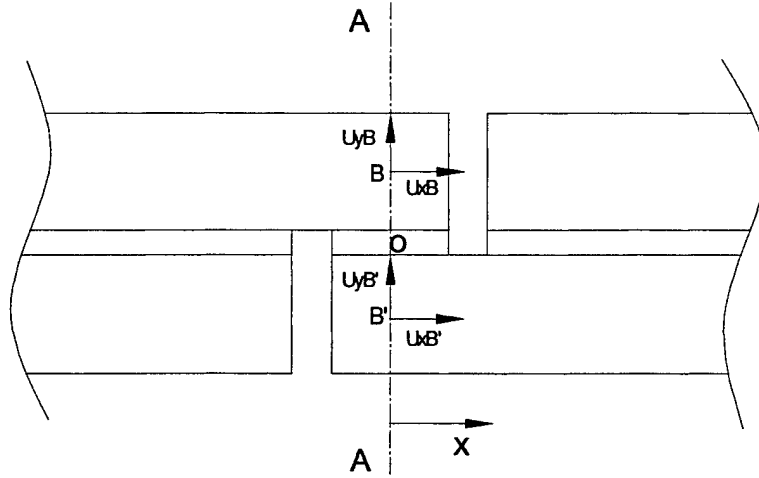


FIGURE 3-4. SYMMETRIC BOUNDARY CONDITIONS AT CENTER OF ASTM D 5656 SPECIMEN

3.1.5 Shear Failure Model.

According to the experiment results, failure of ASTM D 5656 specimen occurs when the adhesive reaches large plastic strains. Therefore, failure models for ductile materials are appropriate to simulate ASTM D 5656 specimen behavior. ABAQUS/Explicit features a shear failure criterion, which is used in the present study to simulate the failure of adhesive (cohesive failure mode). The shear failure model is based on the value of the equivalent plastic strain at element integration points. Failure is assumed to occur when the damage parameter exceeds one. The damage parameter ω is defined as follows:

$$\omega = \sum \left(\frac{\Delta \bar{\epsilon}^{pl}}{\bar{\epsilon}_f^{pl}} \right) \quad (3-17)$$

where $\bar{\epsilon}^{pl}$ is the equivalent plastic strain defined as

$$\bar{\epsilon}^{pl} = \int \sqrt{\frac{2}{3} \sum_{i,j=1,2,3} (\dot{\epsilon}_{ij}^p \dot{\epsilon}_{ij}^p)} dt \quad (3-18)$$

and is designated as PEEQ in ABAQUS/Explicit. The $\dot{\epsilon}_{ij}^p$ is plastic strain rate tensor, $\Delta \bar{\epsilon}^{pl}$ is the increment of PEEQ, and $\bar{\epsilon}_f^{pl}$ is the plastic strain at failure. The summation in equation 3-17 is performed over all increments in the analysis. When the shear failure criterion is reached at an element integration point, all the stress components are set to zero and the material fails at that point. If the material fails at all integration points of an element, the element is removed from the mesh. In the present study, the first-order reduced-integration 2-D solid elements are used. The value of $\bar{\epsilon}_f^{pl}$ is chosen as 0.2 according to trial calculations and experiment results.

3.2 FINITE ELEMENT MODELS OF ASTM D 3165 SPECIMENS.

Two-dimensional finite element models with eight-node elements are used to simulate ASTM D 3165 specimens with bondline thicknesses of 0.013", 0.04", 0.08", and 0.12", as shown in figure 3-5. The number of elements of the entire specimen, the number of elements of the adhesive, and the element aspect ratios are given in table 3-3.

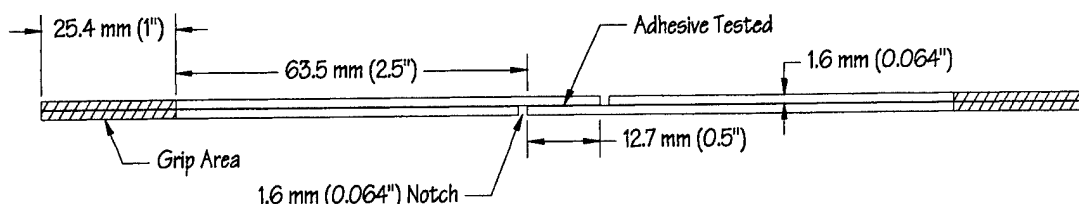


FIGURE 3-5. ASTM D 3165 SPECIMEN GEOMETRY AND DIMENSIONS

TABLE 3-3. NUMBER OF ELEMENTS AND ASPECT RATIO OF FINITE ELEMENT MODELS (ASTM D 3165)

FE Model	Adhesive Thickness (in)	Number of Elements of Entire Model	Number of Elements of Adhesive	Number of Elements Through Adhesive Thickness	Largest Element Aspect Ratio of Adhesive
D 3165_1	0.013	6,020	580	8	5.1
D 3165_2	0.040	4,284	860	14	3.5
D 3165_3	0.080	3,872	920	18	2.8
D 3165_4	0.120	3,944	1,120	22	2.5

Only half of the ASTM D 3165 specimen is modeled due to the symmetry of both loading and specimen geometry (as presented previously for the finite element models of ASTM D 5656 specimens). Displacement control is applied at the loading end of model. The material properties of both the adherend and adhesive are the same as those used for ASTM D 5656 specimens. The geometric and material nonlinearities are also included and the nonlinear equilibrium equations are solved with Newton's method in ABAQUS/Standard. The automatic increment scheme is used because the increment is based upon computational efficiency.

Static analysis is used for two reasons: (1) the nonlinearity of the material and the deformation in the adhesive of ASTM D 3165 specimens are not as severe as those of ASTM D 5656 at failure and (2) methods of fracture mechanics, such as the *J*-integral criterion, critical crack opening displacement criterion, can be applied with static analysis.

The techniques of fracture mechanics analysis associated with the finite element model are described as follows.

3.2.1 *J*-Integral.

The *J*-integral is applied in quasi-static fracture analysis in ABAQUS/Standard to characterize the energy release rate associated with crack growth. Considering an arbitrary counter-clockwise path (Γ) around the tip of a crack, as illustrated in figure 3-6, the *J*-integral is as follows:

$$J = \int \left(w dy - \sum_{i=1}^3 T_i \frac{\partial u_i}{\partial x} ds \right) \quad (3-19)$$

where w is the strain energy density; u_1 , u_2 , and u_3 are the displacement vector components; ds is the length increment along the contour Γ ; and T_1 , T_2 , and T_3 are components of the traction vector. The traction is a stress vector normal to the contour. In other words, T_1 , T_2 , and T_3 are the normal stresses acting at the boundary if a free-body diagram on the material inside of the contour is constructed. Theoretically, the values of *J*-integral should be independent of the path selected. However, the calculated *J*-integral based on different rings may vary because of the approximate nature of finite element solutions. Therefore, at least two contours are used for *J*-integral calculation according to the ABAQUS/Standard User's Manual. Based on the convergence test, the *J*-integral on the fourth ring of elements around the crack front shows appropriate stability.

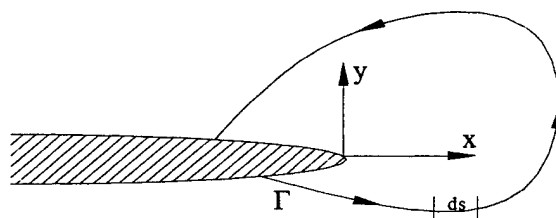


FIGURE 3-6. ARBITRARY CONTOUR AROUND TIP OF A CRACK

3.2.2 Modeling the Crack Tip Singularity.

Because the failure mode of the aluminum-adherend ASTM D 3165 specimen is considered to be the fracture between the adherend and adhesive, i.e., the adhesive failure mode, a precrack must be built into the finite element model. The *J*-integral calculated on the fourth ring is used as the index for judging the onset of the crack. To improve the accuracy of the *J*-integral and the stress and strain calculations, the singularity at the crack tip is modeled as suggested in ABAQUS/Standard Manual. Eight-node isoparametric elements must be used and one side of the element is collapsed so that all three nodes a, b, and c have the same geometric location (on the crack tip) to fulfill the mesh singularity requirement, as depicted in figure 3-7. During this collapsing process, the middle node remains in the middle and nodes a, b, and c are allowed to move independently. In this case, the $1/r$ (r is the distance from the crack tip) singularity in strain is created, which is accurate enough for *J*-integral calculation in the present study according to trial calculations. The typical mesh with the precrack is shown in figure 3-8. The length of the precrack is approximately 3% of the length of the overlap for all models.

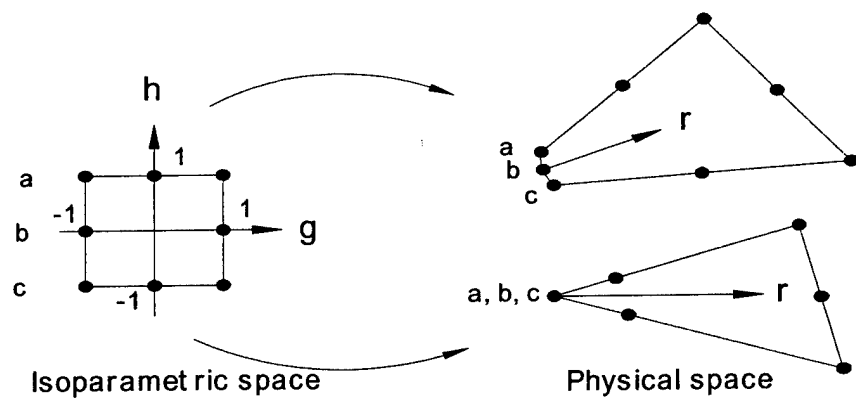


FIGURE 3-7. COLLAPSED TWO-DIMENSIONAL ELEMENT

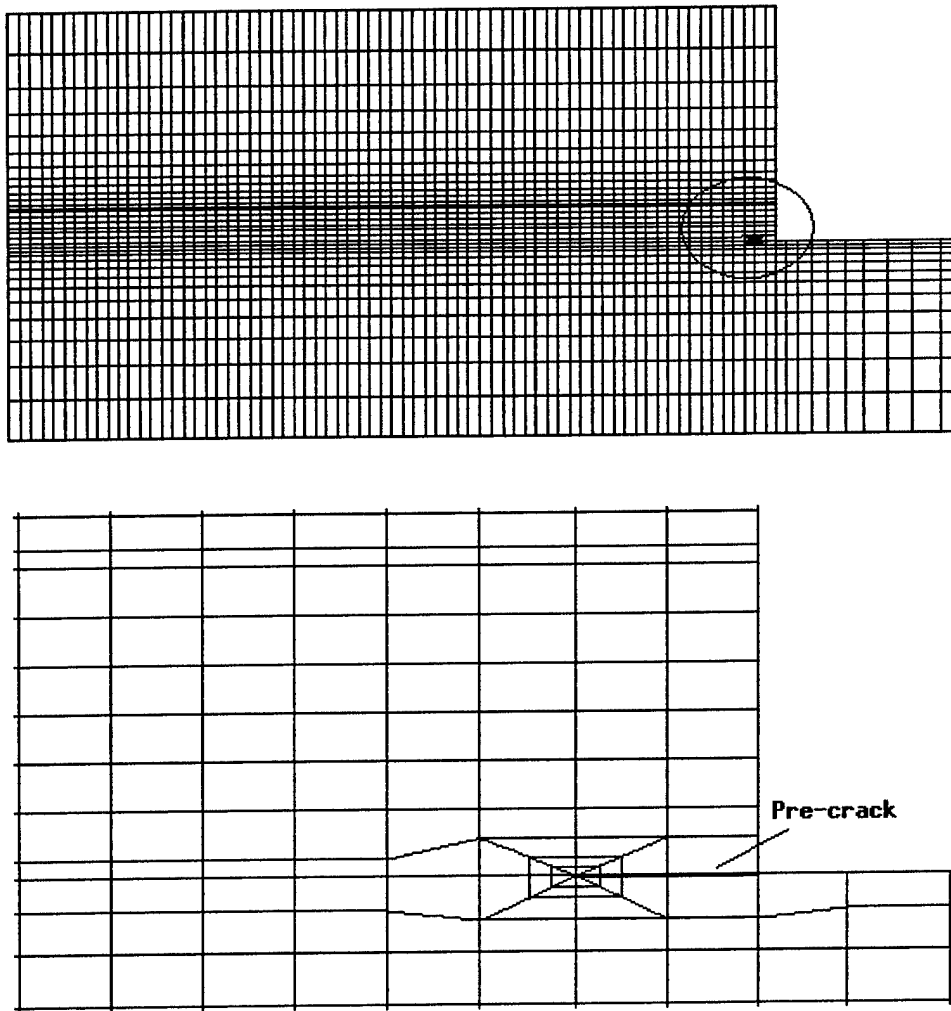


FIGURE 3-8. TYPICAL FOCUSED MESH FOR FRACTURE MECHANICS EVALUATION

3.3 RESULTS AND DISCUSSION OF ASTM D 5656 SPECIMENS.

It is difficult to gain more detailed information from the actual ASTM D 5656 experiment other than the apparent shear stress-strain curves and apparent shear strength. The failure mode is estimated by examining the failed specimen, which does not reflect what actually occurs during the test. However, by using the finite element method, the mechanical behavior of ASTM D 5656 specimens during the loading process can be simulated. The results from finite element simulation can provide more detailed information regarding deformation, stress and strain distributions, damage process, and damage mode of the specimen. This information is important for understanding the damage mechanism of such joints and in realizing the load carrying capability, which provides practical guidance in joint design.

3.3.1 Deformation Analysis (ASTM D 5656).

Detailed deformation analysis in the overlap area of the specimen is very important. It is the first step towards understanding the mechanical behavior of the joint during loading. For ASTM D 5656 specimens with different bondline thickness, figures 3-9 through 3-12 show the calculated displacements, without applying any failure criterion, along the top and bottom adhesive/adherend interfaces under each respective experimental failure load. In these figures, u_x and u_y are the displacements along the load direction and the direction perpendicular to the load direction, respectively, as shown in figure 3-4. It can be seen that the displacements are linear with respect to x , for all four bondline thicknesses. The angles of rotation of the adherends in the overlap region for different bondline thicknesses under the respective failure load are listed in table 3-4. The small angles indicate that bending does not contribute much to the adherend deformation within the overlap due to the large adherend thickness.

TABLE 3-4. ANGLE OF ROTATION OF OVERLAP AREA OF
ASTM D 5656 SPECIMENS AT FAILURE LOAD

Bondline Thickness, t , (in)	Experimental Apparent Adhesive Shear Strain at Failure	Experimental Failure Load (kip)	Rotation Angle of Overlap at Failure (FE Model)
0.013	0.30	1.41	0.152E
0.040	0.20	1.34	0.182E
0.080	0.12	1.26	0.208E
0.120	0.065	1.05	0.212E

Figures 3-13 and 3-14 show the through-thickness average adhesive shear and peel strain distributions along the overlap for specimens with different bondline thicknesses when each respective experimental failure load is applied to the finite element model. The through-thickness average adhesive shear strain in figure 3-13 is calculated by dividing the difference in displacement in the x direction between the upper and lower adhesive/adherend interfaces by the bondline thickness. Similarly, the through-thickness average adhesive peel strain is calculated by dividing the difference of displacements in the transverse direction (y direction). It can be seen from figure 3-13 that the through-thickness average shear strain is fairly uniform within the overlap and that larger average adhesive shear strains exist, at failure, in joints with thinner

bondlines. Figure 3-14 indicates that the through-thickness average adhesive peel strain does vary along the overlap length for specimens with a thinner bondline, especially at the end of the overlap. However, the through-thickness average peel strain is small compared to the through-thickness average shear strain. It should be noted that these through-thickness average adhesive strains cannot fully determine the actual stress distributions because both the free-surface boundary conditions and stress concentration at the edges of the overlap have great effects on the adhesive stress distributions.

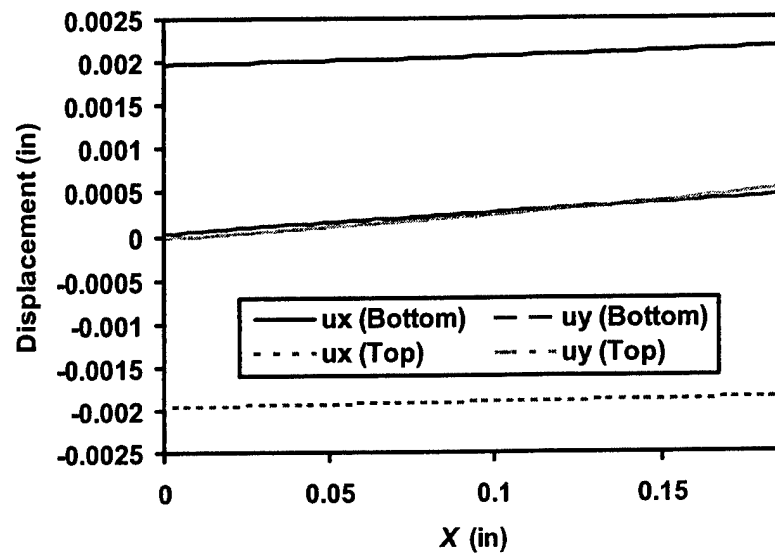


FIGURE 3-9. DISPLACEMENT OF ASTM D 5656 SPECIMEN WITH BONDLINE THICKNESS OF 0.013" AT FAILURE LOAD (1.41 kips)

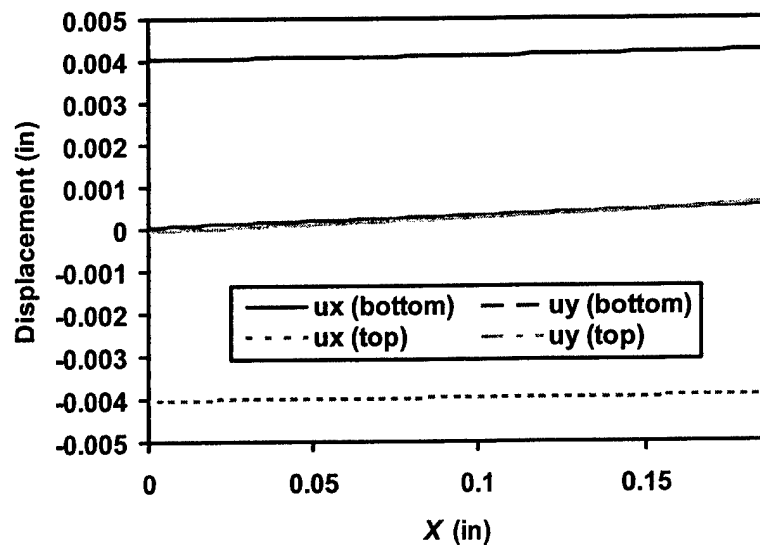


FIGURE 3-10. DISPLACEMENT OF ASTM D 5656 SPECIMEN WITH BONDLINE THICKNESS OF 0.040" AT FAILURE LOAD (1.34 kips)

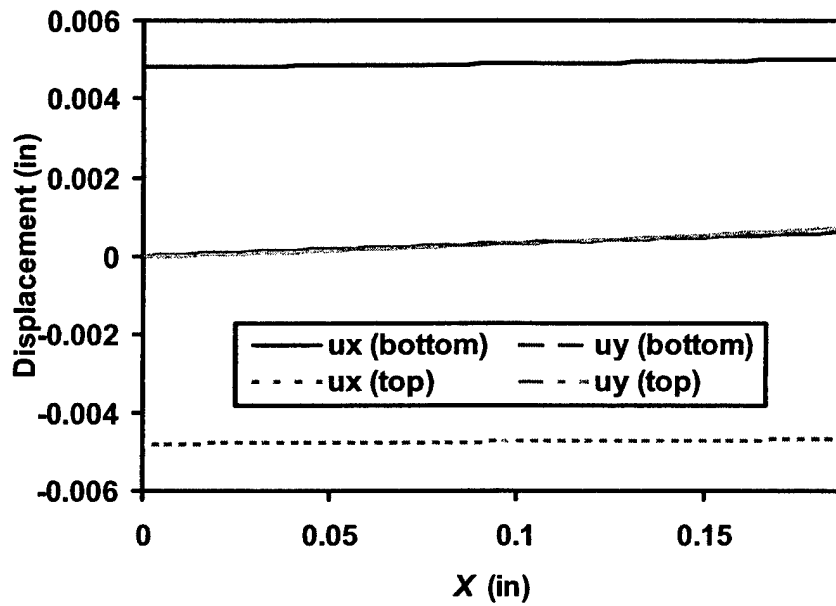


FIGURE 3-11. DISPLACEMENT OF ASTM D 5656 SPECIMEN WITH BONDLINE THICKNESS OF 0.080" AT FAILURE LOAD (1.26 kips)

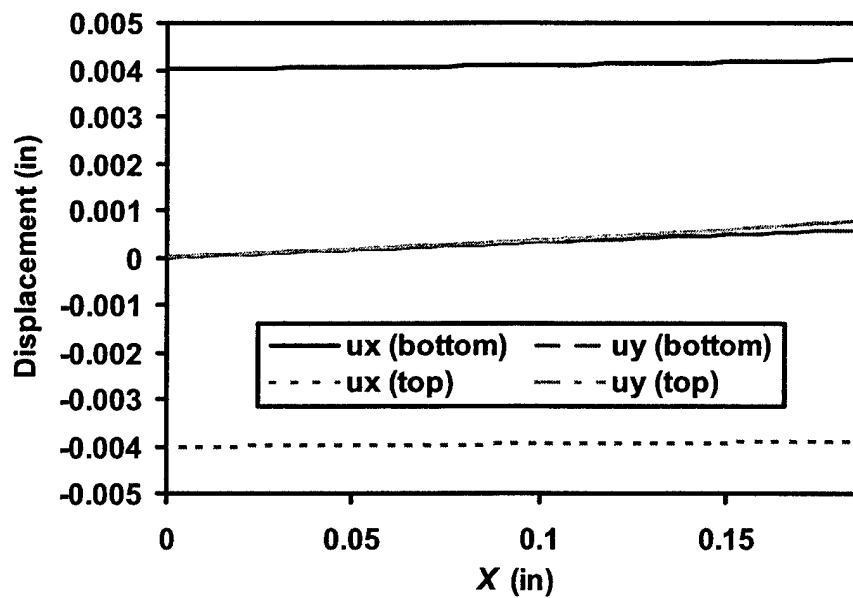


FIGURE 3-12. DISPLACEMENT OF ASTM D 5656 SPECIMEN WITH BONDLINE THICKNESS OF 0.120" AT FAILURE LOAD (1.05 kips)

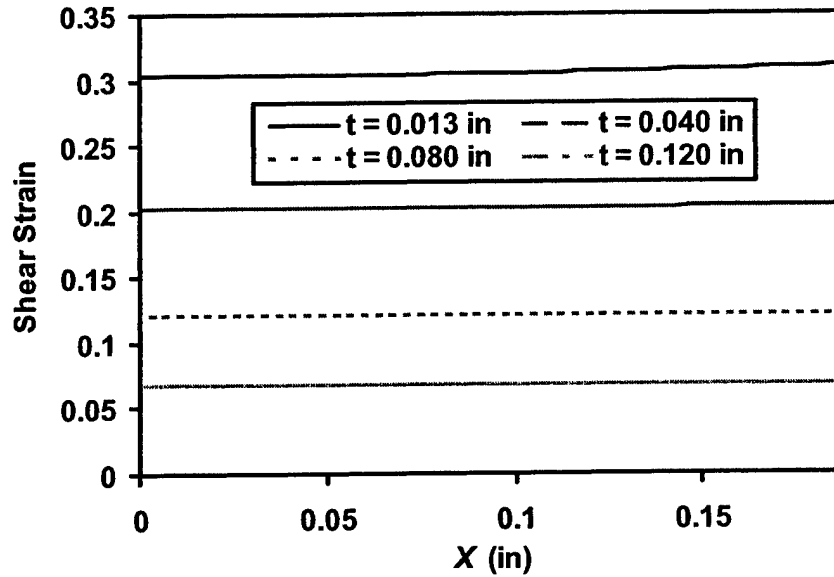


FIGURE 3-13. THROUGH-THICKNESS AVERAGE ADHESIVE SHEAR STRAIN WITHIN OVERLAP AT EACH RESPECTIVE FAILURE LOAD (ASTM D 5656)

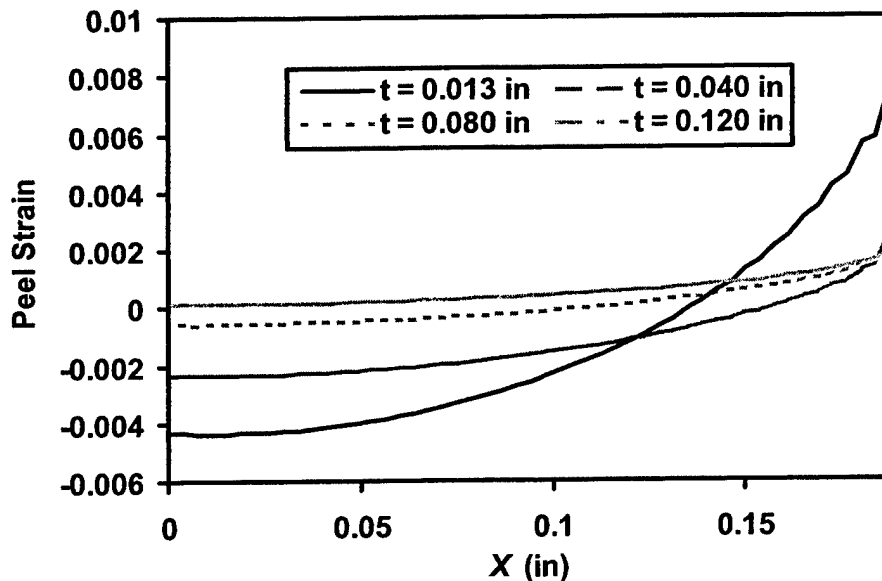


FIGURE 3-14. THROUGH-THICKNESS AVERAGE ADHESIVE PEEL STRAIN WITHIN OVERLAP AT EACH RESPECTIVE FAILURE LOAD (ASTM D 5656)

3.3.2 Stress Analysis (ASTM D 5656).

The adhesive stress distributions are quite complex in the ASTM D 5656 specimen. Generally speaking, shear is the main mechanism which transfers load from one adherend to the other. However, due to the load eccentricity of the adherends, both the adhesive shear stress and peel stress exist at the ends of the overlap and play an important role in failure assessment.

Theoretically, the adhesive stresses in the ASTM D 5656 specimen can be fully determined by the displacement boundary conditions at the upper and lower adhesive/adherend interfaces and the two free adhesive surfaces at the ends of the overlap. Because the tensile rigidity (EA value) of the adherends is relatively high, the displacement along the load direction at the two adhesive/adherend interfaces is rather uniform. Therefore, the main factor which creates the complexity of the adhesive stresses is the free adhesive surfaces at the ends of the overlap.

Figure 3-15 shows five paths that are along the load direction and evenly distributed through the bondline thickness. The adhesive shear stress distribution under a tensile load of 800 lb for the five paths is shown in figures 3-16 through 3-19. It can be seen that the adhesive shear strain decreases to zero at the free adhesive surface (Paths 2, 3, and 4 at $x = 0.1875$). The portion of the overlap where the adhesive shear stress deviates from the near-constant value is obviously larger when the adhesive free surface at the ends of the overlap is larger, i.e., in the case of thicker bondlines. The adhesive free surface actually causes this nonuniformity of the shear stress distribution. Figure 3-20 shows the five-path average adhesive shear stress distribution based on the four-bondline thicknesses. Similarly, thicker bondlines, or larger adhesive free surfaces at the ends of the overlap, affect a larger portion of the overlap. As a result, under the same applied load, in order to compensate for the larger affected overlap area by the free surface, the adhesive shear stress in the middle portion is higher for specimens with larger bondline thicknesses. In the actual ASTM D 5656 tests, the apparent adhesive shear stress is calculated by dividing the applied load by the overlap area. The larger adhesive shear stress at the middle overlap portion in the finite element model is reflected as larger adhesive shear strain in the actual ASTM D 5656 tests. Therefore, the higher adhesive shear strain in the middle portion of the overlap for the thicker bondline explains the fact that thicker bondlines result in lower adhesive shear moduli when the ASTM D 5656 test is conducted. Table 3-5 shows the finite element model simulated ASTM D 5656 test results. It is obvious that lower adhesive shear moduli are calculated for larger bondline thicknesses.

It should be noted that if the bondline becomes very thin (thinner than 0.01" for adhesives with G_i 100 ksi, [27]) the shear modulus obtained from ASTM D 5656 tests is actually larger than the true value. This is because the effect of nonuniformity of the adherend deformation is no longer negligible when the adhesive is very thin. Actually, the shear stress distribution in figure 3-20 has already shown this trend where the five-path average adhesive shear stress distribution starts peaking up at the edge of the overlap for the case of 0.013" bondline thickness.

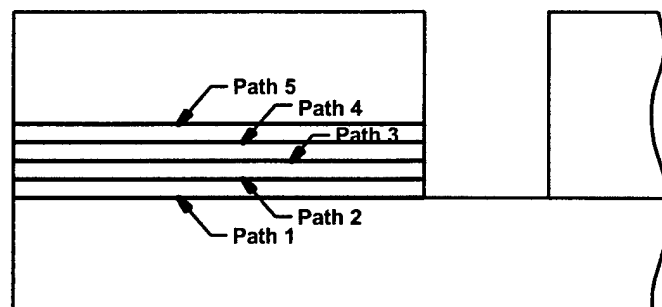


FIGURE 3-15. DEFINITION OF FIVE PATHS IN ADHESIVE LAYER

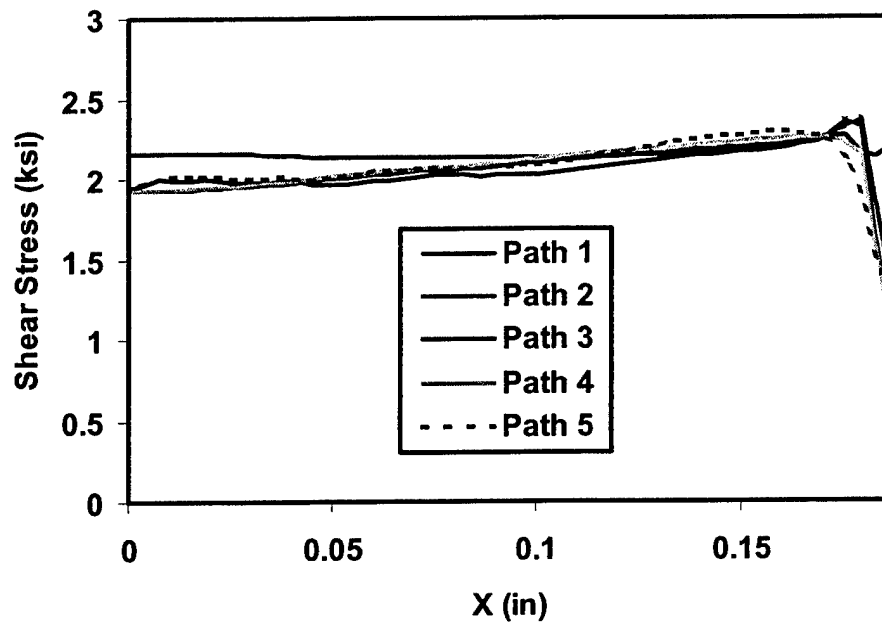


FIGURE 3-16. ADHESIVE SHEAR STRESS DISTRIBUTION (0.013" BONDLINE THICKNESS, ASTM D 5656)

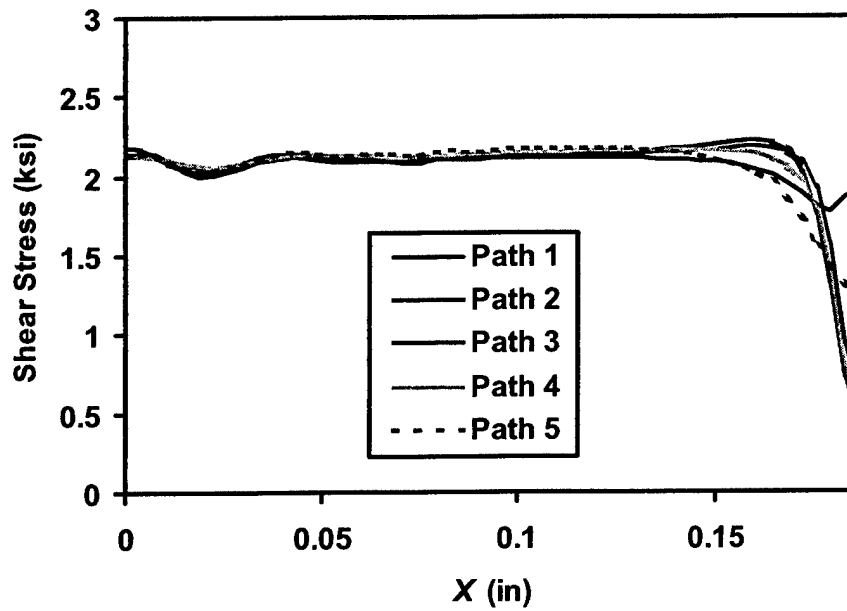


FIGURE 3-17. ADHESIVE SHEAR STRESS DISTRIBUTION (0.04" BONDLINE THICKNESS, ASTM D 5656)

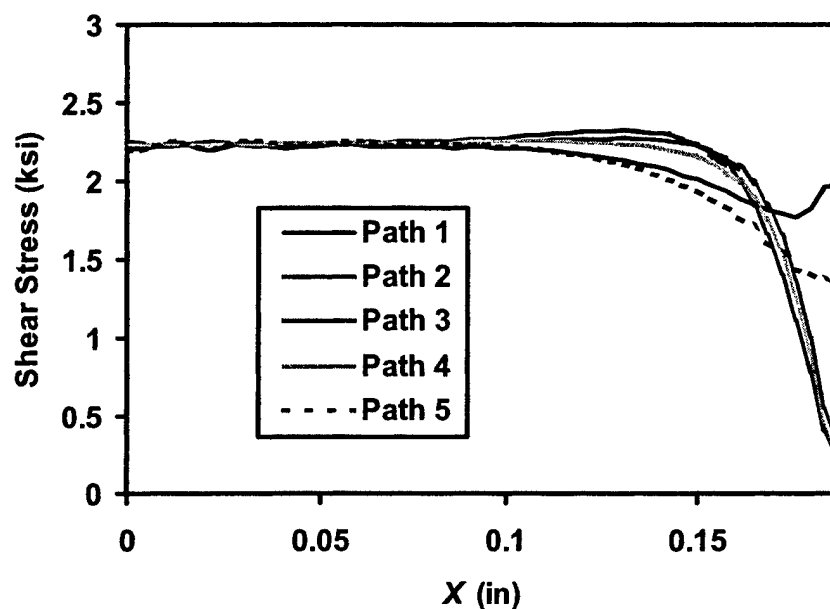


FIGURE 3-18. ADHESIVE SHEAR STRESS DISTRIBUTION (0.08" BONDLINE THICKNESS, ASTM D 5656)

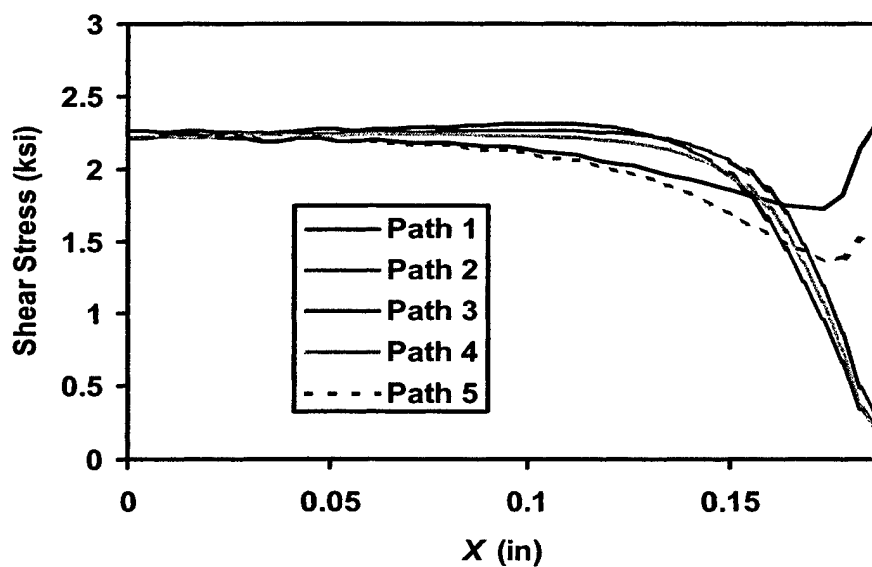


FIGURE 3-19. ADHESIVE SHEAR STRESS DISTRIBUTION (0.12" BONDLINE THICKNESS, ASTM D 5656)

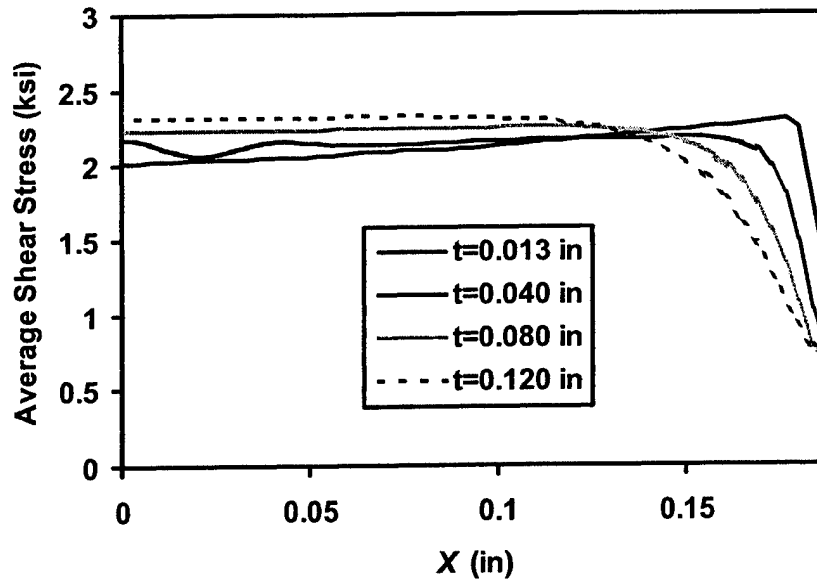


FIGURE 3-20. FIVE-PATH AVERAGE ADHESIVE SHEAR STRESS DISTRIBUTION (ASTM D 5656)

TABLE 3-5. ADHESIVE SHEAR MODULUS

Bondline Thickness (in)	0.013	0.04	0.08	0.12
Apparent Shear Modulus, G_{ASTM} (ksi), Finite Element Simulated	99.28	94.73	89.99	86.02
Deviation*	-6.1%	-10.4%	-14.9%	-18.7%

Note: $Deviation = \frac{G_{ASTM} - G_{input}}{G_{input}}$

Where G_{ASTM} is the calculated adhesive shear modulus using finite element models to simulate the actual ASTM D 5656 test and $G_{input}=105.77$ ksi is the material property used in the finite element model.

Figure 3-21 shows the development of shear stress distribution along path 3 (as defined in figure 3-15), while the displacement at the end of the joint gradually increases (as shown in figure 3-22). When the load nearly reaches the failure load of the joint, the adhesive has already entered its plastic state. After the adhesive plastic strain has initiated, both the load and the adhesive stress rise more slowly even though the joint-end displacement remains at the same speed.

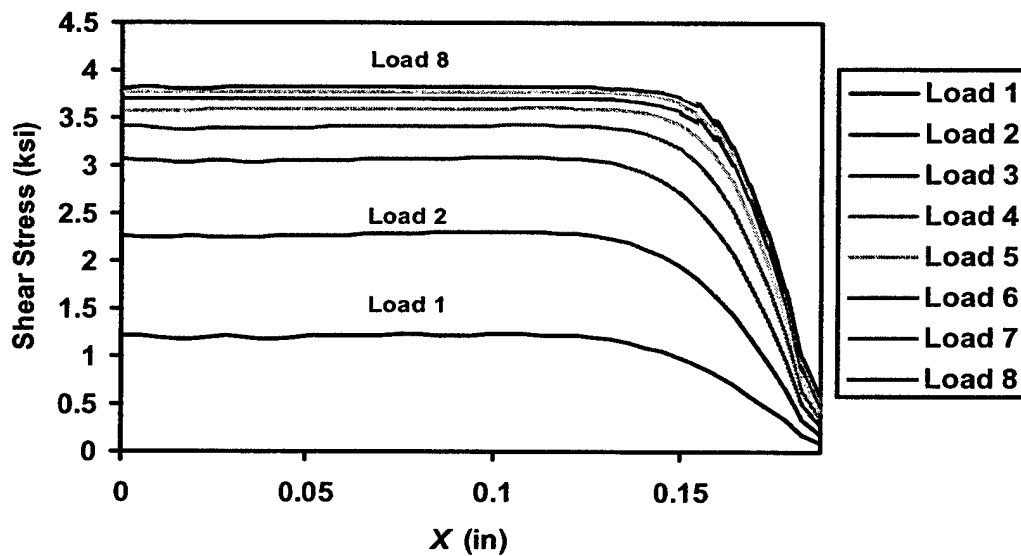


FIGURE 3-21. DEVELOPMENT OF SHEAR STRESS DISTRIBUTION ALONG PATH 3 (0.12" BONDLINE THICKNESS, ASTM D 5656)

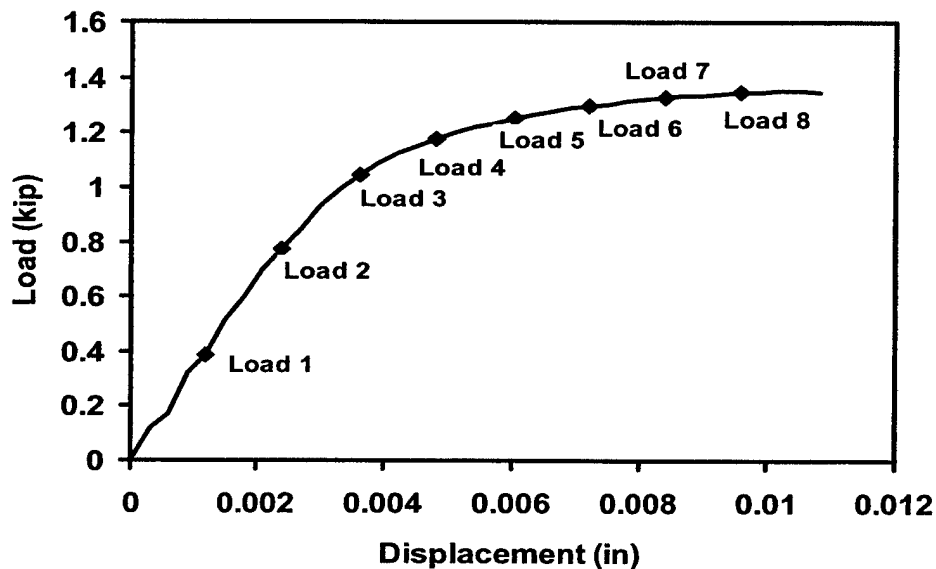


FIGURE 3-22. LOAD VERSUS JOINT-END DISPLACEMENT (0.12" BONDLINE THICKNESS, ASTM D 5656)

3.3.3 Failure Mode and Failure Criterion (ASTM D 5656).

As stated in the ASTM D 5656 test standard, the purpose of this test is to determine the stress-strain relationship of the adhesive. However, understanding the failure mode and failure criterion can assist in design and analysis of such joints.

The three major failure modes of adhesive-bonded joints are as follows: (1) cohesive failure, (2) adhesive failure, and (3) adherend failure. Because ASTM D 5656 specimens use aluminum adherends, their failure tends to be cohesive and/or adhesive failures. Cohesive failure is characterized by the failure of the adhesive itself. In the case of cohesive failure, the adhesive is left on both bonded surfaces of the adherends. However, sometimes it is difficult to judge cohesive failure for a specimen because of the random propagation of the failure surface inside the adhesive. The failure surface might develop inside the adhesive, propagate into the adhesive/adherend interface, and continue to develop along the interface. It is also worthwhile to note that even though cohesive failure is the failure mode of the specimens, the apparent strength of the joint, which is obtained by dividing the failure load by the adhesive area (overlap area), cannot be regarded as merely material dependent. Their values are closely related to the configuration of the joint as well.

Figure 3-23 shows ASTM D 5656 test results using four different bondline thicknesses. The load/apparent adhesive shear strain curves for different bondline thicknesses (t) all have a ramp section and a descending or near-horizontal section. In the ramp section, the apparent shear modulus deviates from one bondline thickness to another, as described previously. After yielding, the apparent shear strain at failure is several times larger for the case of a thin bondline than for the case of a thick bondline. This means that when the joint fails, there would be a much larger plastic strain accumulated inside the adhesive layer of thinner bondlines. The observation that all the curves are fairly smooth, even at the turning sections, implies that the damage developing process inside the adhesive is stable. No staggered impetuous damage occurs during the loading process. Therefore, it is reasonable to assume that the failure is caused by the accumulation of plastic strain in the adhesive.

Based on this assumption, the Shear Failure Criterion featured in ABAQUS/Explicit, as described in “3.1 (5) Shear Failure Model,” is applied to investigate the failure load of ASTM D 5656 specimens. To further demonstrate the dominating factors of joint failure, peel stress, shear stress, and PEEQ (equivalent plastic strain) at two critical locations within the adhesive layer are analyzed for specimens with different bondline thicknesses. Figure 3-24 shows the critical locations where stress concentration occurs during the loading process. Location 1 is at the corner of the adhesive layer, which is the first adhesive element along the lower bondline at the free-boundary surface. Location 2 is where the actual failure is initiated in the finite element model with a bondline thickness of 0.013”. It is located at the upper interface between the adhesive and adherend and is about 15% of the overlap length away from the free boundary of the adhesive.

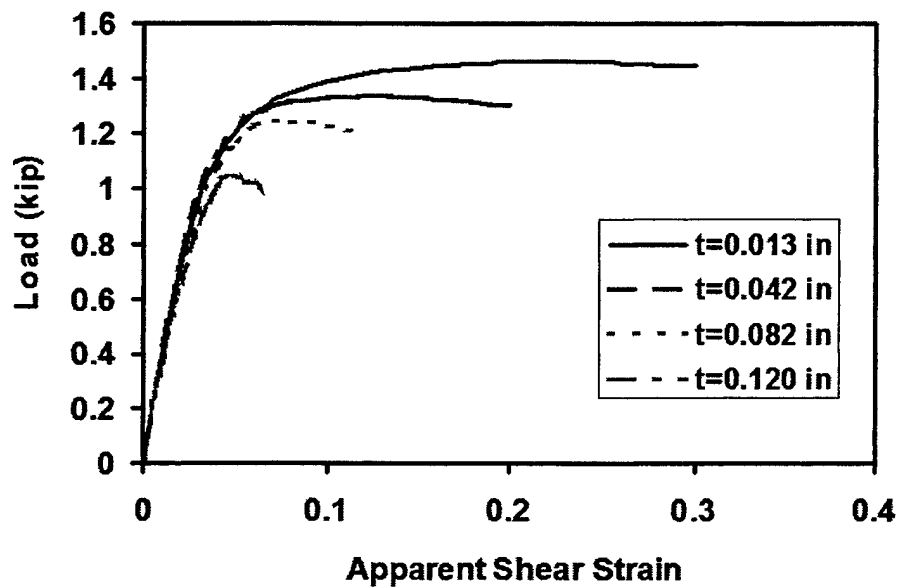


FIGURE 3-23. EXPERIMENTAL LOAD VERSUS APPARENT ADHESIVE SHEAR STRAIN CURVES (ASTM D 5656)

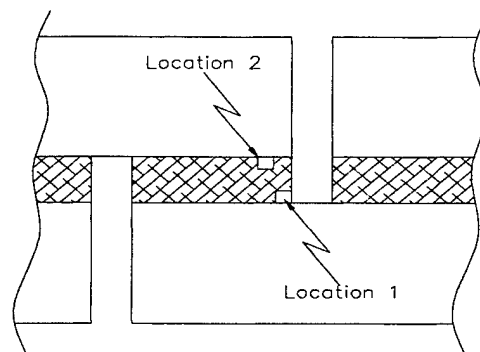


FIGURE 3-24. CRITICAL LOCATIONS INSIDE ADHESIVE LAYER

Figures 3-25 to 3-27 show the shear stress, peel stress, and PEEQ development at the two critical locations, respectively. Figures 3-25 and 3-26 show that it is impossible to find some critical stresses as an index of failure, because the adhesive materials at the critical locations are in large plastic states in which the stress has almost no change. The stress criteria cannot reflect the actual damage state in this case. Different from stresses, PEEQ always increases during loading until the critical value of 0.2, as shown in figure 3-27. The critical value of 0.2 is carefully chosen by trial computation in order to correlate the failure loads and the corresponding apparent shear strains at failure of all specimens in the experiments. Note that the initial damage location of the specimen with bondline thickness of 0.013" is different from other specimens. As shown in figure 3-27, its PEEQ increases faster at location 1 than location 2 initially, but the PEEQ at

location 2 grows much faster and finally exceeds the PEEQ at location 1 before reaching the critical value. Finally, the initial damage occurs at location 2.

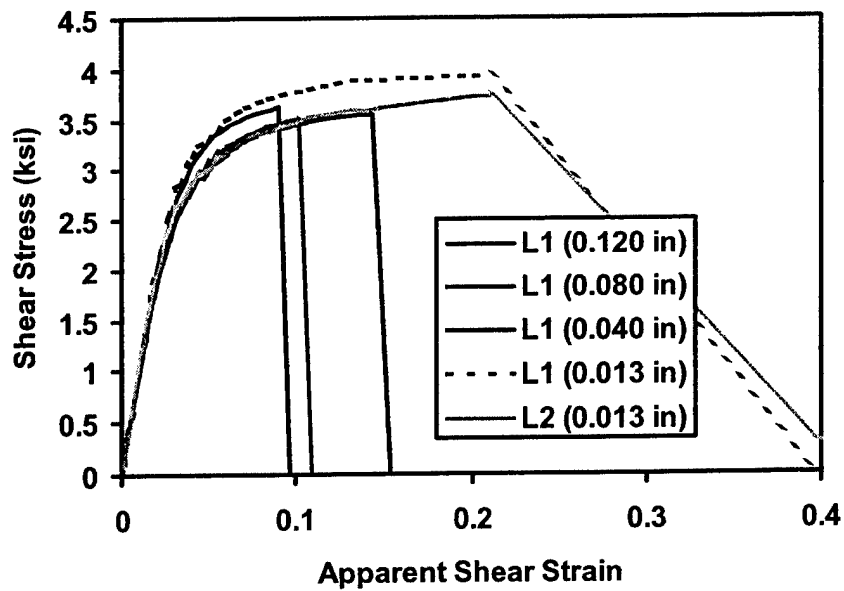


FIGURE 3-25. SHEAR STRESS AT CRITICAL LOCATIONS

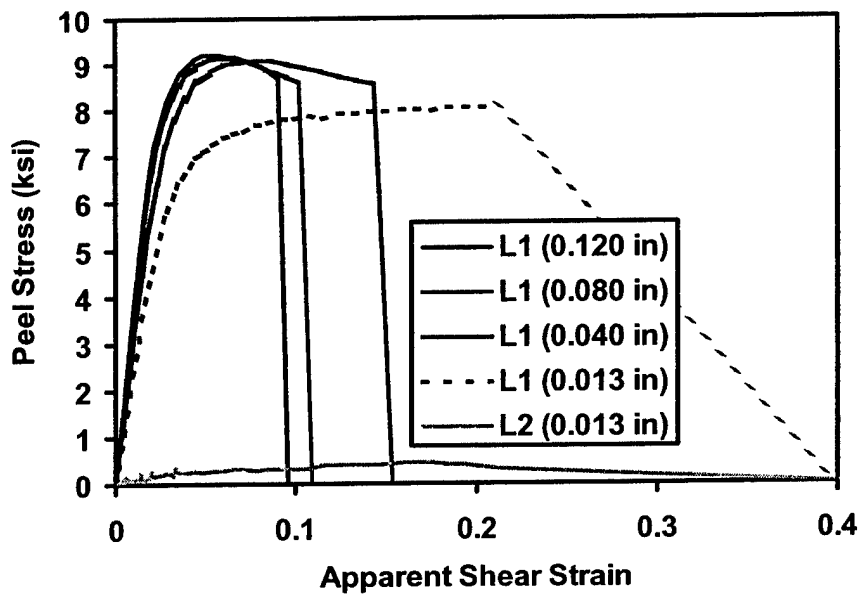


FIGURE 3-26. PEEL STRESS AT CRITICAL LOCATIONS

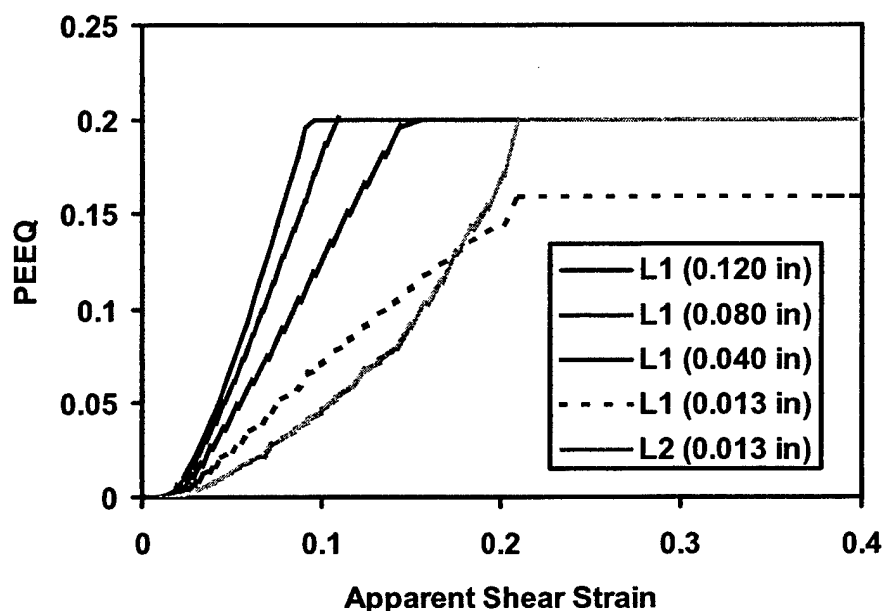


FIGURE 3-27. PEEQ AT CRITICAL LOCATIONS

Figure 3-28 shows the calculated apparent shear stress-strain curves with the equivalent plastic shear strain as failure criterion. The curves for thin bondlines correlate well with the experimental results shown in figure 3-29. The main deviation is that the failure loads and the corresponding apparent shear strains at failure of thick bondline (0.08" and 0.12") from the finite element models are higher than those from the experiments. The reason might be that the localized effects due to the free boundary are more severe in the adhesive of the specimens with thicker bondlines. The PEEQ at the critical locations accumulates quickly in the loading process while damage initiates in the elements at the critical locations after PEEQ reaches the critical value. However, damage does not develop as quickly among the elements near the damaged areas compared to what actually occurred in experiments. This is because damage initiation and damage development in the finite element models should be judged with different criteria or, at least, the same criterion with different parameters. Usually, the criterion for damage propagation is lower than the criterion for damage initiation. In the present study, only the shear failure criterion with a constant parameter is used for judging the entire damage process, which includes damage initiation and development. Damage in the specimens with thin bondlines show that plastic strain develops more evenly in the adhesive. Once the elements at the critical location become critical, the neighboring elements of the damaged elements reach the critical value almost simultaneously. Therefore, the calculation results seem more accurate for the specimens with thin bondlines.

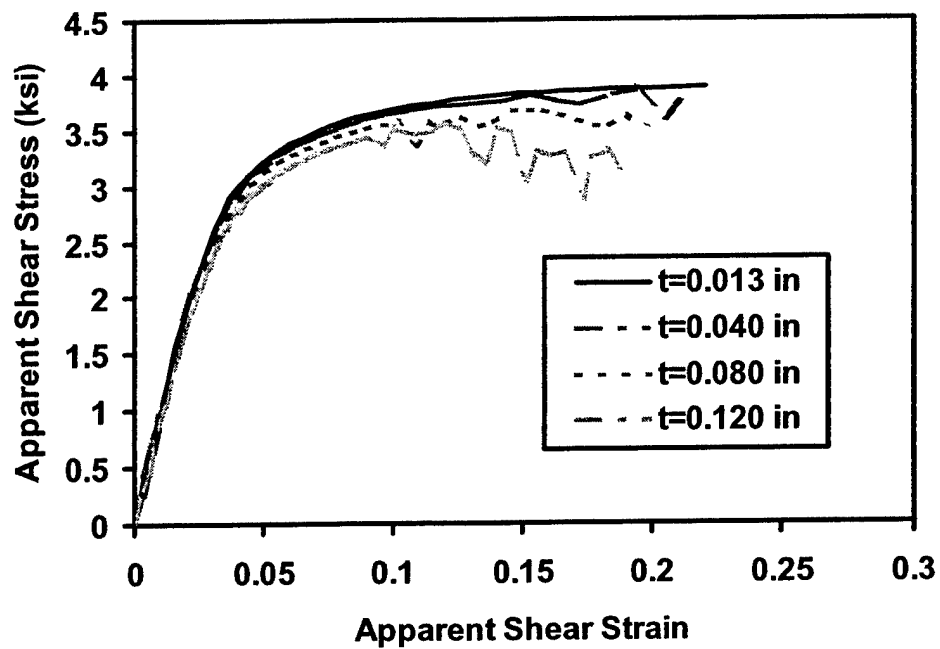


FIGURE 3-28. CALCULATED APPARENT SHEAR STRESS-STRAIN CURVES FOR ASTM D 5656 SPECIMENS

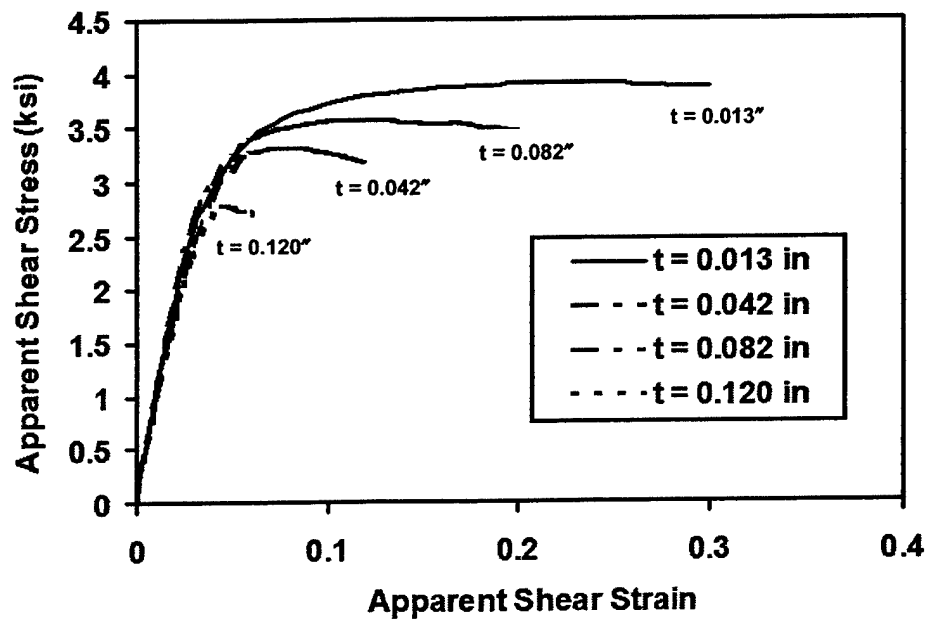
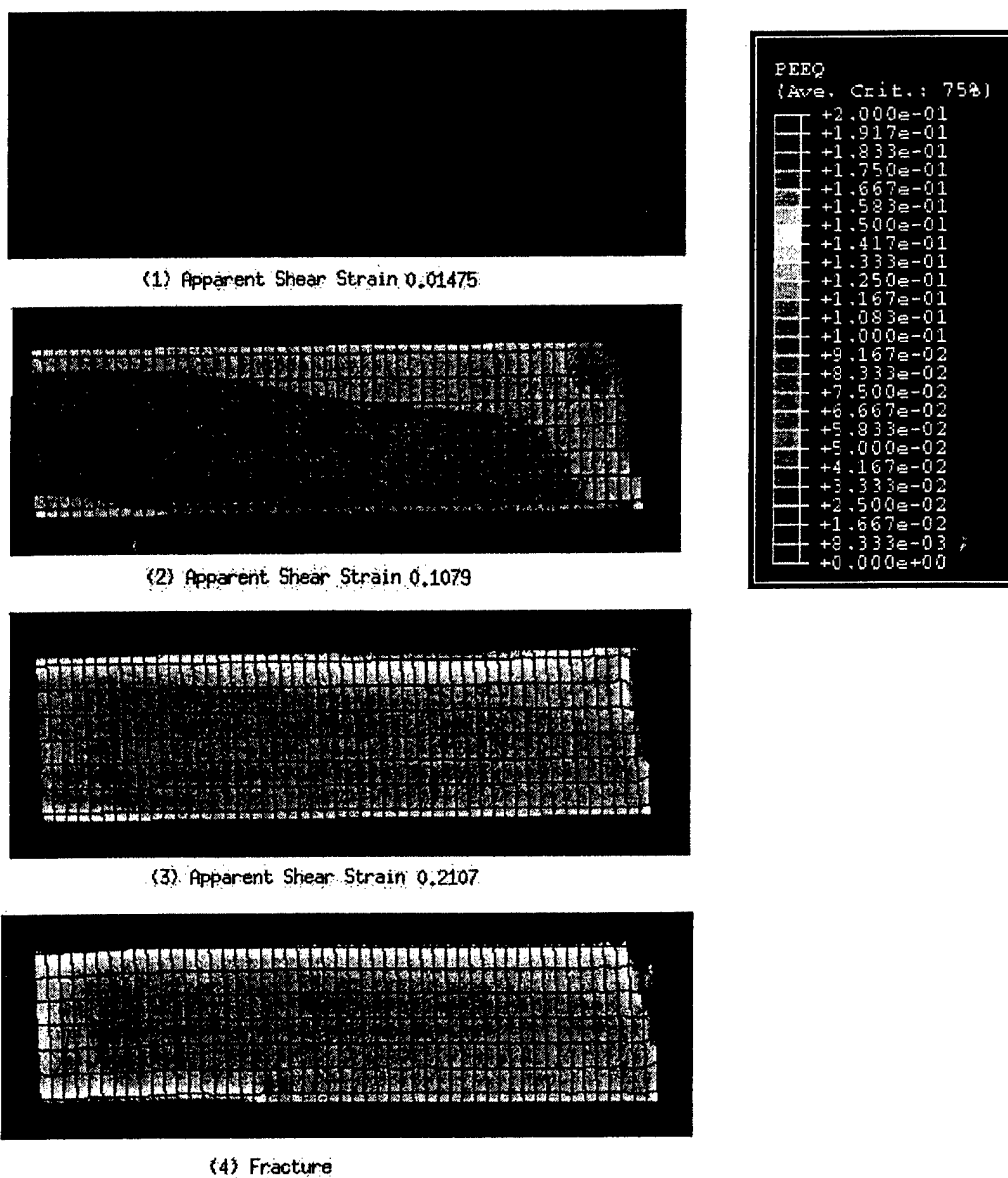


FIGURE 3-29. EXPERIMENTAL APPARENT SHEAR STRESS-STRAIN CURVES FOR ASTM D 5656 SPECIMENS

Figures 3-30 to 3-33 show the process of PEEQ development inside the adhesive with four different bondline thicknesses, 0.013", 0.04", 0.08", and 0.12", respectively. Each picture describes the PEEQ distribution at four stages. The first stage represents the first appearance of the plastic state inside the adhesive layer (the element with little lighter color at the lower right corner). The second stage, shown in figures 3-31 through 3-33, is the moment of the first appearance of damaged elements, i.e., PEEQ reaches 0.2 for this element at that time. Because there is no element damage occurring before the final fracture for the specimen with a bondline thickness of 0.013", the second stage, in figure 3-30, gives the distribution of PEEQ at the moment that the entire adhesive reaches plastic state. The other two stages represent the moments right before and after the final fracture, respectively.

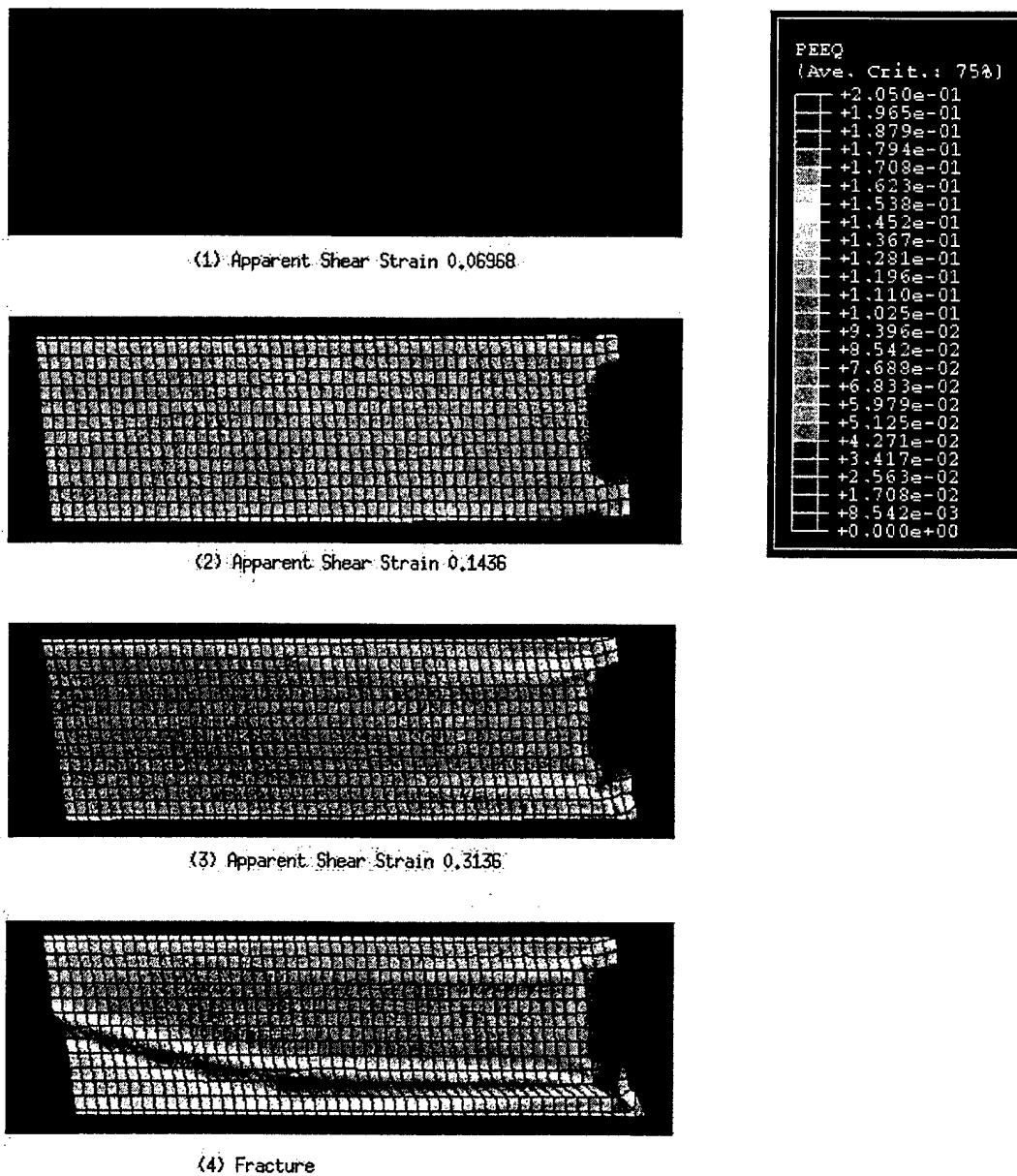
From these figures, it can be seen that the element at location 1 is the first to reach a plastic state during the loading process, indicating that location 1 has the most serious stress concentration. Thereafter, plastic deformation gradually develops from location 1 and also from the upper right corner in the adhesive. For the specimens with bondline thicknesses of 0.12", 0.08", and 0.04", PEEQ develops more quickly at location 1 and results in final fracture inside the adhesive. For the specimen with the 0.013" thick bondline, PEEQ develops quickly at location 1 at the beginning and then slows down. Meanwhile, PEEQ at location 2 begins to increase much faster and finally leads to the initiation of damage. These pictures also show that the damage developments after the initiation of damage take place more rapidly in the adhesive with thin bondlines than in those with thick bondlines. As shown in figure 3-30, the final fracture for the specimen with the 0.013" bondline thickness occurs almost instantly after PEEQ at location 2 reaches the critical value. For other specimens with thicker bondlines, the damage gradually develops from the initiation of damage to the final fracture of the whole model, which can be seen from the development of apparent shear strain between stages 2 and 3 in figures 3-31 through 3-33.

As shown in figure 3-29, the failure of joints with thick bondlines (0.082" and 0.120") occurs before the development of large plastic deformation. Therefore, the J -integral might be a more suitable failure criterion than the PEEQ criterion for the cases of thick bondlines. To obtain more accurate predictions of failure loads for specimens with thick bondlines, the J -integral failure criterion is used as an alternative. The experimental results are shown in figure 3-29, and the load versus J -integral curves from the finite element model are shown in figure 3-34. Table 3-6 lists the experimental and predicted joint failure loads where the critical J -integral value (J_c) is taken as 4 psi-in. It can be seen that the J -integral criterion is also a good prediction for the failure of the ASTM D 5656 joint with thicker bondlines.



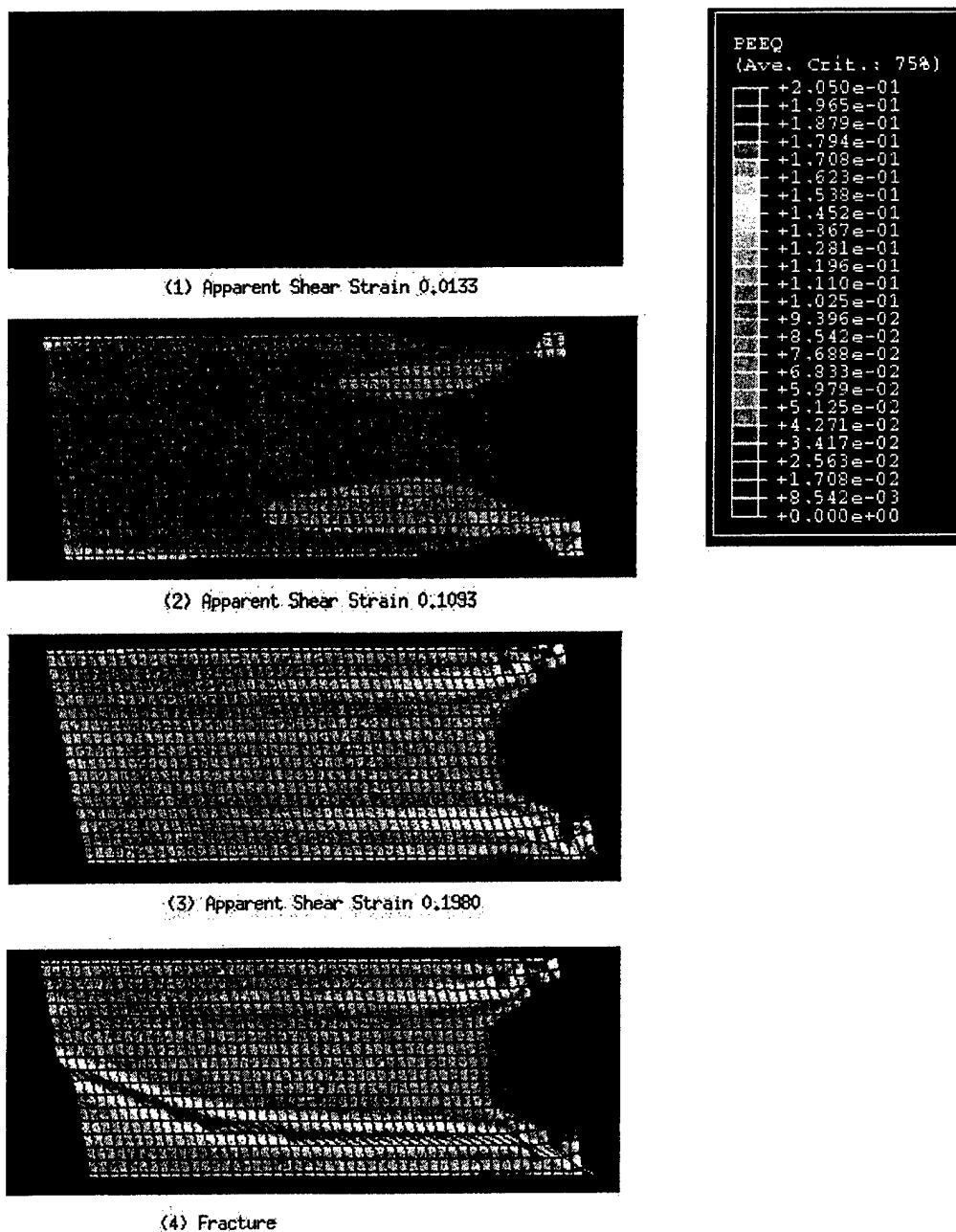
Note: The scale coordinates factor in through-thickness direction is 4, along loading direction is 1.

FIGURE 3-30. PEEQ DISTRIBUTION IN ADHESIVE WITH BONDLINE THICKNESS OF 0.013" AT FOUR TYPICAL STAGES



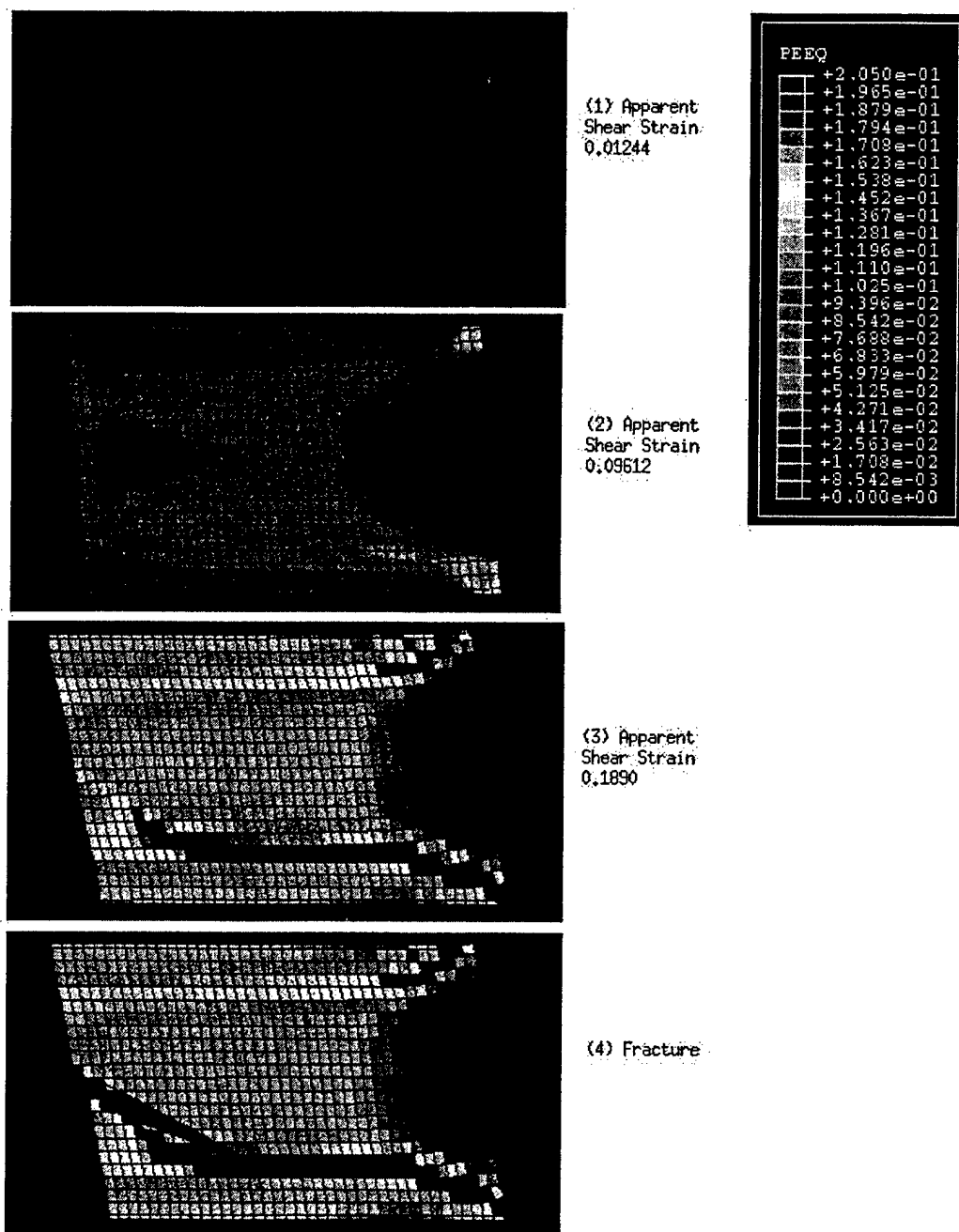
Note: The scale coordinates factor in through-thickness direction is 1.5, along loading direction is 1.

FIGURE 3-31. PEEQ DISTRIBUTION IN ADHESIVE WITH BONDLINE THICKNESS OF 0.040" AT FOUR TYPICAL STAGES



Note: The scale coordinates factor in through-thickness direction is 1, along loading direction is 1.

FIGURE 3-32. PEEQ DISTRIBUTION IN ADHESIVE WITH BONDLINE THICKNESS OF 0.080" AT FOUR TYPICAL STAGES



Note: The scale coordinates factor in through-thickness direction is 1, along loading direction is 1.

FIGURE 3-33. PEEQ DISTRIBUTION IN ADHESIVE WITH BONDLINE THICKNESS OF 0.120" AT FOUR TYPICAL STAGES

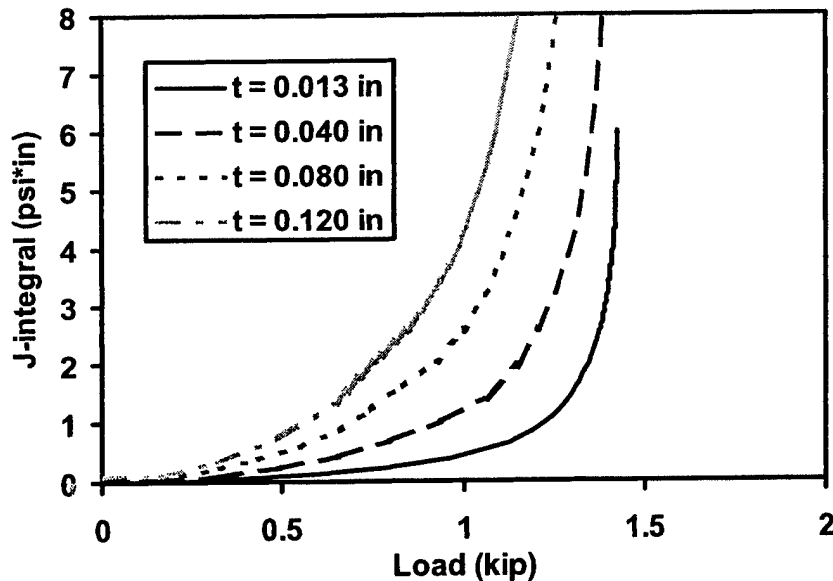


FIGURE 3-34. *J*-INTEGRAL FOR ASTM D 5656 OF SPECIMENS WITH FOUR BONDLINE THICKNESSES

TABLE 3-6. EXPERIMENTAL AND PREDICTED FAILURE LOADS BY *J*-INTEGRAL CRITERION (ASTM D 5656)

Adhesive Thickness (in)	Experimental Failure Load (lb)	Predicted Failure Load (lb)	Deviation (%)
0.013	1,405	1,413	0.57
0.040	1,338	1,294	-3.2
0.080	1,256	1,116	-11
0.120	1,049	987	-6.0

3.4 RESULTS AND DISCUSSION OF ASTM D 3165 SPECIMENS.

The aim of the ASTM D 3165 standard test is to obtain comparative shear strengths of adhesive based on the specimen configuration specified in the standard. The simulation results in this section will be helpful in further understanding the failure mechanism and to determine the dominating factors contributing to joint strength.

3.4.1 Deformation Analysis (ASTM D 3165).

Similarly to the analysis of ASTM D 5656 specimens, the displacements along the transverse direction (y direction, as shown in figure 3-4) and along the load direction at the top and bottom adhesive/adherend interfaces, the through-thickness average peel strain and shear strain and the rotation angles of the overlap areas are analyzed to obtain an overall picture of how the specimens' configuration affect displacement fields.

Figures 3-35 to 3-38 show the displacements of the top and bottom adhesive/adherend interfaces in the load direction and the direction perpendicular to the load direction for specimens with different bondline thicknesses loaded with each corresponding failure load. Compared with those of ASTM D 5656 specimens in figures 3-9 to 3-12, note that the specimens in both the two standard tests have clearly different displacement characteristics. The displacements of ASTM D 3165 specimens in the transverse direction are more than ten times larger than those of ASTM D 5656 specimens with all four bondline thicknesses. This is because the bending stiffness of the adherends of ASTM D 3165 specimens is much lower than those of ASTM D 5656 specimens. However, displacements along the load direction at failure are not as large as those of ASTM D 5656 specimens, because the ASTM D 3165 specimens have different failure mechanisms and their failure occurs before the appearance of large plastic deformation in the adhesive layer. In contrast, there are large plastic deformations in the adhesive of ASTM D 5656 specimens at failure.

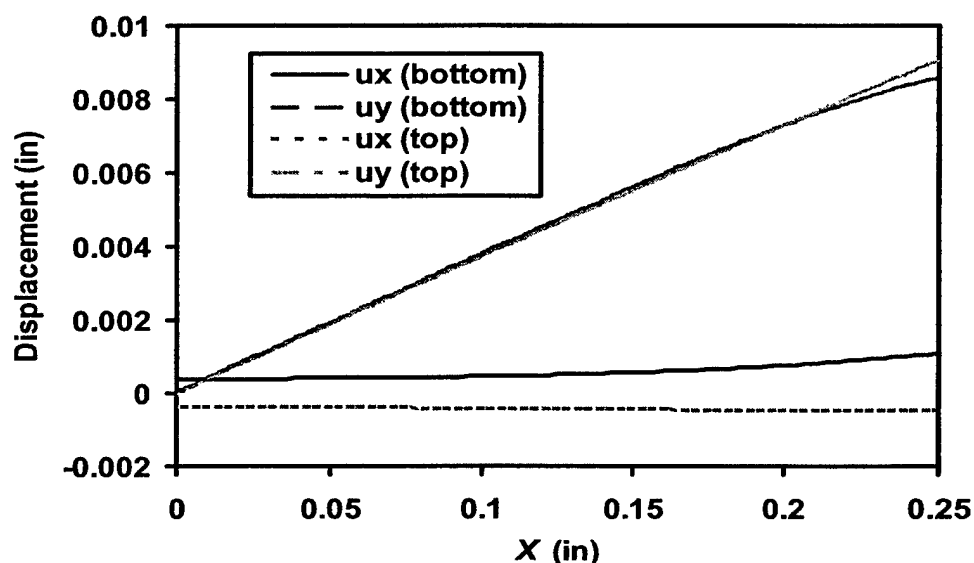


FIGURE 3-35. DISPLACEMENT OF ASTM D 3165 SPECIMEN WITH BONDLINE THICKNESS OF 0.013" AT FAILURE LOAD (1.40 kips)

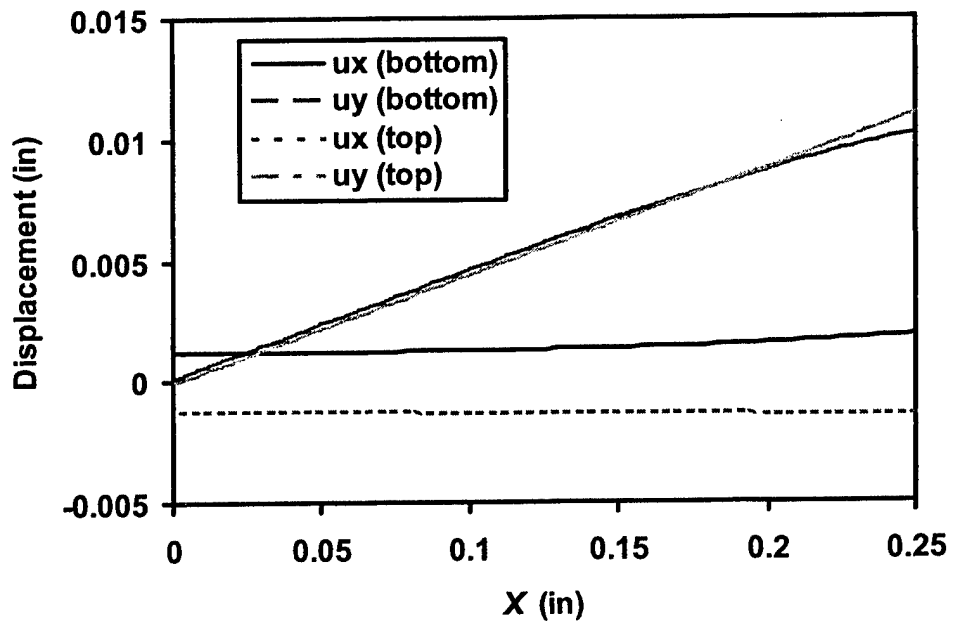


FIGURE 3-36. DISPLACEMENT OF ASTM D 3165 SPECIMEN WITH BONDLINE THICKNESS OF 0.040" AT FAILURE LOAD (1.10 kips)

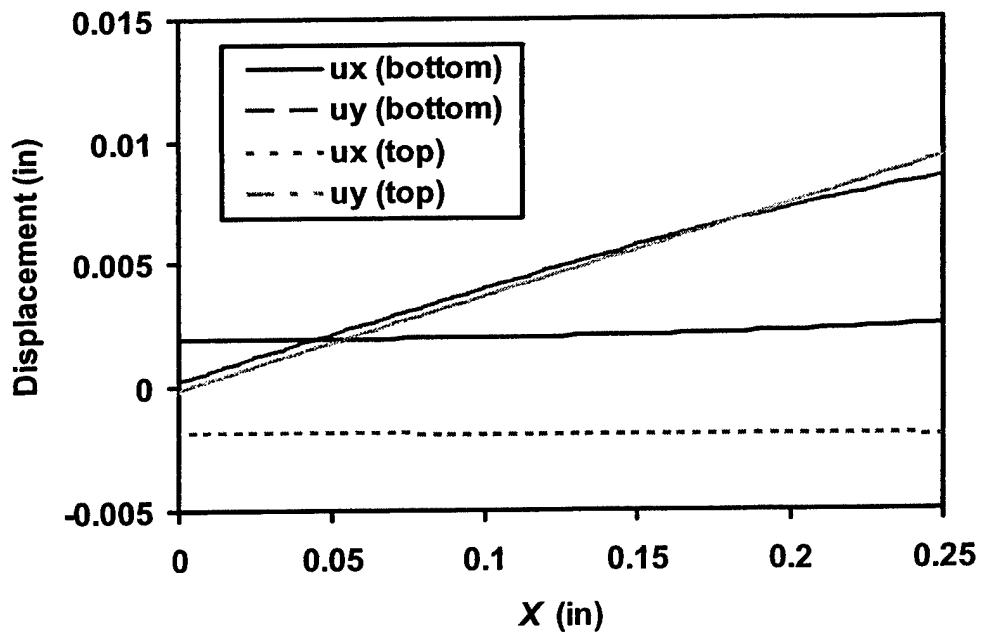


FIGURE 3-37. DISPLACEMENT OF ASTM D 3165 SPECIMEN WITH BONDLINE THICKNESS OF 0.080" AT FAILURE LOAD (0.677 kips)

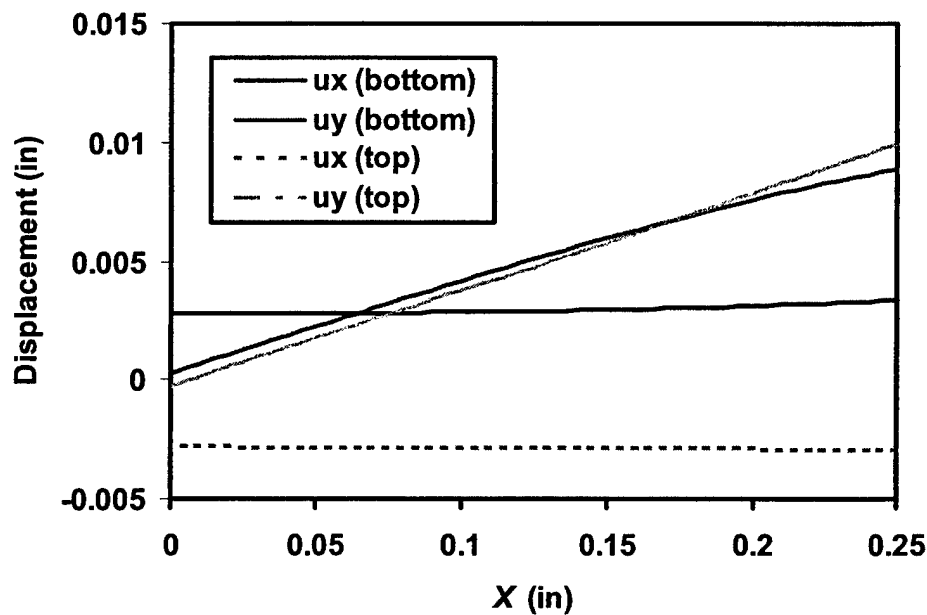


FIGURE 3-38. DISPLACEMENT OF ASTM D 3165 SPECIMEN WITH BONDLINE THICKNESS OF 0.120" AT FAILURE LOAD (0.510 kips)

Because displacements are generally linear functions of x , the angle of rotation of the overlap can be estimated. As shown in table 3-7, the angle of rotation for ASTM D 3165 specimens is about ten times larger than those of ASTM D 5656. Also, because the adherends at the notches have plastic deformation, permanent rotation exists after the load is removed.

TABLE 3-7. ANGLE OF ROTATION OF OVERLAP AREA OF ASTM D 3165 SPECIMENS AT FAILURE LOAD

Bondline Thickness (in)	Failure Load (kips)	Rotation Angle of Bondline
0.013	1.40	2.022°
0.040	1.10	2.437°
0.080	0.677	2.043°
0.120	0.510	2.153°

The angles of rotation are large enough to change the stress distribution inside the adhesive in the deformed shape. However, because the deformation due to bending of the adherends is mainly located at the notches, the stresses at the vicinity of the edges of the overlap are influenced significantly.

Figure 3-39 shows the through-thickness adhesive shear strain distribution for ASTM D 3165 specimens, without applying any failure criterion, for different bondline thicknesses at each respective experimental failure load. It can be seen that the through-thickness adhesive shear

strains for bondline thicknesses of 0.04" and 0.013" vary greatly along the load direction. Similarly, the through-thickness peel strains shown in figure 3-40 change greatly along the load direction, especially for the specimen with 0.013" bondline thickness. Compared with the through-thickness average adhesive shear and peel strain of ASTM D 5656 specimens, as given in figures 3-13 and 3-14, it is obvious that the ASTM D 5656 specimens have approximately twice the shear strain as ASTM D 3165 specimens, but ASTM D 3165 specimens have much greater adhesive peel strain. These results suggest that both the peel and shear stress play important rolls in the failure assessment of ASTM D 3165 specimens.

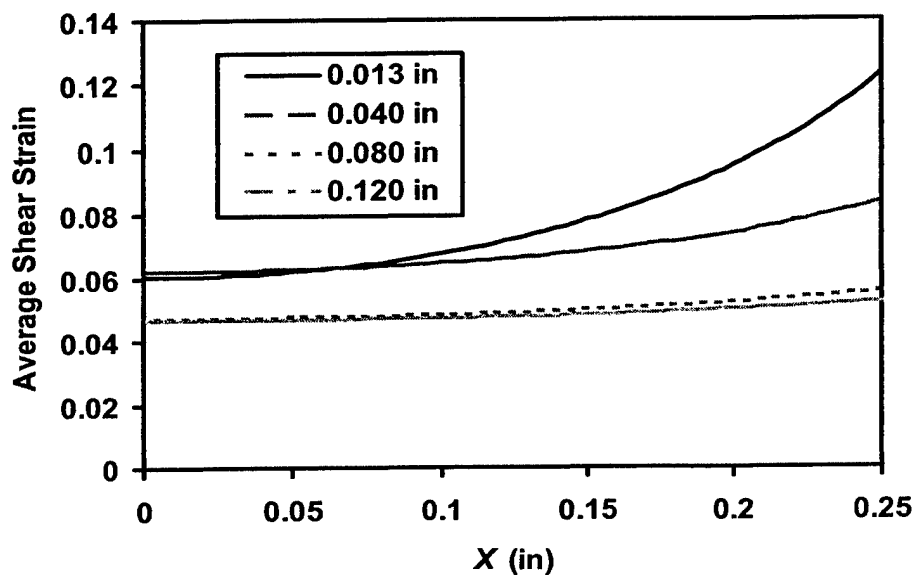


FIGURE 3-39. THROUGH-THICKNESS AVERAGE ADHESIVE SHEAR STRAIN WITHIN OVERLAP AT EACH RESPECTIVE FAILURE LOAD (ASTM D 3165)

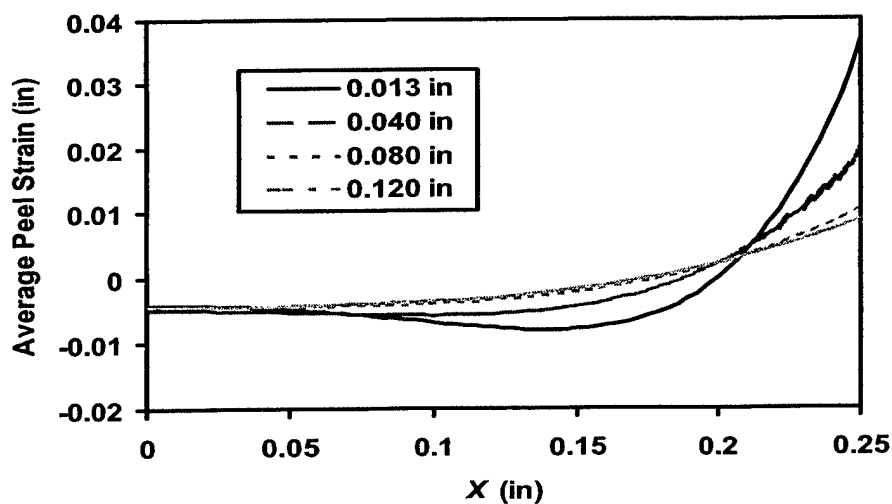


FIGURE 3-40. THROUGH-THICKNESS AVERAGE ADHESIVE PEEL STRAIN WITHIN OVERLAP AT EACH RESPECTIVE FAILURE LOAD (ASTM D 3165)

3.4.2 Stress Analysis (ASTM D 3165).

As mentioned in the previous stress analysis of ASTM D 5656 specimens, the adhesive shear stress is the major mechanism that transfers the load from one adherend to the other. The adhesive shear stress distribution determines the mechanical behavior of the joint and is closely related to joint failure. Figures 3-41 to 3-44 show the shear stress distributions of specimens with four different bondline thicknesses under a load of 800 lbs. The five curves in each figure represent the five paths in the adhesive, as defined in figure 3-15. The five-path average shear stress distribution for each bondline thickness is shown in figure 3-45.

It can be seen that shear stress distributions of ASTM D 3165 specimens vary dramatically compared with those of ASTM D 5656 specimens. The shear stress at the middle of the overlap is low, while the shear stress near the end of the overlap is high. Because the adherends of ASTM D 3165 specimens are thinner than ASTM D 5656 specimens, their stiffness is much lower, which leads to the nonuniformity of shear stress distribution. Stress nonuniformity results in lower joint strength because damage occurs in the high stress area, while the material at low stress area has not been fully used for its load-carrying capability.

Another important feature is the large free-boundary effect of ASTM D 3165 specimens. Because of the thinner adherends of the ASTM D 3165 specimens compared with ASTM D 5656 specimens, ASTM D 3165 specimens' adhesive has larger free surfaces in relation to adherend thickness, where the adhesive stress must equal zero.

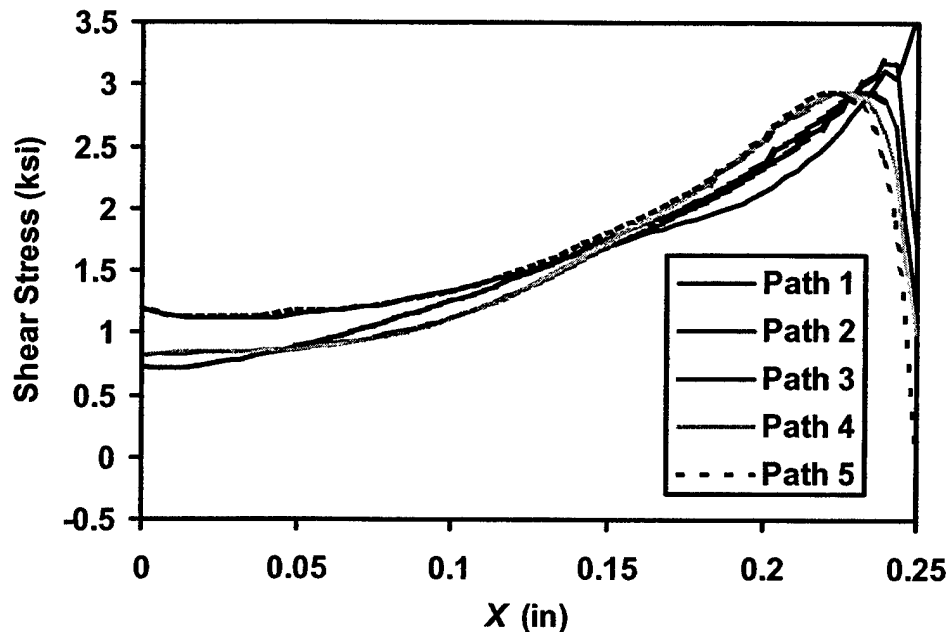


FIGURE 3-41. ADHESIVE SHEAR STRESS DISTRIBUTION (0.013" BONDLINE THICKNESS, ASTM D 3165)

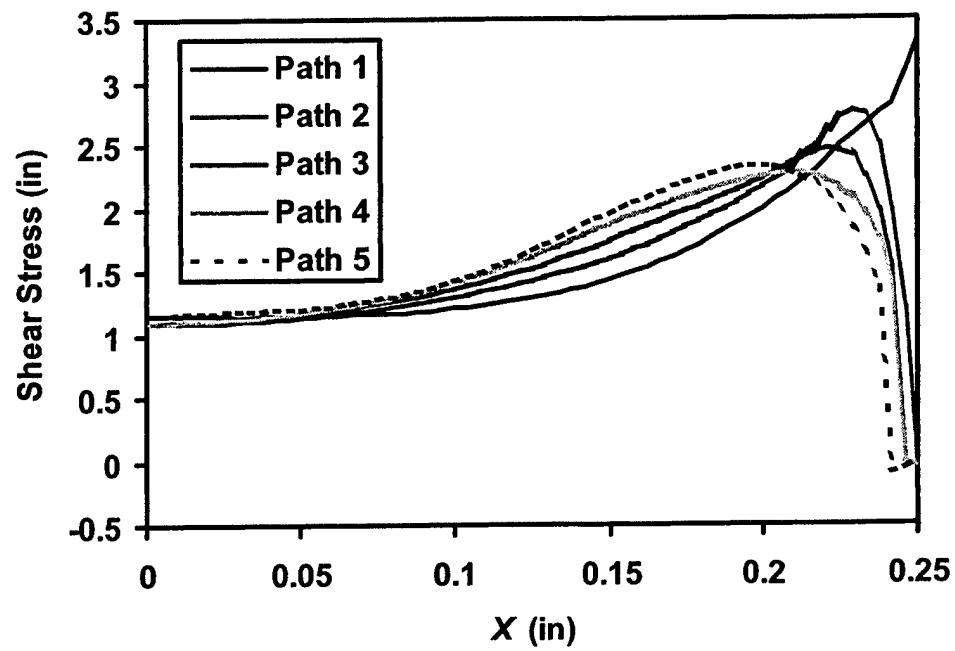


FIGURE 3-42. ADHESIVE SHEAR STRESS DISTRIBUTION (0.040" BONDLINE THICKNESS, ASTM D 3165)

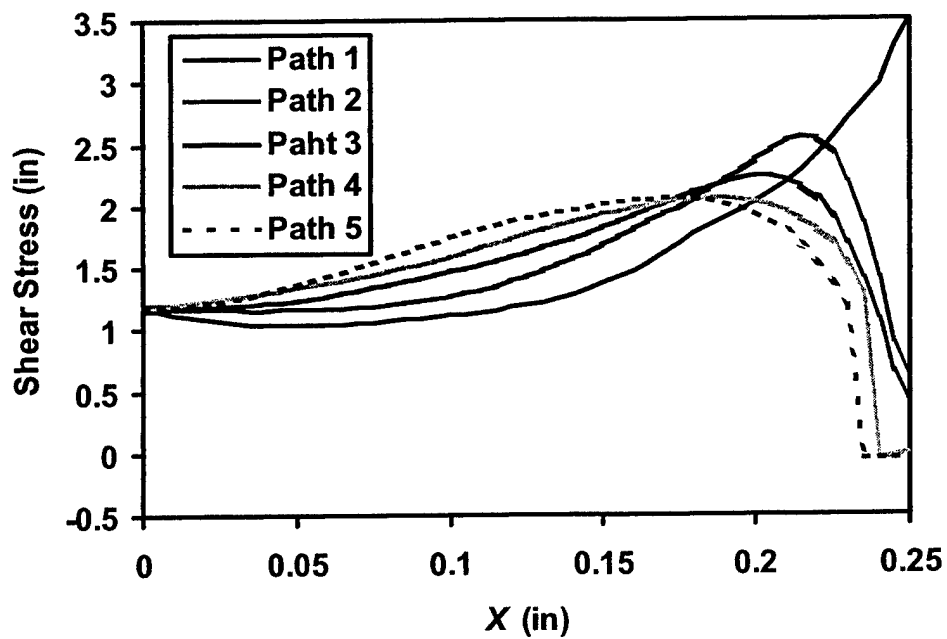


FIGURE 3-43. ADHESIVE SHEAR STRESS DISTRIBUTION (0.080" BONDLINE THICKNESS, ASTM D 3165)

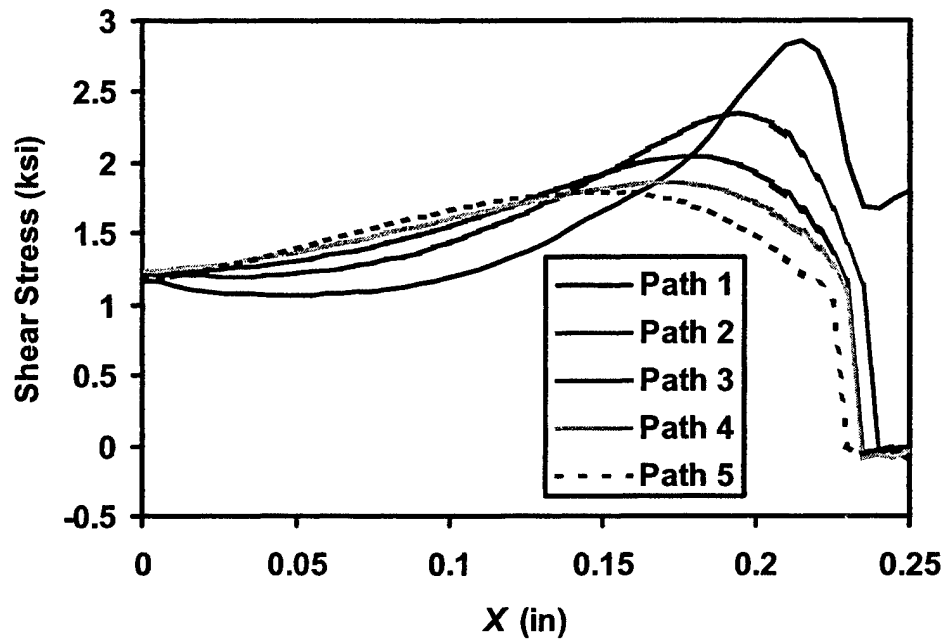


FIGURE 3-44. ADHESIVE SHEAR STRESS DISTRIBUTION (0.120" BONDLINE THICKNESS, ASTM D 3165)

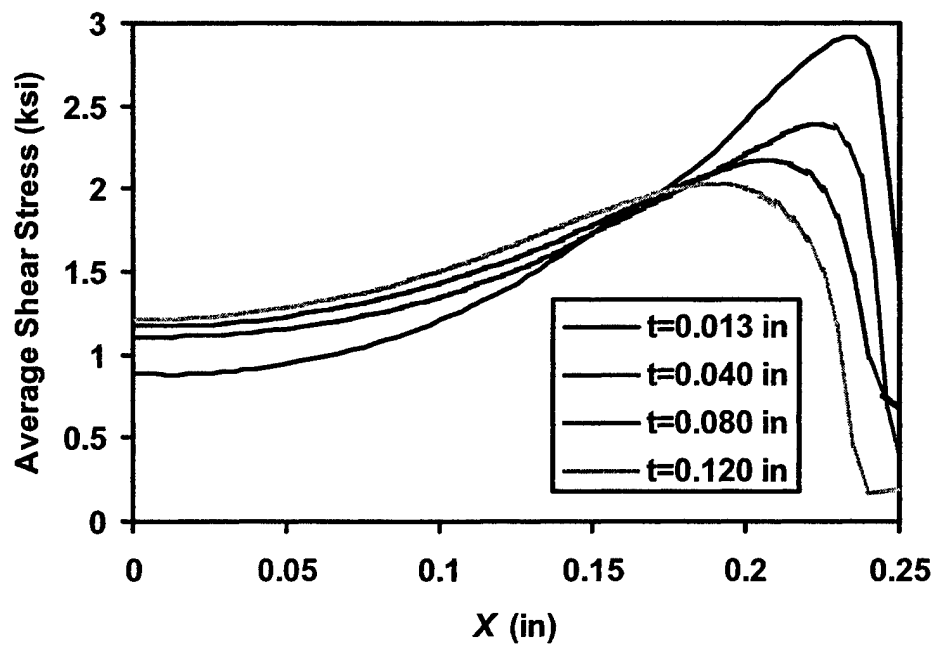


FIGURE 3-45. FIVE-PATH AVERAGE ADHESIVE SHEAR STRESS DISTRIBUTION (ASTM D 3165)

Figure 3-46 indicates the development of shear stress during the loading process. Figure 3-47 shows the development of force while the displacement at the loading end increases. Both figures show the results obtained from the specimen with bondline thickness of 0.12". It can be seen that the trend of shear stress distribution at different loads are quite similar. By comparing figure 3-47 with figure 3-22, it can be seen that the end joint displacement of ASTM D 3165 specimens is much greater than those in ASTM D 5656 specimens at the same load because ASTM D 3165 specimens have much thinner adherends.

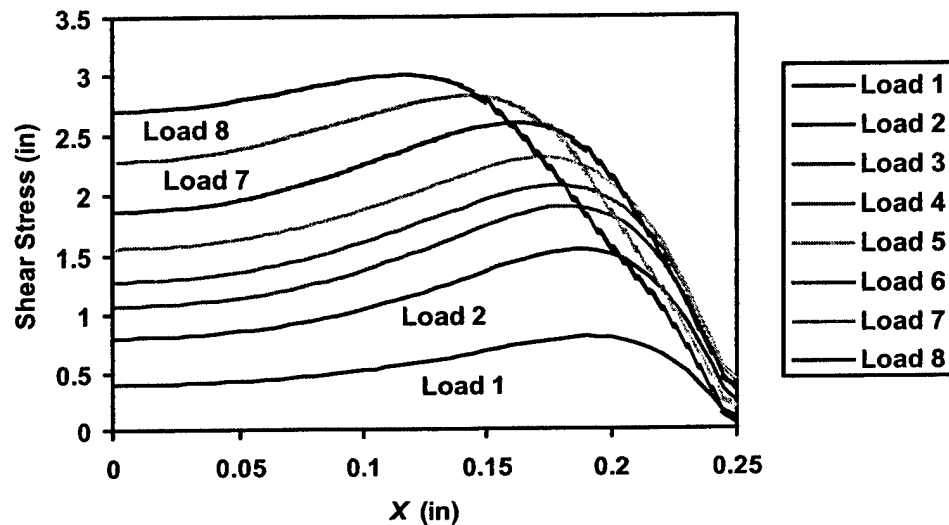


FIGURE 3-46. DEVELOPMENT OF SHEAR STRESS DISTRIBUTION ALONG PATH 3 (0.12" BONDLINE THICKNESS, ASTM D 3165)

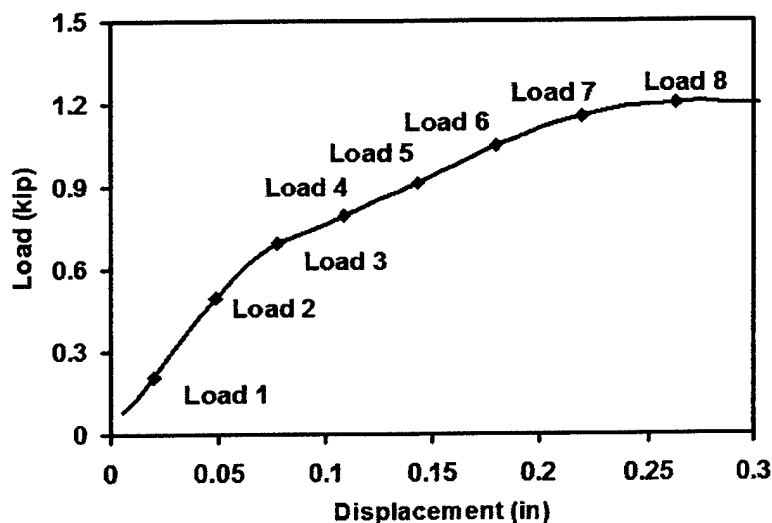


FIGURE 3-47. LOAD VERSUS JOINT-END DISPLACEMENT (0.12" BONDLINE THICKNESS, ASTM D 3165)

3.4.3 Failure Mode and Failure Criterion (ASTM D 3165).

Based on the experimental failure loads of the specimen (table 3-7) and the load-displacement curves shown in figure 3-48, ASTM D 3165 specimens fail before the adhesive yield stress has fully developed in the overlap. In other words, the failure mechanism of ASTM D 3165 specimens appears to be different from the failure mechanism of ASTM D 5656 specimens. The failure of ASTM D 5656 specimens occurs after the accumulation of a large plastic strain. However, ASTM D 3165 specimens fail before the load-displacement curve levels off. This suggests that the failure of ASTM D 3165 specimens might begin at some critical location, propagate quickly, and finally rupture. The brittle failure of ASTM D 3165 specimens also suggests the possibility of using a fracture mechanics approach, such as the J -integral, to analyze their failure.

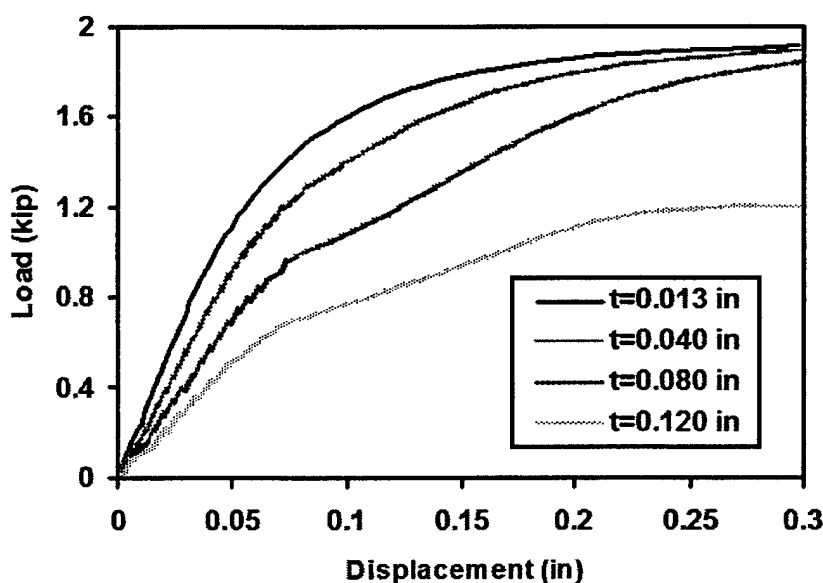


FIGURE 3-48. LOAD VERSUS JOINT-END DISPLACEMENT (ASTM D 3165)

According to the finite element models, the critical location of stress is at the lower right corner of the adhesive, as shown in figure 3-49. Figures 3-50 to 3-53 show the curves of adhesive shear stress, adhesive peel stress, PEEQ, and J -integral versus applied load, respectively, at the critical location. The respective values of adhesive shear stress, peel stress, PEEQ, and J -integral under experimental failure loads are listed in table 3-8. Clearly, the peel stress, shear stress, and PEEQ cannot be used as the failure index of ASTM D 3165 specimens. Based on trial calculation, if an appropriate value of J -integral is chosen as the failure criterion of models with a precrack, the failure loads calculated are close to those from experimental data. As listed in table 3-8, a fairly good prediction of failure loads can be achieved when the critical J -integral value (J_c) is chosen as 4 psi-in. As shown in table 3-9, once J_c is chosen as 4 psi-in, the predicted failure loads are compared with the experimental results for the ASTM D 3165 specimen with four different bondline thicknesses.

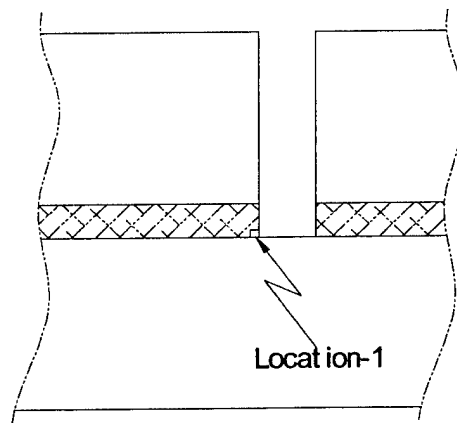


FIGURE 3-49. CRITICAL LOCATION INSIDE ADHESIVE LAYER (ASTM D 3165)

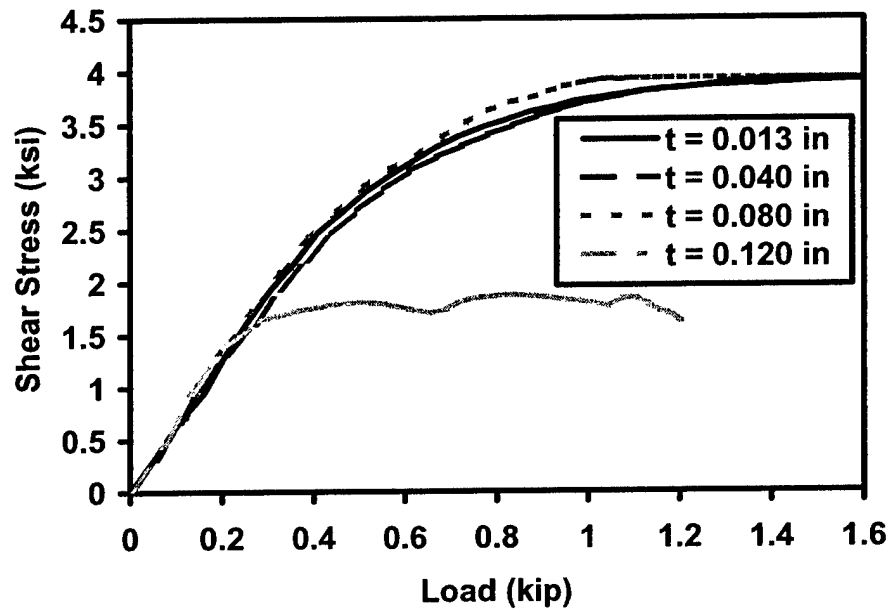


FIGURE 3-50. ADHESIVE SHEAR STRESS VERSUS LOAD AT LOCATION 1 (ASTM D 3165)

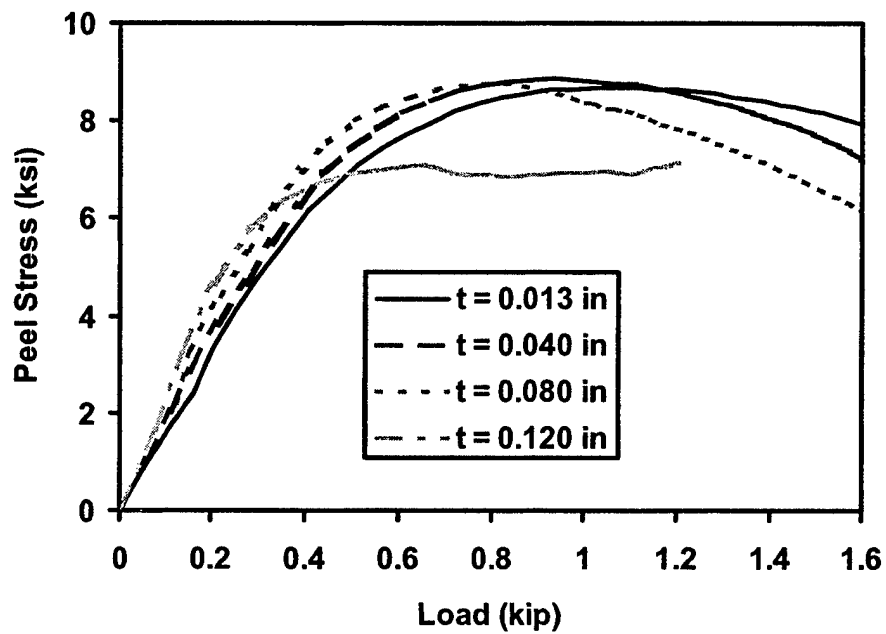


FIGURE 3-51. ADHESIVE PEEL STRESS VERSUS LOAD AT LOCATION 1 (ASTM D 3165)

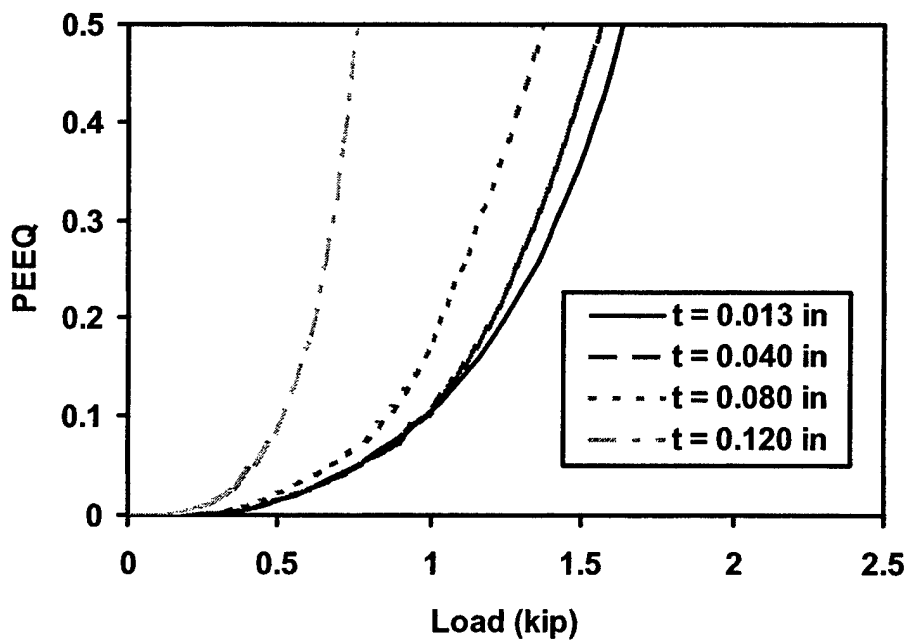


FIGURE 3-52. PEEQ VERSUS LOAD AT LOCATION 1 (ASTM D 3165)

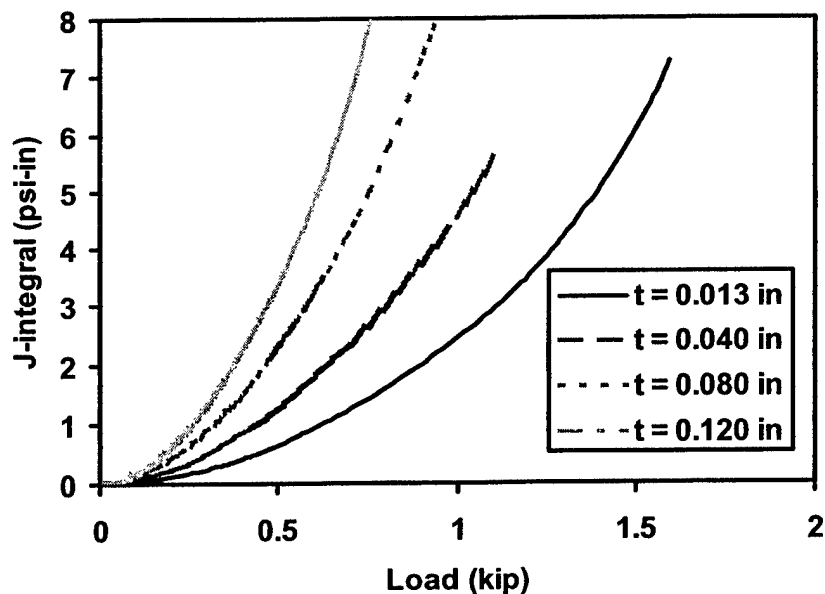


FIGURE 3-53. *J*-INTEGRAL VERSUS LOAD AT LOCATION 1 (ASTM D 3165)

TABLE 3-8. CORRESPONDING VALUES AT FAILURE LOADS FOR ASTM D 3165

Adhesive Thickness (in)	Experimental Failure Load (lb)	Shear Stress (ksi)	Peel Stress (ksi)	PEEQ	<i>J</i> -integral (psi-in)
0.013	1,405	3.88	8.37	0.29	5.1
0.040	1,099	3.64	8.87	0.088	4
0.080	677	3.36	8.63	0.05	4
0.120	510	1.81	6.91	0.095	3.44

TABLE 3-9. COMPARISON OF PREDICTED FAILURE LOADS WITH EXPERIMENTAL RESULTS FOR ASTM D 3165 USING $J_c = 4$ psi-in

Adhesive Thickness (in)	Experimental Failure Load (lb)	Predicted Failure Load (lb)	Deviation (%)
0.013	1,405	1,269	-9.7
0.040	1,099	934	-15
0.080	677	678	0.15
0.120	510	552	8.2

3.5 PARAMETERS AFFECTING JOINT PERFORMANCE.

3.5.1 Adherend Thickness.

With the same approach used to simulate ASTM D 3165 specimens, finite element models with double and triple the original adherend thickness of ASTM D 3165 specimens (0.064") are used to show the effects of adherend thickness on the joint strength. The calculated J -integral values as functions of applied load for specimens with double and triple adherend thicknesses are shown in figures 3-54 and 3-55, respectively. When using 4 psi-in as the critical J -integral value (J_c), the calculated failure load increases as the adherend thickness increases, as shown in figure 3-56. Furthermore, it can be seen from figure 3-56 that the failure load decreases when the adhesive becomes thicker.

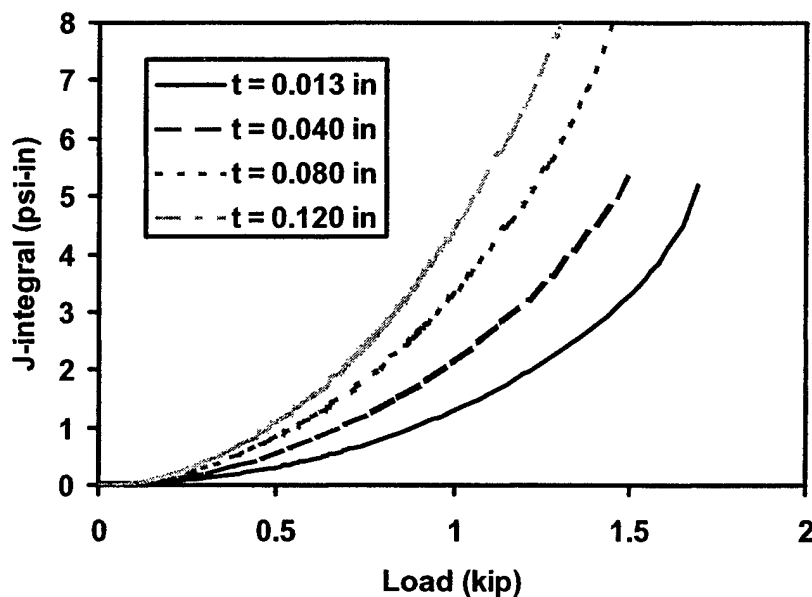


FIGURE 3-54. J -INTEGRAL FOR ASTM D 3165 CONFIGURATION WITH DOUBLE ADHEREND THICKNESS

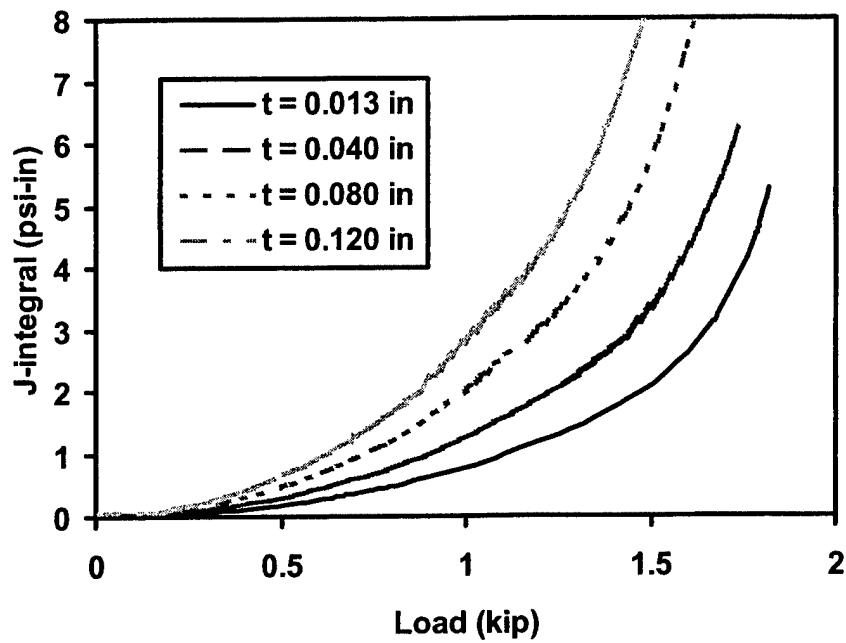


FIGURE 3-55. *J*-INTEGRAL FOR ASTM D 3165 CONFIGURATION WITH TRIPLE ADHEREND THICKNESS

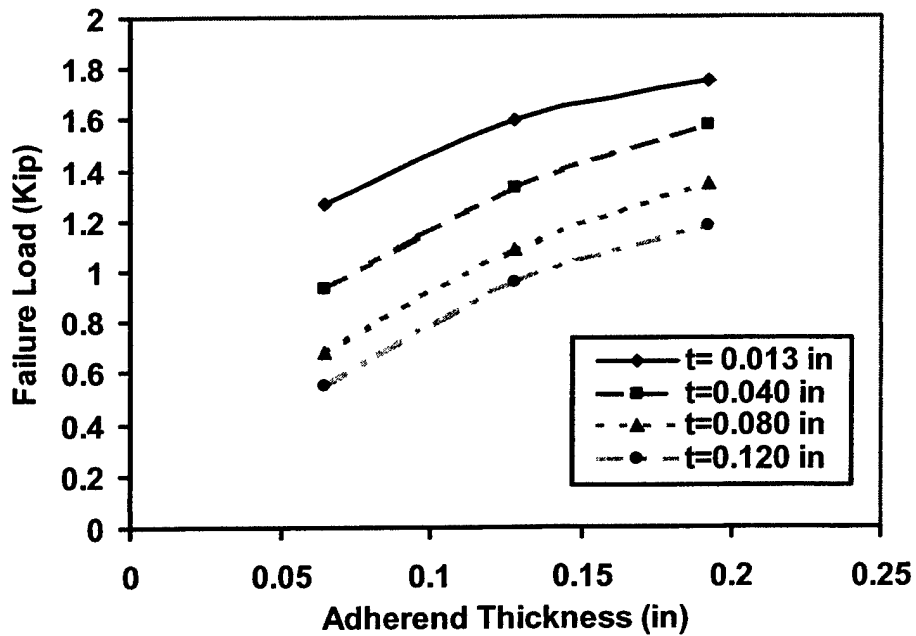


FIGURE 3-56. FAILURE LOAD VERSUS ADHEREND THICKNESS

3.5.2 Adherend Stiffness.

The calculated J -integral value versus applied load for ASTM D 3165 specimens with different adherend moduli is shown in figure 3-57. If 4 psi-in is used as the critical value for J -integral as the joint failure criterion, the relationship between the failure load and adherend Young's modulus is shown in figure 3-58. It can be seen that with the same joint geometry, a joint with steel adherends would be stronger than one with aluminum adherends. With the same approach and the same joint failure criterion, figures 3-59 and 3-60 show the effects of adherend modulus on joint strength of ASTM D 5656 specimens. Because the ASTM D 5656 specimens already have thick adherends with large bending and tensile rigidities, increasing the adherend modulus does not contribute to higher joint strength.

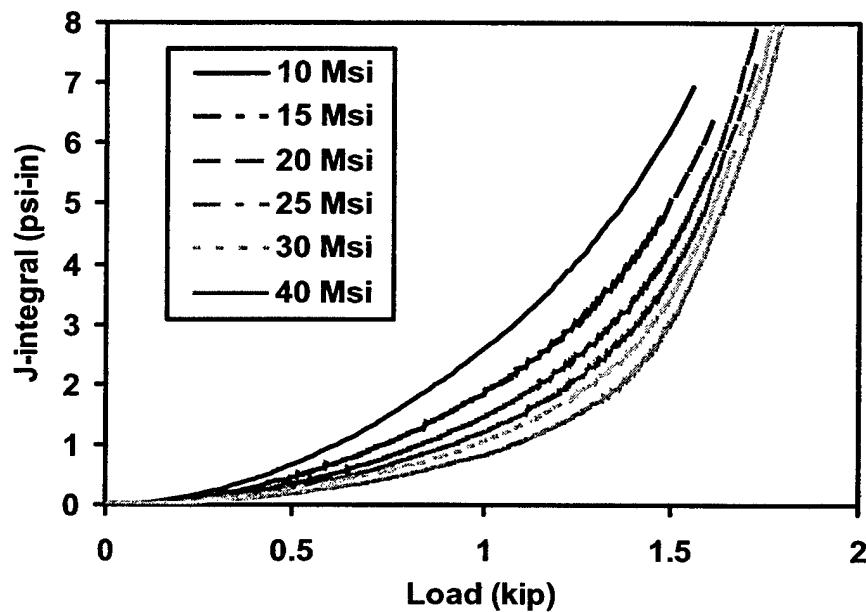


FIGURE 3-57. J -INTEGRAL VERSUS LOAD FOR WITH DIFFERENT ADHEREND YOUNG'S MODULI (0.013" BONDLINE THICKNESS, ASTM D 3165)

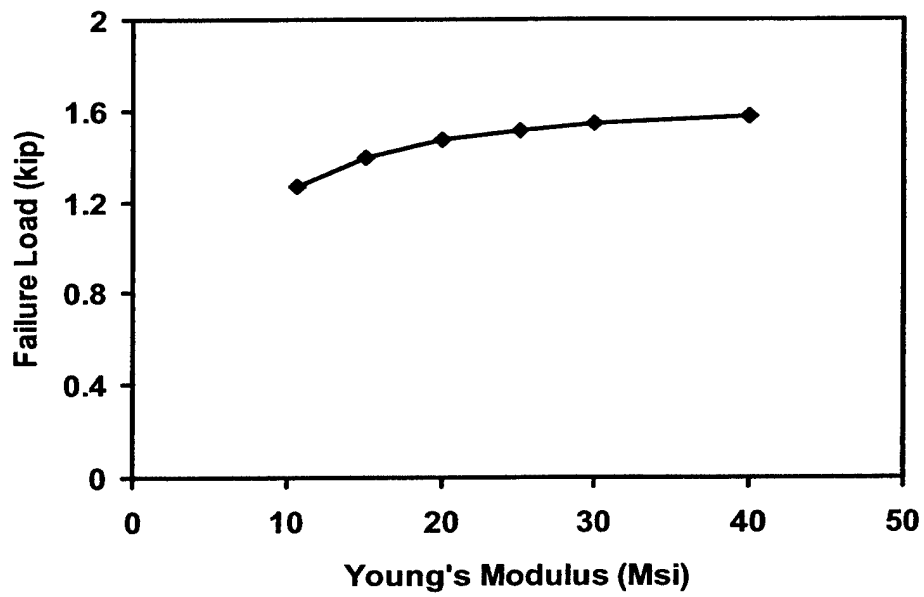


FIGURE 3-58. FAILURE LOAD VERSUS ADHEREND YOUNG'S MODULUS (0.013" BONDLINE THICKNESS, ASTM D 3165)

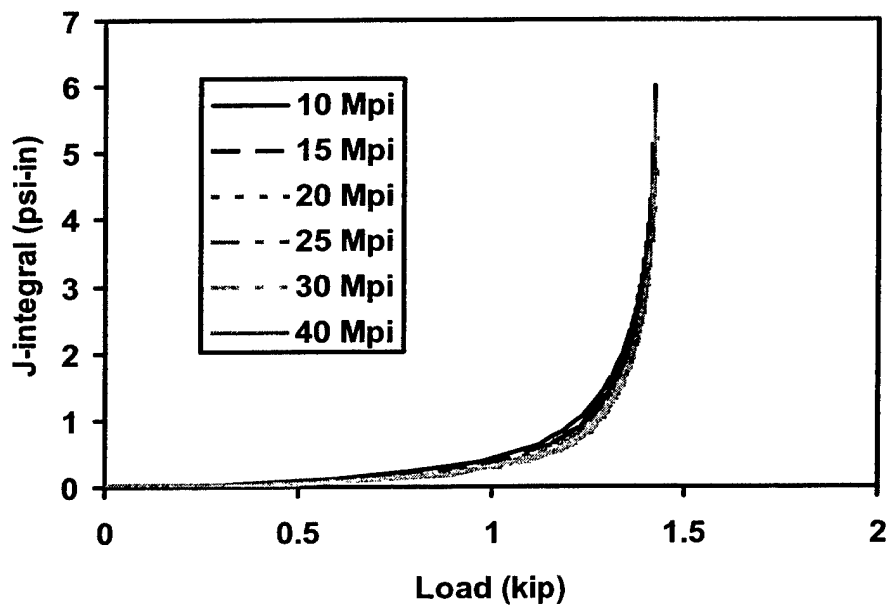


FIGURE 3-59. J-INTEGRAL VERSUS LOAD FOR WITH DIFFERENT ADHEREND YOUNG'S MODULI (0.013" BONDLINE THICKNESS, ASTM D 5656)

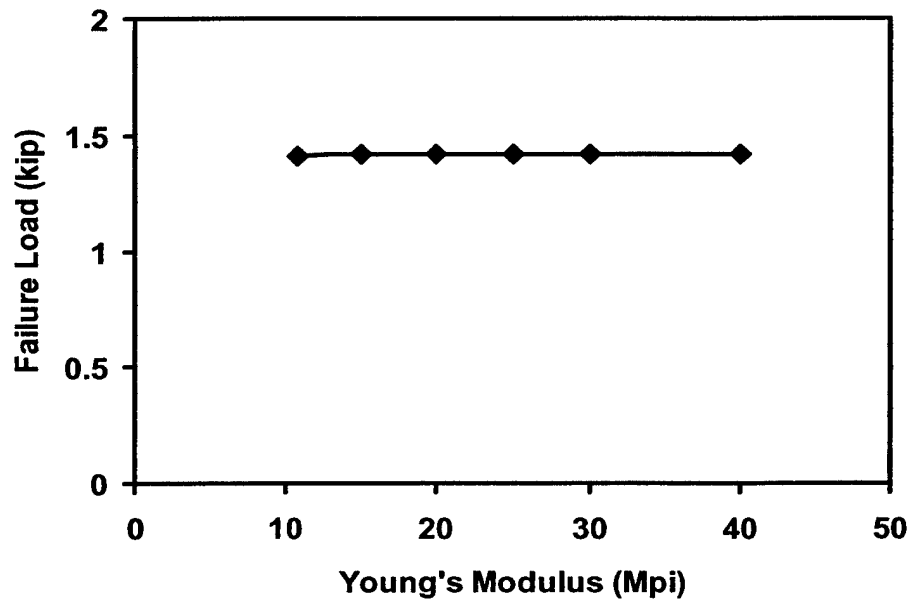


FIGURE 3-60. FAILURE LOAD VERSUS ADHEREND YOUNG'S MODULUS
(0.013" BONDLINE THICKNESS, ASTM D 5656)

3.5.3 Adherend Plasticity.

In the finite element simulation conducted in this research, elastic-perfectly plastic behavior is assumed for the aluminum adherends of both ASTM D 5656 and D 3165 specimens. This is reasonable for ASTM D 5656 specimens because the large thickness of ASTM D 5656 aluminum adherends results in minimal yielding in the adherend. In order to validate the use of elastic-perfectly plastic material properties of aluminum adherend for ASTM D 3165 specimens, comparisons are made between finite element models with plastic and elastic-perfectly plastic aluminum properties. Figures 3-61 and 3-62 show the calculated J -integral versus applied load with two material models for ASTM D 3165 joints with 0.04" and 0.08" bondline thicknesses, respectively. The fact that almost no distinction exists between the two curves shown in figures 3-61 and 3-62, especially at the 4 psi-in J -integral level, confirms the appropriateness of using elastic-perfectly plastic material model for aluminum adherends.

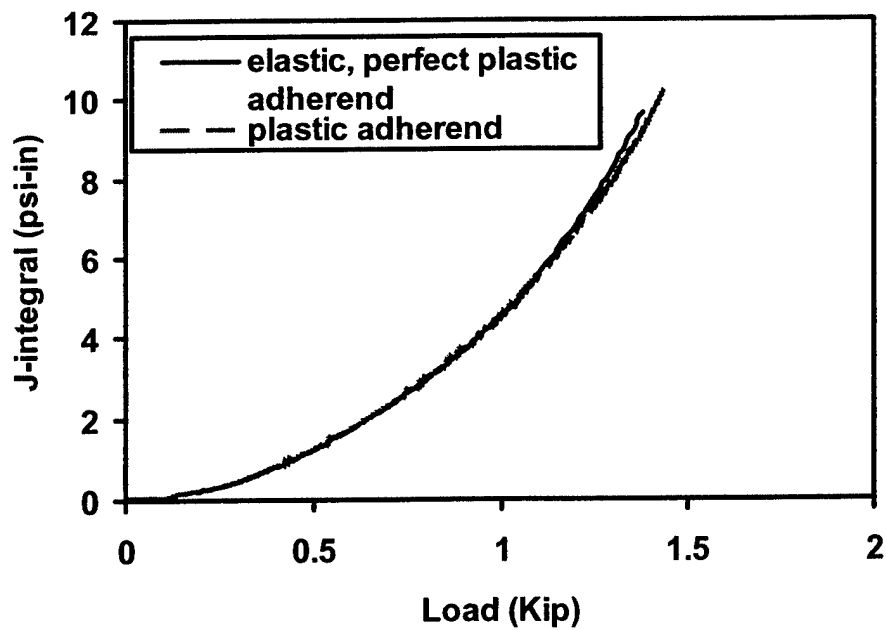


FIGURE 3-61. COMPARISON BETWEEN DIFFERENT MATERIAL MODELS FOR ALUMINUM ADHERENDS (0.04" BONDLINE THICKNESS, ASTM D 3165)

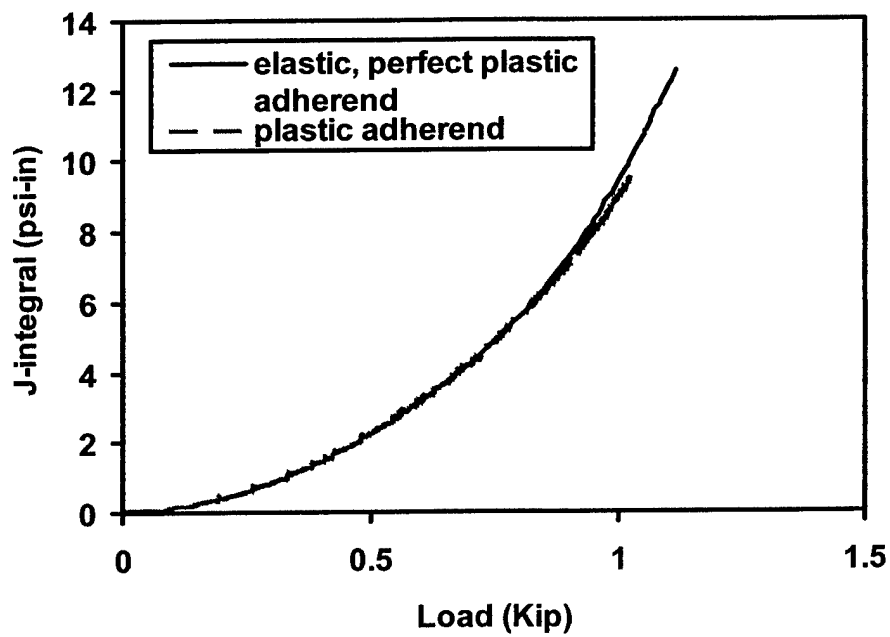


FIGURE 3-62. COMPARISON BETWEEN DIFFERENT MATERIAL MODELS FOR ALUMINUM ADHERENDS (0.08" BONDLINE THICKNESS, ASTM D 3165)

4. CONCLUSION.

An analytical model for adhesive-bonded single-lap joints under tension was developed based on the first-order laminated plate theory for the adherend and on elastic-perfectly plastic behavior for the adhesive. Based on the developed model, closed-form solutions for stress distributions of both the laminates and the adhesive were obtained. The proposed closed-form solutions were found to correlate with the solutions obtained through finite element models. Several joint failure criteria were proposed and evaluated with experimental data.

Extensive finite element modeling was performed to analyze both ASTM D 5656 and D 3165 specimen behavior. With the displacement and stress fields obtained through finite element calculation, phenomena from experimental observations, such as different shear moduli obtained from ASTM D 5656 specimens with different bondline thickness, were explained. The proposed failure criteria, the equivalent adhesive plastic strain and J -integral, were used effectively to predict the joint strength of ASTM D 5656 and D 3165 specimens. The calculated joint strengths correlate well with the experimental results. The effects on joint strength due to bondline thickness, adherend thickness, and adherend modulus were also investigated.

5. REFERENCES.

1. Kutscha, D., "Mechanics of Adhesive-Bonded Lap-Type Joints: Survey and Review," Technical Report AFML-TDR-64-298, 1964.
2. Kutscha, D. and Hofer, K.E. Jr., "Feasibility of Joining Advanced Composite Flight Vehicles," Technical Report AFML-TR-68-391, 1969.
3. Matthews, F.L., Kilty, P.F., and Goodwin, E. W., "A Review of the Strength of Joints in Fibre-Reinforced Plastics: Part 2 Adhesively Bonded Joints," *Composites*, pp. 29-37, 1982.
4. Vinson, J.R., "Adhesive Bonding of Polymer Composites," *Polymer Engineering and Science*, Vol. 29, pp. 1325-31, 1989.
5. Goland, M. and Reissner, E., "The Stresses in Cemented Joints," *Journal of Applied Mechanics*, Vol. 11, pp. A-17-A-27, 1944.
6. Hart-Smith, L.J., "Adhesive-Bonded Single-Lap Joints," Douglas Aircraft Co., NASA Langley Report CR 112236, 1973.
7. Hart-Smith, L.J., "Adhesive-Bonded Double-Lap Joints," Douglas Aircraft Co., NASA Langley Report CR 112235, 1973.
8. Hart-Smith, L.J., "Adhesive-Bonded Scarf and Stepped-Lap Joints," Douglas Aircraft Co., NASA Langley Report CR 112237, 1973.
9. Hart-Smith, L.J., "Analysis and Design of Advanced Composite Bonded Joints," Douglas Aircraft Co., NASA Langley Report CR-2218, 1974.
10. Reissner, E., "The Effect of Transverse Shear Deformation on the Bending of Elastic Plates," *Journal of Applied Mechanics*, Vol. 12, pp. A-69-A-77, 1945.
11. Reddy, J.N., "A Refined Nonlinear Theory of Plates With Transverse Shear Deformation," *International Journal of Solids Structures*, Vol. 20, pp. 881-96, 1984.
12. Renton, W.J. and Vinson, J.R., "Analysis of Adhesively Bonded Joints Between Panels of Composite Materials," *Journal of Applied Mechanics*, Vol. 44, pp. 101-06, 1977.
13. Yang, C., Pang, S.S., and Griffin, S.A., "Failure Analysis of Adhesive-Bonded Double-Lap Joints Under Cantilevered Bending," *Polymer Engineering and Science*, Vol. 32, pp. 632-40, 1992.
14. Yang, C. and Pang, S.S., "Stress-Strain Analysis of Single-Lap Composite Joints Under Cylindrical Bending," *Composites Engineering*, Vol. 3, pp. 1051-63, 1993.

15. Yang, C. and Pang, S.S., "Stress-Strain Analysis of Single-Lap Composite Joints Under Tension," ASME Transaction, *Journal of Engineering Materials and Technology*, Vol. 118, pp. 247-55, 1996.
16. Oplinger, D.W., "Effects of Adherend Deflections in Single Lap Joints," *International Journal of Solids and Structures*, Vol. 31, pp. 2565-87, 1994.
17. Tong, L., "An Assessment of Failure Criteria to Predict the Strength of Adhesively Bonded Composite Double Lap Joints," *Journal of Reinforced Plastics and Composites*, Vol. 16, No. 8, pp. 698-713, 1997.
18. Adams, R.D. and Davies, R., "Strength of Joints Involving Composites," *Journal of Adhesion*, Vol. 59, pp. 171-82, 1996.
19. Thomas, R., Garcia, F.J., and Adams, R.D., "Adhesive Joining of Composite Laminates," *Plastics, Rubber, and Composite Processing and Applications*, Vol. 27, No. 4, pp. 200-05, 1998.
20. Chai, H., "Micromechanics of Shear Deformations in Cracked Bonded Joints," *International Journal of Fracture*, Vol. 58, pp. 223-39, 1992.
21. Chai, H., "Deformation and Failure of Adhesive Bonds Under Shear Loading," *Journal of Materials Science*, Vol. 28, pp. 494-506, 1993.
22. Chai, H. and Chiang, M.Y.M., "A Crack Propagation Criterion Based on Local Shear Strain in Adhesive Bonds Subjected to Shear," *Journal of Mech. Phys. Solids*, Vol. 44, No. 10, pp. 1669-89, 1996.
23. Needleman, A. and Rosakis, A.J., "Effect of Bond Strength and Loading Rate on the Conditions Governing the Attainment of Intersonic Crack Growth Along Interfaces," *Journal of the Mechanics and Physics of Solids*, Vol. 47, No. 12, pp. 2411-49, 1999.
24. Charalambides, M.N., Hardouin, R., Kinloch, A.J., and Matthews, F.L., "Adhesively-Bonded Repairs to Fibre-Composite Materials I: Experimental," *Composites Part A*, Vol. 29A, pp. 1371-81, 1998.
25. Charalambides, M.N., Kinloch, A.J., and Matthews, F.L., "Adhesively-Bonded Repairs to Fibre-Composite Materials II: Finite Element Modeling," *Composites Part A*, Vol. 29A, pp. 1383-96, 1998.
26. Monagan M.B., K.O. Geddes, K.M. Heal, G. Labahn, and S. Vorkoetter, *Maple V Programming Guide*, Springer-Verlag, New York, 1996.
27. Yang, C., Huang, H., Tomblin, J.S., and Oplinger, D.W., "Evaluation and Adjustments for ASTM D 5656-Standard Test Method for Thick-Adherend Metal Lap-Shear Joints for Determination of the Stress-Strain Behavior of Adhesives in Shear by Tension Loading," *ASTM Journal of Testing and Evaluation*, Vol. 29, No. 1, pp. 36-43, 2001.

APPENDIX A—BOUNDARY CONDITIONS

Region 1 At $x_1 = 0$,

$$u^{oU} \Big|_{x_1=0} = 0 \quad (\text{A-1})$$

$$w^U \Big|_{x_1=0} = 0 \quad (\text{A-2})$$

$$M_y^U \Big|_{x_1=0} = 0 \quad (\text{A-3})$$

$$u^{oL} \Big|_{x_1=0} = 0 \quad (\text{A-4})$$

$$M_y^L \Big|_{x_1=0} = 0 \quad (\text{A-5})$$

$$Q_z^L \Big|_{x_1=0} = 0 \quad (\text{A-6})$$

At $x_1 = L_1$ ($x_{1p} = 0$),

$$u^{oU} \Big|_{x_1=L_1} = u^{oU} \Big|_{x_{1p}=0} \quad (\text{A-7})$$

$$\psi^U \Big|_{x_1=L_1} = \psi^U \Big|_{x_{1p}=0} \quad (\text{A-8})$$

$$w^U \Big|_{x_1=L_1} = w^U \Big|_{x_{1p}=0} \quad (\text{A-9})$$

$$N_x^U \Big|_{x_1=L_1} = N_x^U \Big|_{x_{1p}=0} \quad (\text{A-10})$$

$$M_y^U \Big|_{x_1=L_1} = M_y^U \Big|_{x_{1p}=0} \quad (\text{A-11})$$

$$Q_z^U \Big|_{x_1=L_1} = Q_z^U \Big|_{x_{1p}=0} \quad (\text{A-12})$$

$$u^{oL} \Big|_{x_1=L_1} = u^{oL} \Big|_{x_{1p}=0} \quad (\text{A-13})$$

$$\psi^L \Big|_{x_1=L_1} = \psi^L \Big|_{x_{1p}=0} \quad (\text{A-14})$$

$$w^L \Big|_{x_1=L_1} = w^L \Big|_{x_{1p}=0} \quad (\text{A-15})$$

$$N_x^L \Big|_{x_1=L_1} = N_x^L \Big|_{x_{1p}=0} \quad (\text{A-16})$$

$$M_y^L \Big|_{x_1=L_1} = M_y^L \Big|_{x_{1p}=0} \quad (\text{A-17})$$

$$Q_z^L \Big|_{x_1=L_1} = Q_z^L \Big|_{x_{1p}=0} \quad (\text{A-18})$$

At $x_{1p} = L_{1p}$,

$$u^{oU} \Big|_{x_{1p}=L_{1p}} = u^{oU} \Big|_{x_{2p}=0} \quad (\text{A-19})$$

$$\psi^U \Big|_{x_{1p}=L_{1p}} = \psi^U \Big|_{x_{2p}=0} \quad (\text{A-20})$$

$$w^U \Big|_{x_{1p}=L_{1p}} = w^U \Big|_{x_{2p}=0} \quad (\text{A-21})$$

$$N_x^U \Big|_{x_{1p}=L_{1p}} = N_x^U \Big|_{x_{2p}=0} \quad (\text{A-22})$$

$$M_y^U \Big|_{x_{1p}=L_{1p}} = M_y^U \Big|_{x_{2p}=0} \quad (\text{A-23})$$

$$Q_z^U \Big|_{x_{1p}=L_{1p}} = Q_z^U \Big|_{x_{2p}=0} \quad (\text{A-24})$$

$$N_x^L \Big|_{x_{1p}=L_{1p}} = 0 \quad (\text{A-25})$$

$$M_y^L \Big|_{x_{1p}=L_{1p}} = 0 \quad (\text{A-26})$$

$$Q_z^L \Big|_{x_{1p}=L_{1p}} = 0 \quad (\text{A-27})$$

Region 2 At $x_{2p} = 0$,

$$N_x^L \Big|_{x_{2p}=0} = 0 \quad (\text{A-28})$$

$$M_y^L \Big|_{x_{2p}=0} = 0 \quad (\text{A-29})$$

$$Q_z^L \Big|_{x_{2p}=0} = 0 \quad (\text{A-30})$$

At $x_{2p} = L_{2p}$ ($x_2 = 0$),

$$u^{oU} \Big|_{x_{2p}=L_{2p}} = u^{oU} \Big|_{x_2=0} \quad (\text{A-31})$$

$$\psi^U \Big|_{x_{2p}=L_{2p}} = \psi^U \Big|_{x_2=0} \quad (\text{A-32})$$

$$w^U \Big|_{x_{2p}=L_{2p}} = w^U \Big|_{x_2=0} \quad (\text{A-33})$$

$$N_x^U \Big|_{x_{2p}=L_{2p}} = N_x^U \Big|_{x_2=0} \quad (\text{A-34})$$

$$M_y^U \Big|_{x_{2p}=L_{2p}} = M_y^U \Big|_{x_2=0} \quad (\text{A-35})$$

$$Q_z^U \Big|_{x_{2p}=L_{2p}} = Q_z^U \Big|_{x_2=0} \quad (\text{A-36})$$

$$u^{oL} \Big|_{x_{2p}=L_{2p}} = u^{oL} \Big|_{x_2=0} \quad (\text{A-37})$$

$$\psi^L \Big|_{x_{2p}=L_{2p}} = \psi^L \Big|_{x_2=0} \quad (\text{A-38})$$

$$w^L \Big|_{x_{2p}=L_{2p}} = w^L \Big|_{x_2=0} \quad (\text{A-39})$$

$$N_x^L \Big|_{x_{2p}=L_{2p}} = N_x^L \Big|_{x_2=0} \quad (\text{A-40})$$

$$M_y^L \Big|_{x_{2p}=L_{2p}} = M_y^L \Big|_{x_2=0} \quad (\text{A-41})$$

$$Q_z^L \Big|_{x_{2p}=L_{2p}} = Q_z^L \Big|_{x_2=0} \quad (\text{A-42})$$

At $x_2 = L_2$ ($x_{2p'} = 0$),

$$u^{oU}|_{x_2=L_2} = u^{oU}|_{x_{2p'}=0} \quad (\text{A-43})$$

$$\psi^U|_{x_2=L_2} = \psi^U|_{x_{2p'}=0} \quad (\text{A-44})$$

$$w^U|_{x_2=L_2} = w^U|_{x_{2p'}=0} \quad (\text{A-45})$$

$$N_x^U|_{x_2=L_2} = N_x^U|_{x_{2p'}=0} \quad (\text{A-46})$$

$$M_y^U|_{x_2=L_2} = M_y^U|_{x_{2p'}=0} \quad (\text{A-47})$$

$$Q_z^U|_{x_2=L_2} = Q_z^U|_{x_{2p'}=0} \quad (\text{A-48})$$

$$u^{oL}|_{x_2=L_2} = u^{oL}|_{x_{2p'}=0} \quad (\text{A-49})$$

$$\psi^L|_{x_2=L_2} = \psi^L|_{x_{2p'}=0} \quad (\text{A-50})$$

$$w^L|_{x_2=L_2} = w^L|_{x_{2p'}=0} \quad (\text{A-51})$$

$$N_x^L|_{x_2=L_2} = N_x^L|_{x_{2p'}=0} \quad (\text{A-52})$$

$$M_y^L|_{x_2=L_2} = M_y^L|_{x_{2p'}=0} \quad (\text{A-53})$$

$$Q_z^L|_{x_2=L_2} = Q_z^L|_{x_{2p'}=0} \quad (\text{A-54})$$

At $x_{2p'} = L_{2p'}$ ($x_{3p} = 0$),

$$N_x^U|_{x_{2p'}=L_{2p'}} = 0 \quad (\text{A-55})$$

$$M_y^U|_{x_{2p'}=L_{2p'}} = 0 \quad (\text{A-56})$$

$$Q_z^U|_{x_{2p'}=L_{2p'}} = 0 \quad (\text{A-57})$$

$$u^{oL}|_{x_{2p'}=L_{2p'}} = u^{oL}|_{x_{3p}=0} \quad (\text{A-58})$$

$$\psi^L|_{x_{2p'}=L_{2p'}} = \psi^L|_{x_{3p}=0} \quad (\text{A-59})$$

$$w^L|_{x_{2p'}=L_{2p'}} = w^L|_{x_{3p}=0} \quad (\text{A-60})$$

$$N_x^L|_{x_{2p'}=L_{2p'}} = N_x^L|_{x_{3p}=0} \quad (\text{A-61})$$

$$M_y^L|_{x_{2p'}=L_{2p'}} = M_y^U|_{x_{3p}=0} \quad (\text{A-62})$$

$$Q_z^L|_{x_{2p'}=L_{2p'}} = Q_z^U|_{x_{3p}=0} \quad (\text{A-63})$$

Region 3 At $x_{3p} = 0$,

$$N_x^U \Big|_{x_{3p}=0} = 0 \quad (\text{A-64})$$

$$M_y^U \Big|_{x_{3p}=0} = 0 \quad (\text{A-65})$$

$$Q_z^U \Big|_{x_{3p}=0} = 0 \quad (\text{A-66})$$

At $x_{3p} = L_{3p}$ ($x_3 = 0$),

$$u^{oU} \Big|_{x_{3p}=L_{3p}} = u^{oU} \Big|_{x_3=0} \quad (\text{A-67})$$

$$\psi^U \Big|_{x_{3p}=L_{3p}} = \psi^U \Big|_{x_3=0} \quad (\text{A-68})$$

$$w^U \Big|_{x_{3p}=L_{3p}} = w^U \Big|_{x_3=0} \quad (\text{A-69})$$

$$N_x^U \Big|_{x_{3p}=L_{3p}} = N_x^U \Big|_{x_3=0} \quad (\text{A-70})$$

$$M_y^U \Big|_{x_{3p}=L_{3p}} = M_y^U \Big|_{x_3=0} \quad (\text{A-71})$$

$$Q_z^U \Big|_{x_{3p}=L_{3p}} = Q_z^U \Big|_{x_3=0} \quad (\text{A-72})$$

$$u^{oL} \Big|_{x_{3p}=L_{3p}} = u^{oL} \Big|_{x_3=0} \quad (\text{A-73})$$

$$\psi^L \Big|_{x_{3p}=L_{3p}} = \psi^L \Big|_{x_3=0} \quad (\text{A-74})$$

$$w^L \Big|_{x_{3p}=L_{3p}} = w^L \Big|_{x_3=0} \quad (\text{A-75})$$

$$N_x^L \Big|_{x_{3p}=L_{3p}} = N_x^L \Big|_{x_3=0} \quad (\text{A-76})$$

$$M_y^L \Big|_{x_{3p}=L_{3p}} = M_y^L \Big|_{x_3=0} \quad (\text{A-77})$$

$$Q_z^L \Big|_{x_{3p}=L_{3p}} = Q_z^L \Big|_{x_3=0} \quad (\text{A-78})$$

At $x_3 = L_3$,

$$N_x^U \Big|_{x_3=L_3} = \frac{P A_{II}^U}{A_{II}^U + A_{II}^L + E\eta} \quad (\text{A-79})$$

$$M_y^U \Big|_{x_3=L_3} = 0 \quad (\text{A-80})$$

$$Q_z^U \Big|_{x_3=L_3} = 0 \quad (\text{A-81})$$

$$N_x^L \Big|_{x_3=L_3} = \frac{P A_{II}^L}{A_{II}^U + A_{II}^L + E\eta} \quad (\text{A-82})$$

$$M_y^L \Big|_{x_3=L_3} = 0 \quad (\text{A-83})$$

$$Q_z^L \Big|_{x_3=L_3} = 0 \quad (\text{A-84})$$